

Seasonal and Interannual Variability in South Asian Monsoon Dynamics

Thesis by
Jennifer Marie Walker

In Partial Fulfillment of the Requirements for the
degree of
Doctor of Philosophy

The logo for the California Institute of Technology (Caltech), featuring the word "Caltech" in a bold, orange, sans-serif font.

CALIFORNIA INSTITUTE OF TECHNOLOGY
Pasadena, California

2017
Defended December 5, 2016

© 2017

Jennifer Marie Walker
ORCID: 0000-0002-1709-0888

All rights reserved

ABSTRACT

Recent theoretical advances indicate that the South Asian summer monsoon (SASM) should be viewed as an energetically-direct cross-equatorial Hadley circulation, with the monsoonal precipitation primarily occurring in its ascending branch, rather than its traditional interpretation as a large land-sea breeze circulation. Despite these developments, very few studies have explored the implications of these emerging theories for the observed variability of the SASM.

This is the goal of this PhD thesis, which uses atmospheric reanalysis data from recent decades to investigate seasonal transitions and interannual variability of the SASM. Our approach differs from previous studies in its focus on the large-scale atmospheric dynamics of the SASM: more specifically, we analyze the tropical circulation throughout the SASM sector and its relationship with extratropical weather systems in both hemispheres that can affect transports of momentum and energy.

The atmospheric moisture budget over the SASM region provides a crucial starting point for our work. We use this budget to introduce a novel objective index for the onset and retreat of the SASM, which robustly captures the expected seasonal transitions in precipitation and winds and eliminates the need for arbitrarily selected thresholds. Using this index, we show how the SASM onset and retreat are associated with a coherent set of seasonal transitions in circulation, jet streams, precipitation, energetics, and momentum balance throughout the SASM sector. These transitions closely resemble those of the zonal mean Hadley circulation, indicating that the SASM projects strongly onto the zonal mean and that the observed SASM is consistent with new theoretical interpretations.

We also use the atmospheric moisture budget to define a new index for the SASM strength on interannual time scales. We show that interannual variability in SASM net precipitation is primarily caused by variations in winds rather than variations in humidity, highlighting the importance of understanding drivers of the large-scale circulation and its changes. We then use linear regression analysis to identify robust changes in the circulation associated with SASM year-to-year variability. We find that strong monsoons are associated with a northward expansion of the overturning circulation and a decreased near-surface land-sea thermal contrast, in disagreement with the traditional view of the SASM as a sea-breeze circulation. We also find teleconnections between SASM strength and temperatures, winds, and

momentum and energy transports in the southern hemisphere extratropics. These interhemispheric teleconnections, which have not been previously identified, suggest new directions for future research to improve our understanding of the mechanisms involved in SASM variability.

Important advances in modeling and predicting the SASM at all timescales require a deeper understanding of the fundamental processes driving this system. Through theoretically-guided analyses of the SASM observed variability, this dissertation work takes an important step in this direction and provides novel insight into long-standing open questions on the SASM, with crucial implications for its predictability.

PUBLISHED CONTENT AND CONTRIBUTIONS

Walker, J. M. and S. Bordoni (2016). “Onset and withdrawal of the large-scale South Asian monsoon: A dynamical definition using change point detection”. In: *Geophys. Res. Lett.* 43. DOI: 10.1002/2016GL071026.

J.M.W. developed the methodology, performed the data analysis, and wrote the manuscript as lead author.

Walker, J. M., S. Bordoni, and T. Schneider (2015). “Interannual Variability in the Large-Scale Dynamics of the South Asian Summer Monsoon”. In: *Journal of Climate* 28.9, pp. 3731–3750. DOI: 10.1175/JCLI-D-14-00612.1.

J.M.W. assisted in developing the methodology, performed the data analysis, and wrote the manuscript as lead author.

Ensberg, J. J., J. A. de Gouw, R. Ellis, J. Flynn, C. L. Haman, P. L. Hayes, J.-L. Jimenez, B. L. Lefer, A. M. Middlebrook, J. G. Murphy, J. A. Neuman, J. S. Craven, J. B. Nowak, J. M. Roberts, J. Stutz, J. W. Taylor, P. R. Veres, J. M. Walker, J. H. Seinfeld, A. R. Metcalf, J. D. Allan, W. M. Angevine, R. Bahreini, J. Brioude, C. Cai, and H. Coe (2012). “Inorganic and black carbon aerosols in the Los Angeles Basin during CalNex”. In: *Journal of Geophysical Research* 118, pp. 1–27. DOI: 10.1029/2012JD018136.

J.M.W. conducted GEOS-Chem modeling to provide boundary conditions for the CMAQ regional model.

Walker, J. M., S. Philip, R. V. Martin, and J. H. Seinfeld (2012). “Simulation of nitrate, sulfate, and ammonium aerosols over the United States”. In: *Atmospheric Chemistry and Physics* 12.22, pp. 11213–11227. DOI: 10.5194/acp-12-11213-2012.

J.M.W. conducted GEOS-Chem model simulations, analyzed model output and surface measurement data, incorporated satellite measurements from S.P. and R.V.M. into the data analysis, and wrote the manuscript as lead author.

TABLE OF CONTENTS

Abstract	iii
Published Content and Contributions	v
Table of Contents	vi
List of Illustrations	vii
List of Tables	xiv
Chapter I: Introduction	1
Chapter II: Definition of Monsoon Onset and Withdrawal	6
2.1 Introduction	6
2.2 Data	7
2.3 SASM onset and withdrawal index	8
2.4 Seasonal transitions	13
2.5 Conclusions	20
2.6 Appendix: Supporting information	21
Chapter III: Seasonal Variability	26
3.1 Introduction	27
3.2 Data and methods	29
3.3 Atmospheric circulation and thermodynamics	31
3.4 Momentum budget	40
3.5 Discussion and conclusions	46
Chapter IV: Interannual Variability	48
4.1 Introduction	48
4.2 Data and methods	51
4.3 Atmospheric moisture budget	53
4.4 Large-scale patterns of monsoon variability	57
4.5 Teleconnections with southern hemisphere extratropics	67
4.6 Correlations with modes of SST variability	71
4.7 Summary and concluding remarks	72
4.8 Appendix: Long-term trends	73
Bibliography	80
Appendix A: Simulation of nitrate, sulfate, and ammonium aerosols over the United States	92

LIST OF ILLUSTRATIONS

<i>Number</i>	<i>Page</i>
2.1 June–September (JJAS) fraction of yearly rainfall in GPCP climatology. The magenta rectangle shows the averaging region for the CHP index. Kerala state is outlined in blue.	8
2.2 (a) Example timeseries of MERRA-2 daily atmospheric moisture budget averaged over 10-30°N, 60-100°E in the year 2000 (Jan 1, 2000 - Feb 3, 2001), showing the total precipitation (dashed black), evaporation (solid black), MFC (heavy solid black), atmospheric storage (solid gray), and CMFC (red). Vertical black lines indicate the onset and withdrawal days in this year. (b) Yearly onset dates defined by CHP (heavy black), HOWI (green), OCI (red), and MOK (blue). (c-d) Climatological composites of MERRA-2 (1980-2015) and GPCP (1997-2015) daily fields centered on onset date, averaged 60-100°E, with vertical black lines indicating mean onset and withdrawal days, and dashed vertical black line indicating the start of the “Mature” stage (day 15). (c) Moisture budget averaged 10-30°N, showing MFC (solid black, mm day ⁻¹), GPCP (dashed black, mm day ⁻¹), and CMFC (red, mm). (d) 850 hPa zonal (black) and meridional (red) winds at 15°N (m s ⁻¹).	10
2.3 (a) Box-and-whisker plot for yearly onset dates, withdrawal dates, and season lengths defined by CHP. The blue boxes indicate the range between the 25th and 75th percentiles, with a red line for the median and whiskers indicating the total range. (b-c) Climatological composites of MERRA-2 and GPCP daily fields centered on withdrawal date, averaged 60-100°E, with vertical black lines indicating mean onset and withdrawal days. (b) Moisture budget averaged 10-30°N, showing MFC (solid black, mm day ⁻¹), GPCP (dashed black, mm day ⁻¹), and CMFC (red, mm). (c) 850 hPa zonal (black) and meridional (red) winds at 15°N (m s ⁻¹).	11

2.4	Seasonal evolution of (a) GPCP and (b-d) MERRA-2 climatological composites centered on onset date, averaged 60-100°E: (a) precipitation (mm day^{-1}), (b) 200 hPa meridional wind (m s^{-1}), (c) 200 hPa zonal wind (m s^{-1}), and (d) 850 hPa zonal wind (m s^{-1}). Vertical black lines indicate mean onset and withdrawal days, and dashed vertical black line indicates the start of the “Mature” stage (day 15). Latitudes with less than 50% of grid points above the topography are masked out in (d).	13
2.5	As in Fig. 2.4, but for composites centered on withdrawal date. . . .	14
2.6	Maps of zonal wind (m s^{-1}) at 850 hPa in MERRA-2 climatological composites centered on onset date, for days -15 through 40.	15
2.7	As in Fig. 2.6 but for meridional wind.	16
2.8	Maps of daily precipitation rates (mm day^{-1}) in GPCP climatological composites centered on onset date, for days 0 through 55. The magenta rectangle shows the averaging region for the CHP index. . .	18
2.9	As in Fig. 2.8, but for composites centered on withdrawal date, for days -45 through 10.	19
2.10	Local onset dates defined with CHP method using GPCP precipitation. (a) Climatological mean (contours) and standard deviation (colors) of onset dates. (b) Regression coefficients (day day^{-1}) of local onset dates onto large-scale CHP onset index, with gray stippling indicating the regions where the correlation is significant at the 5% level. Kerala state is outlined in blue.	19
2.11	As in Fig. 2.10, but for withdrawal dates.	20
2.12	Scatter plots and linear regressions of detrended monsoon season totals (mm), from onset to retreat in each year, of MERRA-2 moisture flux convergence (MFC_TOT), MERRA-2 precipitation (PCP_TOT), GPCP precipitation (GPCP_TOT), and MERRA-2 evaporation (EVAP_TOT), averaged 10–30°N, 60–100°E vs. detrended SASM onset, retreat, and season length (days). Note that the GPCP dataset is shorter than MERRA-2, so higher correlation coefficients are required for statistical significance at the 5% level.	23

- 2.13 Scatter plots and linear regressions of detrended seasonal mean rates (mm day^{-1}), averaged from onset to retreat in each year, of MERRA-2 moisture flux convergence (MFC_AVG), MERRA-2 precipitation (PCP_AVG), GPCP precipitation (GPCP_AVG), and MERRA-2 evaporation (EVAP_AVG), averaged $10\text{--}30^\circ\text{N}$, $60\text{--}100^\circ\text{E}$ vs. detrended SASM onset, retreat, and season length. Note that the GPCP dataset is shorter than MERRA-2, so higher correlation coefficients are required for statistical significance at the 5% level. 24
- 3.1 June–September (JJAS) fraction of yearly rainfall in GPCP climatology (contours) and ocean mixed layer depths (m) in Ifremer May climatology (colors). The blue rectangle shows the averaging region for the SASM onset index. 30
- 3.2 Climatological composites of MERRA-2 (1980-2015) and GPCP (1997-2015) daily fields centered on onset date, averaged $60\text{--}100^\circ\text{E}$, with vertical black lines indicating mean onset and withdrawal days, and dashed vertical black line indicating the start of the “Mature” stage (day 15). (a) Moisture budget averaged $10\text{--}30^\circ\text{N}$, showing MFC (solid black, mm day^{-1}), GPCP (dashed black, mm day^{-1}), and CMFC (red, mm). (b) 200 hPa zonal wind (black, m s^{-1}) and 500 hPa streamfunction (red, 10^9 kg s^{-1}) at 0°N . (c) 200 hPa atmospheric temperature at 30°N (black, K) and 30°S (red, K). Panel (a) is adapted from Walker and Bordoni (2016). 32
- 3.3 Latitude-pressure contours of SASM sector mean streamfunction (black, contour interval $5 \times 10^9 \text{ kg s}^{-1}$) and zonal wind (violet, contour interval 5 m s^{-1}), on days -45, -30, -15, 0, 15, and 30. Positive contours are solid and negative contours are dashed. The zero line is indicated by a heavy solid contour for the zonal wind, and is omitted for the streamfunction. Sector mean topography is shaded in black. 33

3.4	Seasonal evolution of (a) GPCP and (b-e) MERRA-2 climatological composites centered on onset date, averaged 60–100°E: (a) precipitation (mm day^{-1}), (b) 500 hPa streamfunction (10^9 kg s^{-1}), (c) 200 hPa zonal wind (m s^{-1}), (d) 200 hPa temperature (K), and (e) near-surface equivalent potential temperature (K). Vertical black lines indicate mean onset and withdrawal days, and dashed vertical black line indicates the start of the “Mature” stage (day 15). Panels (a, c) are adapted from Walker and Bordoni (2016).	34
3.5	Maps of precipitation (a–c, mm day^{-1}), 200 hPa zonal wind (d–f, m s^{-1}), and 200 hPa temperature (g–i, K) on day 0 (a, d, g) and the anomaly from day 0 to day 15 (b, e, h). SASM sector mean fields vs. latitude on days 0, 15, and the anomaly from day 0 to 15 are shown in (c, f, i).	36
3.6	As in Fig. 3.5, but for near-surface equivalent potential temperature (a–c, K) and near-surface temperature (d–f, K).	37
3.7	Meridional fluxes of MSE components, averaged 5°S–5°N (10^9 W m^{-1}). (a) Total MSE flux $v(C_p T + gz + L_v q_v)$. (b) Enthalpy flux $vC_p T$. (c) Geopotential flux vgz . (d) Latent energy flux $vL_v q_v$	39
3.8	Cross-equatorial fluxes of MSE (PW) averaged 5°S–5°N and integrated across the Somali jet sector (40–60°E, red) and SASM sector (60–100°E, blue), showing fluxes of total MSE (heavy solid), enthalpy (dashed), geopotential energy (dotted), and latent energy (solid).	40
3.9	Dominant terms in the SASM sector mean zonal momentum balance (10^{-4} m s^{-2}) and zonal wind (m s^{-1}) at 200 hPa. The components of the momentum balance are: advection by MMC (solid blue), Coriolis MMC (dashed blue), pressure gradient force (black), eddy-mean flow cross term (green), and EMFC from transient and stationary eddies (violet). The sum of the MMC advection and Coriolis terms is shown as DMDY (red): $f[\bar{v}] - \frac{1}{\cos\theta}[\bar{v}]\partial_y([\bar{u}]\cos\theta) = \frac{-1}{\text{acos}\theta}[\bar{v}]\partial_y[\bar{m}]$	42
3.10	Latitude-pressure contours of SASM sector mean streamfunction (black, contour interval $5 \times 10^9 \text{ kg s}^{-1}$) and the zero line of zonal wind (violet) on days -30, 0, and 30, showing the total, mean, and eddy components of the streamfunction.	45

4.1	Interannual variability of the SASM strength, based on the ERA-Interim atmospheric moisture budget, showing the dynamic component, thermodynamic component, and total variability (mm day^{-1}).	55
4.2	Timeseries of the MFC index, based on ERA-Interim atmospheric moisture budget, along with precipitation from ERA-Interim and GPCP averaged over the same region ($60\text{-}100^{\circ}\text{E}$, $10\text{-}30^{\circ}\text{N}$), and the AIR index. Each timeseries is based on JJAS averages, and is shown as the standardized anomaly from the climatological mean.	57
4.3	JJAS precipitation (mm day^{-1}) from GPCP, showing (a) 1979-2011 climatology, and (b) regression coefficients from linear regression of JJAS precipitation for each year against the standardized MFC index. Gray stippling shows regions where the regression coefficient is significant at the 5% level. The green rectangle shows the averaging region for the monsoon strength index.	58
4.4	Climatology (a-c) and regression coefficients onto MFC index (d-f) of JJAS ERA-Interim SASM sector mean streamfunction, vertical pressure velocity, and meridional velocity. Black contours are positive while violet contours are negative; zero contours are omitted. Gray shading in d-f shows regions where the regression coefficient is significant at the 5% level. Black shading shows the sector mean topography. Contour intervals are: (a) $5 \times 10^9 \text{ kg s}^{-1}$, (b) 0.02 Pa s^{-1} , (c) 2 m s^{-1} , (d) $0.5 \times 10^9 \text{ kg s}^{-1}$, (e) 0.002 Pa s^{-1} , (f) 0.1 m s^{-1} .	59
4.5	Streamfunctions representing "Strong" (blue) and "Weak" (red) monsoonal circulations, defined as those associated with a ± 2 standard deviation excursion of the MFC index. Positive contours are solid, negative contours are dashed, and zero contours are omitted. Contour interval is $5 \times 10^9 \text{ kg s}^{-1}$.	60
4.6	SASM sector GPCP JJAS precipitation profiles (mm day^{-1}) for "Strong" (blue) and "Weak" (red) monsoons.	61
4.7	Climatology (a-b) and regression coefficient onto MFC index (c-d) of JJAS ERA-Interim zonal wind (m s^{-1}) at 200 hPa and 850 hPa. Gray stippling shows the regions where the regression coefficient is significant at the 5% level. The green rectangle shows the averaging region for the MFC index.	62

4.8	Climatology (a) and regression coefficient onto MFC index (b) of JJAS ERA-Interim SASM sector EMFD (colors, m s^{-2}) and zonal wind (contours, m s^{-1}). Positive contours are in black, negative contours in violet, and zero contours in heavy black. Gray stippling shows the regions where the EMFD regression coefficient is significant at the 5% level. Black shading shows the sector mean topography. Contour levels of zonal wind are: (a) 5 m s^{-1} and (b) 0.25 m s^{-1}	63
4.9	Climatology (a-b) and regression coefficient onto MFC index (c-d) of JJAS ERA-Interim atmospheric temperature (K) at 200 hPa and 850 hPa. Gray stippling shows the regions where the regression coefficient is significant at the 5% level. The green rectangle shows the averaging region for the MFC index.	64
4.10	SASM sector lower-tropospheric temperature (K) in MAM (dashed) and JJAS (solid) for "Strong" (blue) and "Weak" (red) monsoons, using ERA-Interim temperatures at 850 hPa.	65
4.11	Climatology (a) and regression coefficient onto monsoon index (b) of JJAS ERA-Interim vertically integrated MSE transient eddy fluxes (kW M^{-1}). Gray stippling shows the regions where the regression coefficient is significant at the 5% level. The green rectangle shows the averaging region for the MFC index.	68
4.12	Southern hemisphere JJAS ERA-Interim SASM sector EMFD (colors, m s^{-2}) and zonal wind (contours, m s^{-1}) representing (a) "Strong" and (b) "Weak" SASM years. Zonal wind contours are 5 m s^{-1} , with positive contours in black, negative contours in violet, and zero contours in heavy black. Black shading shows the sector mean topography.	70
4.13	Linear trend ($\text{mm day}^{-1} \text{ year}^{-1}$) in reanalysis precipitation over the period 1979-2011 (ERA40: 1979-2002). Gray stippling shows the regions where the trend is significant at the 5% level.	76
4.14	Same as in Fig. 4.13, but for various other precipitation datasets. Trends computed over 1979-2011 (TRMM: 1998-2011).	77
4.15	Anomalies in SASM JJAS precipitation (mm day^{-1}) in reanalysis and precipitation data over the period 1979-2011 (ERA40: 1979-2002, TRMM: 1998-2011). All values are based on area averages over the region $60\text{-}100^\circ\text{E}$, $10\text{-}30^\circ\text{N}$, except AIR which is an average over India.	78

4.16 Same as in Fig. 4.15, but with 5-year running mean. 79

LIST OF TABLES

<i>Number</i>	<i>Page</i>
2.1 Summary of CHP indices of large-scale SASM onset, withdrawal, and season length.	9
2.2 Interannual correlation coefficients between CHP indices, GPCP seasonal total and mean rainfall (from onset to withdrawal each year, averaged 10–30°N, 60–100°E), and ENSO indices. Values significant at the 5% level are indicated in bold. Note that the GPCP dataset is shorter than the other indices, so higher correlation coefficients are required for statistical significance at the 5% level.	25
4.1 Linear trends in SASM JJAS yearly and 5-year running mean precipitation ($\text{mm day}^{-1} (33 \text{ years})^{-1}$) over the period 1979-2011 (ERA40: 1979-2002, TRMM:1998-2011). All values are based on area averages over the region 60-100°E, 10-30°N, except AIR which is an average over India. The trend in 5-year running mean is omitted from TRMM due to insufficient number of years in the data. Trends which are statistically significant at the 5% level are in bold.	75

Chapter 1

INTRODUCTION

Monsoons are tropical circulations with a seasonal cycle characterized by dry winters and wet summers and seasonally reversing wind patterns. The South Asian summer monsoon (SASM) is the largest monsoon system on Earth, bringing heavy summer rainfall to densely populated and rapidly growing countries in South Asia. The SASM rainy season begins with sudden and dramatic changes in atmospheric circulation and precipitation: near-surface winds over the Arabian Sea abruptly switch from northeasterly to southwesterly; intense cross-equatorial flow develops in a low-level jet stream off the eastern coast of Africa; and the first bursts of monsoon rainfall occur over Southeast Asia, the southern tip of India, the Arabian Sea, and the Bay of Bengal. Over the following weeks, monsoonal rainbelts propagate northward into the Indian subcontinent and mature monsoon conditions are established, persisting throughout most of the June-September (JJAS) boreal summer. The seasonal mean SASM is characterized by a deep meridional overturning cell, with a subtropical rainfall peak in its ascending branch; a reversed meridional gradient in upper-tropospheric temperatures, with temperatures increasing poleward from the equator to the northern hemisphere subtropics; and a strong upper-level easterly jet across a broad band of tropical latitudes. The SASM tapers off in early autumn, with a slow southward retreat of monsoon rains and a gradual transition of the circulation back to equinox conditions.

The SASM displays variability on timescales from intraseasonal through interannual and decadal (e.g., Webster et al., 1998; Gadgil, 2003; Turner and Annamalai, 2012). On seasonal timescales, accurate forecasting of monsoon onset is critical for effective agriculture planning and water management in the SASM region (e.g., Raju et al., 2007; Adamson and Nash, 2012). Interannual variability in the SASM strength, as measured by the standard deviation in summer rainfall over India, is approximately 10% of the mean summer rainfall (Gadgil, 2003). This year-to-year variability of the SASM is sufficient to trigger drought and flood conditions, with major agricultural, economic, and social impacts (e.g., Webster et al., 1998; Gadgil and Kumar, 2006).

Despite its crucial economic and societal impacts, fundamental mechanisms controlling the SASM are not well understood and predictive skills remain limited.

Traditionally, the SASM is viewed as a planetary scale sea-breeze circulation, driven by surface temperature contrasts and associated atmospheric pressure gradients between the Asian continent and the Indian ocean to the south (e.g., Webster and Fasullo, 2003). Surface temperature gradients alone can generate only a shallow circulation (Schneider and Lindzen, 1977), whereas the SASM circulation extends through the depth of the troposphere; thus the sea-breeze paradigm has been modified to include the effects of elevated diabatic heating from moist convection (e.g., Webster et al., 1998) and the Tibetan plateau (e.g., Li and Yanai, 1996). In these studies, the monsoonal circulation is understood as a linear response to diabatic heating (e.g., Gill, 1980; Hoskins and Rodwell, 1995) and surface inhomogeneities between land and ocean are assumed to be an essential mechanism driving the SASM circulation, with the meridional temperature gradient viewed as an external forcing.

In recent years, an alternative theoretical framework has emerged in the literature, which views the SASM as a regional manifestation of the tropical Hadley circulation in boreal summer, with monsoonal rains associated with the seasonal migration of the intertropical convergence zone (ITCZ) onto the subtropical continent (e.g., Gadgil, 2003). In this framework, the SASM is understood as a thermally-direct overturning circulation, which approaches conservation of angular momentum, and is thus highly nonlinear (e.g., Privé and Plumb, 2007; Bordoni and Schneider, 2008; Schneider and Bordoni, 2008). In support of this view, modeling studies have shown that monsoonal circulations can exist even on aquaplanets without any land-ocean thermal contrasts (Privé and Plumb, 2007; Bordoni and Schneider, 2008), thus suggesting that surface inhomogeneities are not an essential driving mechanism for the monsoon, although they may alter the properties of the monsoonal circulation. In this emerging view, the reversed meridional temperature gradient (e.g. Li and Yanai, 1996) and convective heating (e.g., Gill, 1980) are not considered as external forcings, but rather are in themselves viewed as part of the atmosphere's response to the seasonal variation of insolation.

This progressive shift in the theoretical interpretation of the monsoon suggests the need to revisit the large-scale dynamics of the SASM from an observational perspective. Mechanisms which are important in the zonal mean Hadley circulation, such as interactions with extratropical eddy fluxes of momentum (e.g., Schneider and Bordoni, 2008) and energy (e.g. Kang et al., 2008), may be relevant to the SASM. And conversely, the role of the SASM in the tropical circulation needs to be

elucidated; as I will show, the SASM sector mean circulation projects strongly onto the zonal mean and dominates the abrupt seasonal transition from boreal spring to summer.

In this thesis, I will use atmospheric reanalysis data from recent decades to investigate seasonal and interannual variability in SASM dynamics. Although there is considerable regional variability within the SASM domain, this thesis addresses the variations of the monsoon as a large-scale circulation, focusing on large-scale atmospheric moisture, energy, and momentum budgets rather than local or regional features. As explained further in Chapter II, I define the SASM sector as 60–100°E to encompass the longitudes where the circulation behaves coherently as an overturning circulation with the majority of mass transport within the meridional-vertical plane, and to include the precipitation maxima over India and the Bay of Bengal. I define the SASM domain, where the majority of SASM rainfall occurs, as 10–30°N, 60–100°E (Fig. 2.1), corresponding with the SASM sector in longitude, and with latitude limits selected to focus on the subtropical monsoonal precipitation, excluding the topography to the north and the oceanic regions to the south whose seasonal variability is not consistent with the summer monsoon.

There are three overarching goals in this thesis:

1. **Develop methodology:** What measures can be used to characterize the seasonal transitions and interannual variability of the large-scale SASM, accurately representing both circulation and precipitation?
2. **Compare observed SASM with theoretical frameworks:** Which proposed mechanisms are most consistent with observed variability in the SASM?
3. **Identify patterns of tropical and extratropical variability associated with the SASM:** How does the circulation throughout the SASM sector vary seasonally as the monsoon progresses, and interannually with monsoon strength? Do any teleconnections exist between the SASM and the southern hemisphere, and if so, what new mechanisms of SASM variability do these suggest? How does the SASM sector project onto the zonal mean circulation?

The first goal is necessary because I want to accurately assess the variability in both the circulation and rainfall of the SASM: many large-scale dynamic indices of the SASM have been defined previously, but these indices do not correlate well with

the actual monsoon rainfall over South Asia (e.g., Webster and Yang, 1992; Ailikon and Yasunari, 1998; Goswami et al., 1999; Wang and Fan, 1999). To solve this problem, I develop robust new indices of SASM onset, withdrawal, and strength, which use the atmospheric moisture budget to link monsoon precipitation directly to the large-scale circulation.

In Chapter II, I revisit one of the major outstanding problems in the monsoon literature: defining the onset and withdrawal of the SASM. I use change point detection of the atmospheric moisture flux converging in the SASM domain to introduce a robust index that captures the seasonal transitions in monsoon circulation and precipitation, and provides a precise characterization of the timescales and stages of the SASM. I also show that this methodology can be used at grid points within the SASM domain to compute local onset and withdrawal dates which are well correlated with the large-scale index on interannual timescales, providing insight into the relationships between local and large-scale monsoon timing.

In Chapter III, I use the index developed in Chapter II to construct climatological composites, exploring the seasonal variability of the SASM, and comparing the observed monsoon with theoretical frameworks and idealized monsoon studies. I analyze important aspects of the energetics and momentum balance of the circulation throughout the SASM sector, including atmospheric fields remote to the monsoon, which affect the large-scale transports of momentum and energy. Examining the abrupt transitions at monsoon onset, I explore the role of eddy-mean flow feedbacks as an onset mechanism, as well as the contribution of the SASM sector to seasonal transitions of the zonal mean circulation.

In Chapter IV, I investigate the interannual variability of the SASM. First, I develop a robust new index for seasonal mean SASM strength, using the atmospheric moisture budget to link monsoon precipitation directly to the large-scale circulation. This formulation allows the water vapor budget to be decomposed into dynamic and thermodynamic components, elucidating the role of the large-scale circulation in monsoon rainfall variability. Using linear regression analyses, I examine changes in dynamics and thermodynamics associated with interannual variations in monsoon strength. I also explore teleconnections with the southern hemisphere extratropics and identify possible mechanisms of SASM variability that have been discussed in the zonal mean tropical circulation but have not been previously identified as a contributing factor in SASM variability.

Altogether, these theoretically-guided analyses of the SASM contribute important

insights into the fundamental mechanisms of the SASM and its variability on seasonal and interannual timescales. In addition, the methodologies developed here provide a robust framework that can be used to assess variability and trends in the SASM in both observations and climate simulations, to further enhance our understanding of the SASM in current and future climates.

Chapter 2

DEFINITION OF MONSOON ONSET AND WITHDRAWAL

Walker, J. M. and S. Bordoni (2016). “Onset and withdrawal of the large-scale South Asian monsoon: A dynamical definition using change point detection”. In: *Geophys. Res. Lett.* 43. DOI: 10.1002/2016GL071026.

Abstract

We introduce an objective definition for onset and withdrawal of the South Asian summer monsoon (SASM), based on the large-scale atmospheric moisture budget. The change point (CHP) index allows precise characterization of the different stages and timescales of the large-scale SASM and is highly correlated with the local operational index, the monsoon onset over Kerala. The CHP-based onset and withdrawal dates, which capture the expected seasonal transitions in rainfall and winds, correspond with regime changes in the SASM moisture budget between negative and positive net precipitation. Climatological composites reveal that the seasonal transitions in SASM sector mean precipitation and circulation closely resemble those of the zonal mean Hadley circulation. The CHP index at grid points within the SASM domain yields a robust definition of local onset and withdrawal dates, which are well correlated with the large-scale index on interannual timescales, providing insight into the regional variability of the SASM.

2.1 Introduction

The onset of the South Asian Summer Monsoon (SASM) is marked by a sharp increase in rainfall and abrupt reversal of winds over South Asia. Accurately defining and forecasting this transition is critical for effective agriculture planning and water management in the region (e.g., Raju et al., 2007; Adamson and Nash, 2012). Many different measures of SASM onset exist, but there is no widely accepted objective definition. The India Meteorological Department (IMD) employs the monsoon onset over Kerala (MOK) as an operational index, using a subjective method based on rain gauge data, winds, and outgoing longwave radiation (Rao, 1976; Ananthakrishnan and Soman, 1988). Objective definitions of SASM onset include measures such as the increase of rainfall above a threshold (Wang and LinHo, 2002), transitions in vertically integrated moisture transport (Fasullo and Webster, 2003), reversal

of surface wind (Ramage, 1971), and intensification of the lower-level Somali jet (Taniguchi and Koike, 2006; Wang et al., 2009).

Having been developed for specific applications, such as operational forecasts and evaluation of observed variability, existing definitions are generally not well suited for broader use. The MOK cannot be extended to identify SASM onset in climate model simulations, due to its subjective methodology. Objective indices are mostly threshold based and sensitivity to the selected threshold can yield onset dates that vary significantly with slightly different thresholds; this issue is especially critical when comparing datasets or climate models, which may have different biases in their mean climatologies. Threshold-based indices are also susceptible to false onsets due to pre-monsoon rainfall peaks and wind anomalies caused by transient weather systems (e.g., Fieux and Stommel, 1977; Flatau et al., 2001; Noska and Misra, 2016).

In this study, we introduce an objective definition of large-scale SASM onset and withdrawal which does not require selection of any threshold. This index is based on change point detection of the atmospheric moisture flux converging in the large-scale SASM sector (see Section 3) and robustly represents the seasonal transitions in SASM circulation and precipitation.

2.2 Data

Atmospheric fields for the years 1980-2015 are used from NASA's Modern-Era Retrospective analysis for Research and Applications, Version 2 (MERRA-2; Rienecker et al., 2011; Bosilovich et al., 2015). We use pressure-level winds and vertically integrated moisture fluxes, at a horizontal grid resolution of 0.5° (latitude) \times 0.625° (longitude). Daily means are computed from the 3-hourly reanalysis. For precipitation, we use daily estimates at $1^\circ \times 1^\circ$ grid resolution from the Global Precipitation Climatology Project Version 1.2 One-Degree Daily (GPCP; Huffman et al., 2001; Huffman et al., 2016) from 1997 (first complete year available) through October 2015 (final month available).

Statistical significance of correlation coefficients are computed with a Student's t test, and correlations which are statistically significant at the 5% level are highlighted.

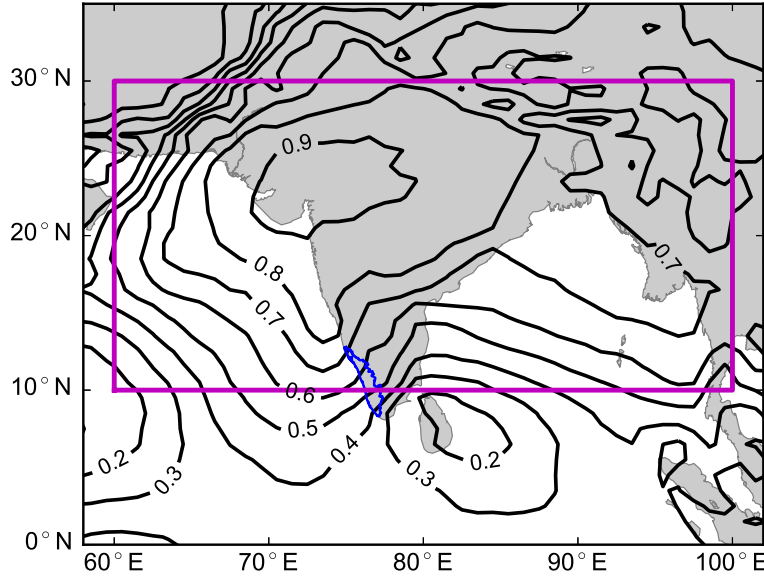


Figure 2.1: June–September (JJAS) fraction of yearly rainfall in GPCP climatology. The magenta rectangle shows the averaging region for the CHP index. Kerala state is outlined in blue.

2.3 SASM onset and withdrawal index

Index definition

Following the approach of our previous work on the interannual variability of the SASM (Walker et al., 2015), we define the SASM region as 10–30°N, 60–100°E (Fig. 2.1, further details in the Supporting Information) and we analyze seasonal transitions in its large-scale atmospheric moisture budget, given by:

$$\text{MFC} = - \int_0^{p_s} \nabla_p \cdot (\mathbf{u} q) \frac{dp}{g} = P - E + \frac{\partial w}{\partial t} \quad (2.1)$$

where MFC is the horizontal moisture flux convergence integrated from the surface to the top of the atmosphere, $\nabla_p \cdot ()$ the horizontal divergence in pressure coordinates, $\mathbf{u} = (u, v)$ the horizontal wind vector, q the specific humidity, P the precipitation rate, E the evaporation rate, and $w = \int_0^{p_s} q \frac{dp}{g}$ the total precipitable water. With negligible storage $\partial w / \partial t$ (e.g., Fig. 2.2(a)), the dominant balance in the SASM region is between MFC and net precipitation ($P - E$). Thus, positive (negative) values of MFC correspond to positive (negative) net precipitation.

We define a change point (CHP) index for SASM onset and withdrawal, adapted from the method of Cook and Buckley (2009) as follows: In each year, we compute the MERRA-2 daily mean MFC, averaged over the SASM region. We then construct

Table 2.1: Summary of CHP indices of large-scale SASM onset, withdrawal, and season length.

	Mean	Standard Deviation	Maximum	Minimum
Onset Date	138 (May-18)	8	153 (Jun-2)	122 (May-2)
Withdrawal Date	292 (Oct-19)	9	311 (Nov-7)	273 (Sep-30)
Season Length	154	13	186	130

a cumulative timeseries of MFC accumulated since January 1 of each year (CMFC). We use a two-phase linear regression of CMFC versus day of year to detect change points over two ranges: days 1-250 for monsoon onset, and days 200-400 for monsoon withdrawal, where the days above 365 (366 in leap years) are from the beginning of the following year.

Fig. 2.2(a) shows an example of the moisture budget terms from Eq. 2.1, the CMFC timeseries, and CHP onset and withdrawal, for the year 2000. The onset captures the first burst of monsoonal rainfall, followed by active-break rainfall cycles throughout the season. The CHP onset (withdrawal) day corresponds approximately to the minimum (maximum) of the CMFC timeseries and to the transition from negative to positive values (positive to negative) of daily MFC, a consistent feature in all years. Thus, our definition of onset corresponds with a moisture budget transition from negative to positive net precipitation (and vice versa for withdrawal).

Fig. 2.2(b) shows the CHP onset dates in each year, while Table 2.1 and Fig. 2.3(a) provide summary statistics of the onset, withdrawal, and season lengths, defined as the number of days from onset to withdrawal. The climatological mean onset is day 138 (May 18), withdrawal is day 292 (October 19), and season length is 154 days, with standard deviations of 8, 9, and 13 days, respectively. In the Supporting Information, we discuss interannual variability in SASM timing associated with El Niño–Southern Oscillation (ENSO). We also show that earlier onsets are associated with longer seasons, and hence enhanced seasonal rainfall (Fig. 2.12, Table 2.2).

Index performance and comparison with other definitions

To assess representativeness of the CHP index and investigate transitions in circulation and precipitation at SASM onset and withdrawal, we compute climatological composites of daily fields centered on the onset (withdrawal) date in each year, so that day 0 corresponds to onset (withdrawal) day. These composites are smoothed with a centered 5-day moving average. Fig. 2.2(c-d) shows composites, centered

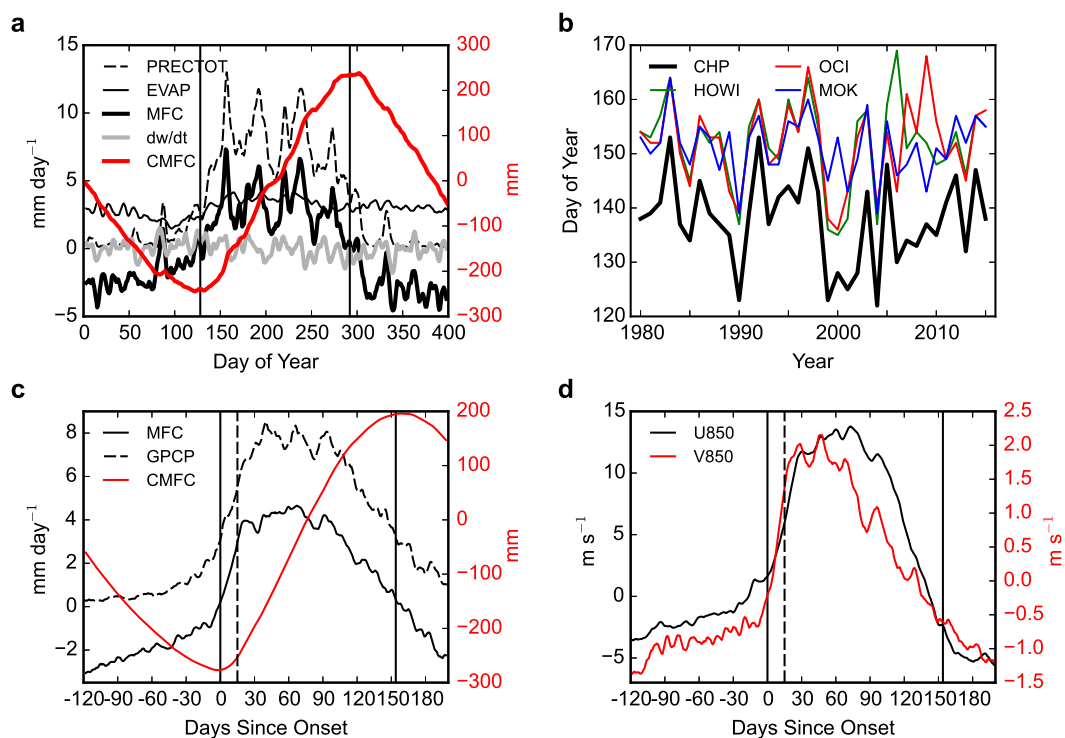


Figure 2.2: (a) Example timeseries of MERRA-2 daily atmospheric moisture budget averaged over 10-30°N, 60-100°E in the year 2000 (Jan 1, 2000 - Feb 3, 2001), showing the total precipitation (dashed black), evaporation (solid black), MFC (heavy solid black), atmospheric storage (solid gray), and CMFC (red). Vertical black lines indicate the onset and withdrawal days in this year. (b) Yearly onset dates defined by CHP (heavy black), HOWI (green), OCI (red), and MOK (blue). (c-d) Climatological composites of MERRA-2 (1980-2015) and GPCP (1997-2015) daily fields centered on onset date, averaged 60-100°E, with vertical black lines indicating mean onset and withdrawal days, and dashed vertical black line indicating the start of the "Mature" stage (day 15). (c) Moisture budget averaged 10-30°N, showing MFC (solid black, mm day⁻¹), GPCP (dashed black, mm day⁻¹), and CMFC (red, mm). (d) 850 hPa zonal (black) and meridional (red) winds at 15°N (m s⁻¹).

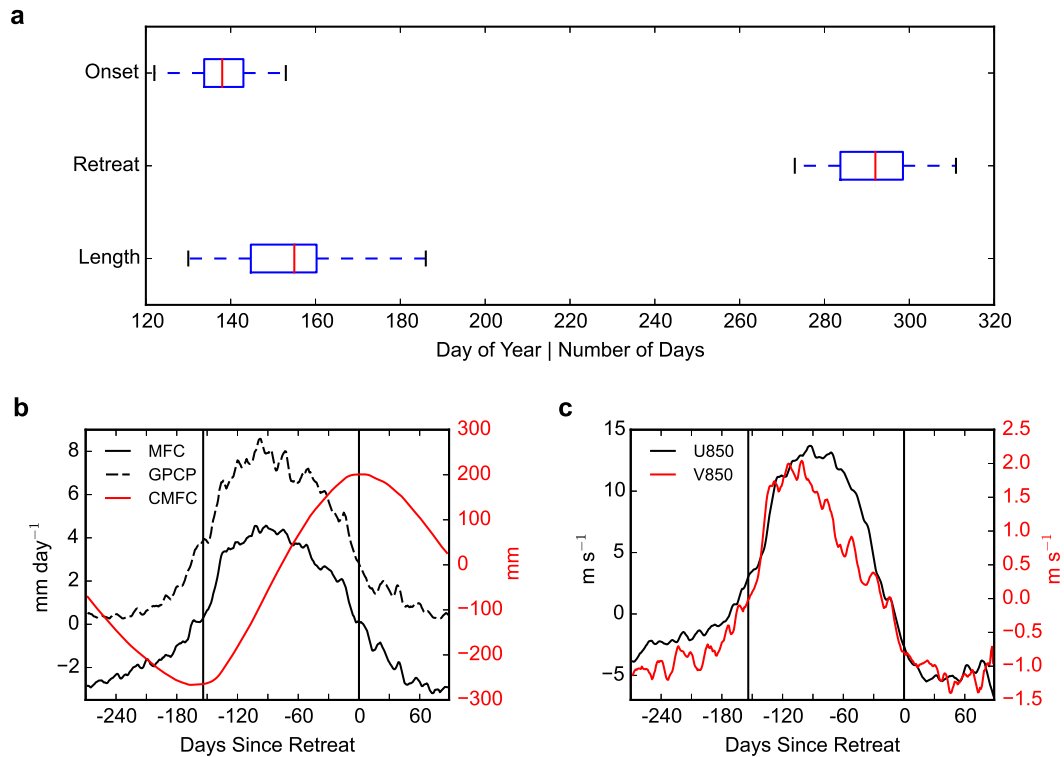


Figure 2.3: (a) Box-and-whisker plot for yearly onset dates, withdrawal dates, and season lengths defined by CHP. The blue boxes indicate the range between the 25th and 75th percentiles, with a red line for the median and whiskers indicating the total range. (b-c) Climatological composites of MERRA-2 and GPCP daily fields centered on withdrawal date, averaged 60-100°E, with vertical black lines indicating mean onset and withdrawal days. (b) Moisture budget averaged 10-30°N, showing MFC (solid black, mm day⁻¹), GPCP (dashed black, mm day⁻¹), and CMFC (red, mm). (c) 850 hPa zonal (black) and meridional (red) winds at 15°N (m s⁻¹).

on onset date, of various precipitation and circulation indices averaged in longitude over the SASM sector (60-100°E). In Fig. 2.2(c), we see that the onset day marks the beginning of a sharp increase in rainfall over the SASM region. Note that the GPCP precipitation timeseries shown here is independent of the MERRA-2 moisture budget and CHP calculations. Fig. 2.2(d) shows 850 hPa zonal (U850) and meridional (V850) winds at 15°N, representing the lower-level flow across the Arabian Sea, Indian peninsula, and Bay of Bengal. Around day 0, there is an abrupt transition in both U850 and V850 from weak negative to strong positive values, indicating wind reversal and development of strong southwesterly flow.

Thus, the CHP index robustly characterizes the distinguishing features of SASM onset: initiation of heavy monsoon rain and reversal of lower-level winds. The

climatological composites centered on withdrawal date (Fig. 2.3) show opposite but much more gradual transitions at withdrawal, in agreement with previous studies (Webster and Yang, 1992; Fasullo and Webster, 2003; Cook and Buckley, 2009).

For comparison with previously defined indices, we consider the MOK dates provided by the IMD and we use MERRA-2 to calculate two previously introduced dynamically-based indices for the large-scale SASM: the hydrologic onset and withdrawal index (HOWI; Fasullo and Webster, 2003), based on transitions in vertically integrated moisture fluxes averaged over the Arabian Sea; and the onset circulation index (OCI; Wang et al., 2009), based on a threshold in 850 hPa zonal wind averaged over the Southern Arabian Sea. Fig. 2.2(b) shows the yearly onset dates defined by these indices. High correlations and lead-lag relationships between them are evident. For MOK, HOWI, and OCI, the climatological mean onset ranges from days 151 to 152 (May 31 to June 1), whereas the climatological mean CHP onset is 13-14 days earlier, on day 138 (May 18). This offset is due to CHP onset representing the beginning of the transition (i.e., the change point) rather than the first day when the monsoon rain and winds are well established, as represented by the other definitions. Interannual variability of CHP onset is highly correlated with the other indices, with correlation coefficients of 0.82, 0.73, and 0.76 with MOK, HOWI, and OCI, respectively. CHP is also more highly correlated with the operational MOK onset than the other two dynamically based indices, with correlation coefficients of 0.82, 0.62 and 0.56 of MOK with CHP, HOWI, and OCI, respectively.

There are numerous advantages to the CHP index in defining seasonal monsoon transitions. Since no thresholds are used, this method is not hindered by the pitfalls of threshold-based indices discussed in Section 1. By construction, the CHP index is not susceptible to false onsets or withdrawals because change points are detected taking into account the MFC at all days in the given range, rather than considering only the values on a single day or few days. Finally, since change points represent the beginning of the onset or withdrawal transition, rather than a day somewhere in the midst of the transition, this definition allows us to characterize more precisely the duration of the transition and to construct composites elucidating the different timescales of the various stages of the monsoon, as discussed in the next section.

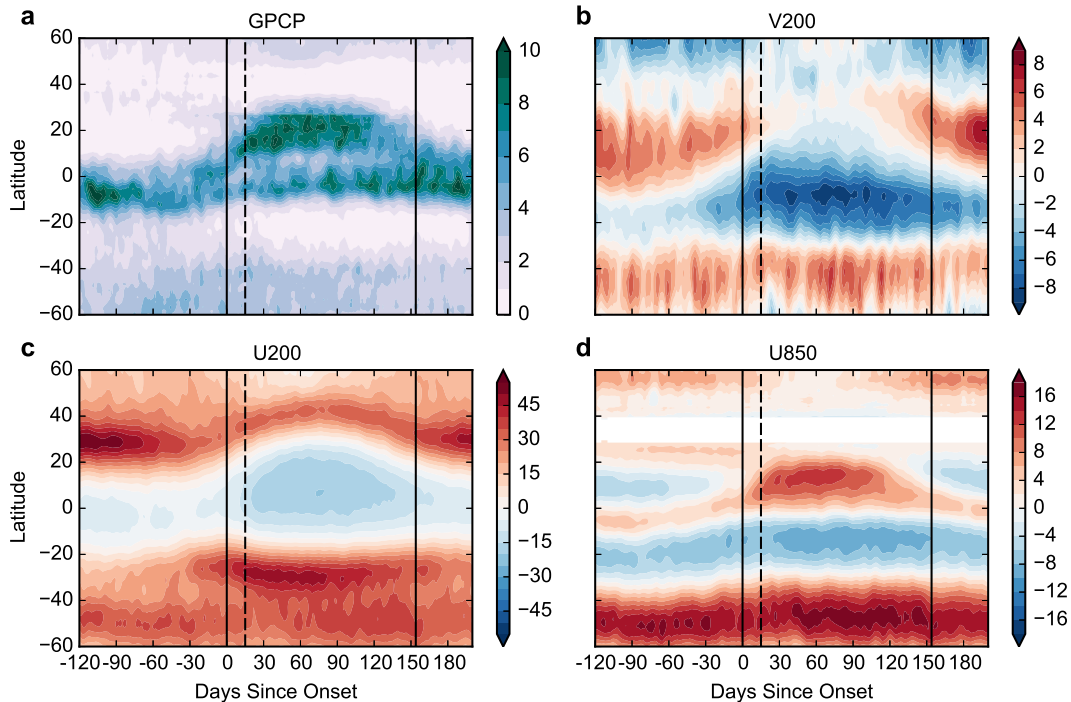


Figure 2.4: Seasonal evolution of (a) GPCP and (b-d) MERRA-2 climatological composites centered on onset date, averaged 60-100°E: (a) precipitation (mm day^{-1}), (b) 200 hPa meridional wind (m s^{-1}), (c) 200 hPa zonal wind (m s^{-1}), and (d) 850 hPa zonal wind (m s^{-1}). Vertical black lines indicate mean onset and withdrawal days, and dashed vertical black line indicates the start of the “Mature” stage (day 15). Latitudes with less than 50% of grid points above the topography are masked out in (d).

2.4 Seasonal transitions

Large-scale circulation and precipitation

Fig. 2.4 shows the seasonal evolution of climatological composites, centered on onset date, of GPCP precipitation and MERRA-2 upper-level (200 hPa) and lower-level (850 hPa) winds, averaged over 60-100°E. In each field, we see a gradual seasonal transition over approximately two months preceding onset (“Pre-Monsoon” stage), followed by an abrupt transition from day 0 to approximately day 15 (“Onset” stage). By day 15, mature monsoon conditions are well established, persisting for approximately three months (“Mature” stage). The “Withdrawal” stage is much more gradual than the Onset stage, with a gradual retreat of monsoon rains and a transition in winds occurring slowly over approximately the final 1.5 months of the season (Figs. 2.3(b, c), 2.5).

During the Pre-Monsoon stage, the SASM sector intertropical convergence zone

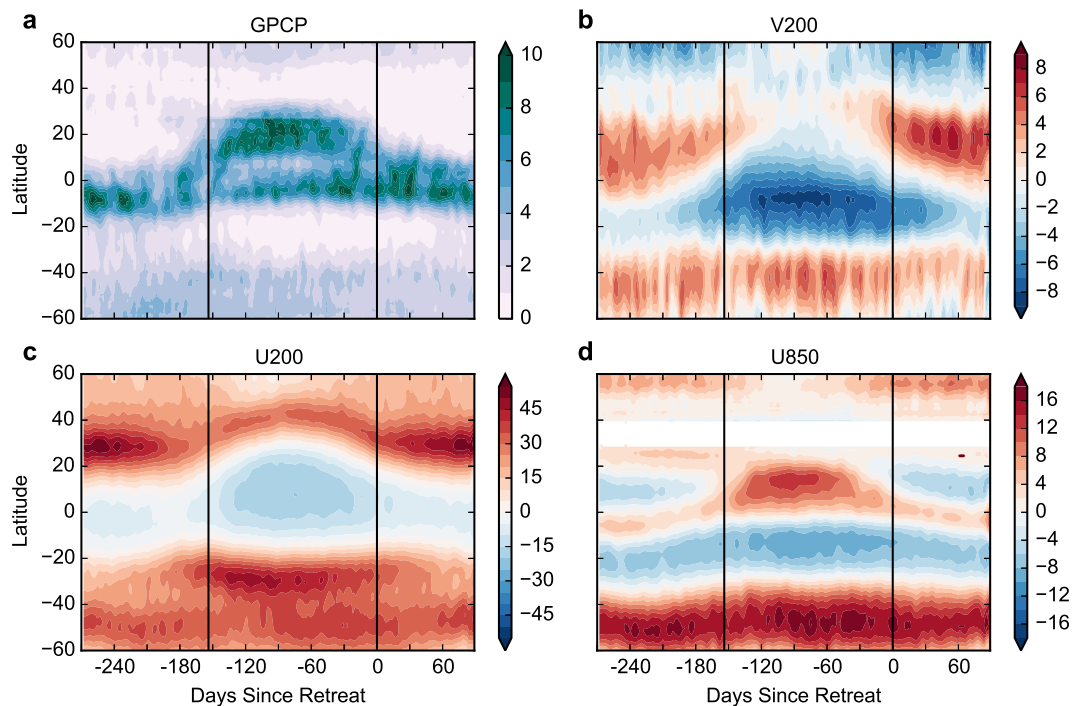


Figure 2.5: As in Fig. 2.4, but for composites centered on withdrawal date.

(ITCZ), indicated by the latitude of maximum precipitation, migrates across the equator from approximately 10°S to approximately 2°N (Fig. 2.4(a)). A corresponding transition is evident in the upper-level meridional wind (V200). The V200 field represents the upper-level flow of the large-scale meridional overturning circulation in the SASM sector, as previously shown in the Eulerian mass streamfunction for the seasonal mean monsoon (Bordoni and Schneider, 2008; Walker et al., 2015). During the Pre-Monsoon stage, there are a pair of regional Hadley cells, with the northern hemisphere (NH) cell initially stronger. As the southern hemisphere (SH) cell expands into the NH and the ITCZ migrates northward across the equator, the SH cell strengthens while the NH cell contracts and weakens (Fig. 2.4(b)). Concurrent with the transition in precipitation and V200, the upper-level westerly jet in the NH weakens and migrates northward, while a subtropical westerly jet starts to develop in the SH (Fig. 2.4(c)).

Around day 0, as the SASM moisture budget transitions from negative to positive net precipitation, we observe a basin-wide switch of the lower-level zonal winds over the Arabian Sea from negative to positive (Fig. 2.6), so that the lower-level NH tropical trade winds are reversed over the entire SASM sector (Figs. 2.4(d), 2.6). The lower-level southerly jet off the eastern coast of Africa (Somali jet) also begins

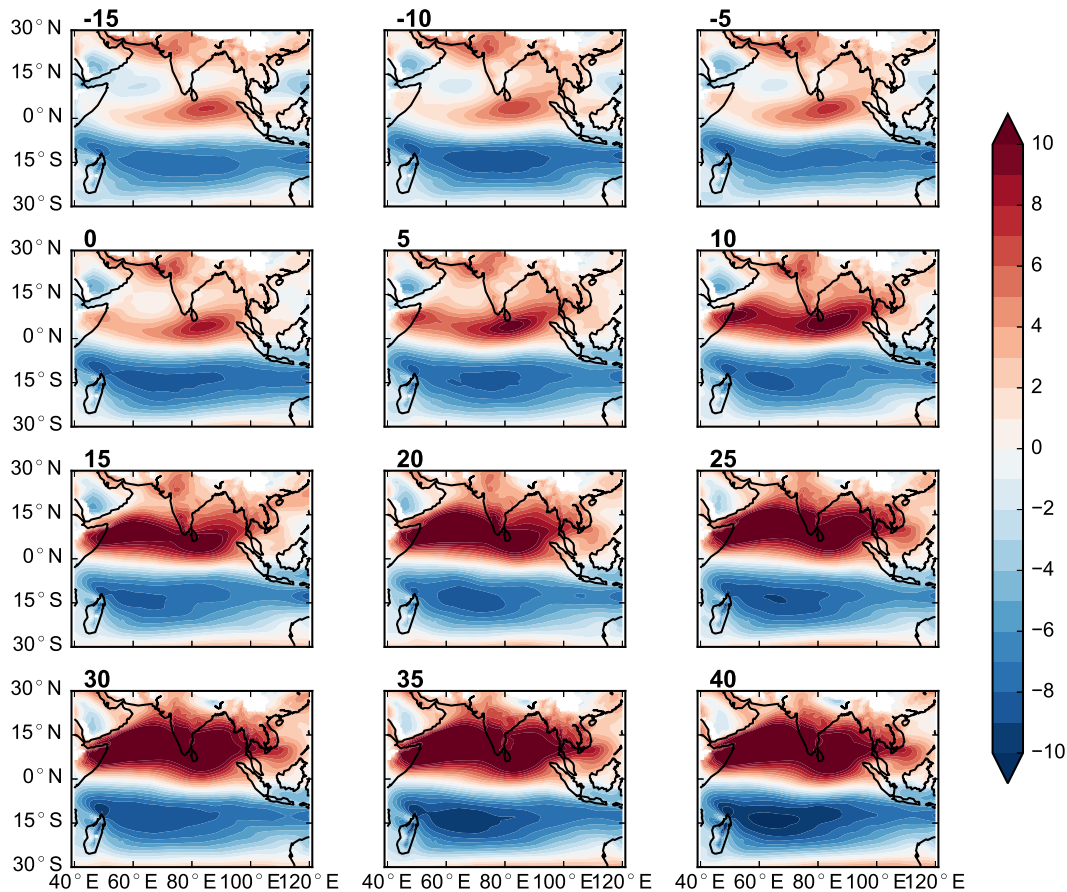


Figure 2.6: Maps of zonal wind (m s^{-1}) at 850 hPa in MERRA-2 climatological composites centered on onset date, for days -15 through 40.

to develop around day 0 over an extended longitudinal range (Fig. 2.7). By the end of the Onset stage (day 15), strong lower-level southwesterly flow has developed across the SASM region, with maximum lower-level westerly and southerly wind speeds exceeding 10 m s^{-1} (Figs. 2.6, 2.7).

During the Onset stage, the ITCZ migrates rapidly northward to approximately 15°N as the SH Hadley cell suddenly intensifies and expands deep into the NH, while the NH Hadley cell almost disappears (Fig. 2.4(a, b)). Accompanying this transition is an abrupt strengthening and expansion of upper-level tropical easterlies, northward migration of the NH upper-level westerly jet, and strengthening of the SH upper-level subtropical jet (Fig. 2.4(c)).

While consistent with previous findings for the SASM (e.g., Webster and Yang, 1992; Li and Yanai, 1996; Trenberth et al., 2005), these sector-mean seasonal transitions in precipitation and winds also bear close resemblance to seasonal transitions

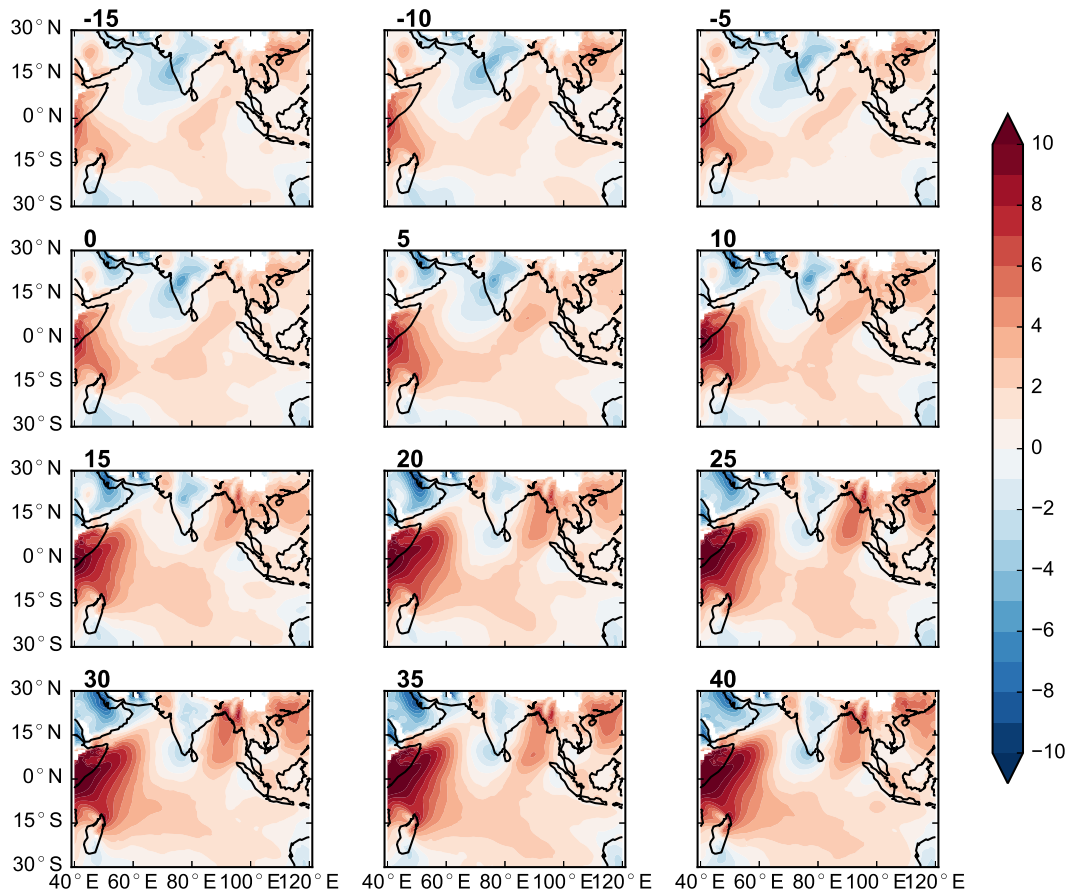


Figure 2.7: As in Fig. 2.6 but for meridional wind.

of the zonal mean Hadley circulation, which shifts from the traditional equinoctial pattern characterized by a pair of Hadley cells during equinox seasons to a solstitial pattern dominated by a single cross-equatorial winter cell and a very weak or negligible summer cell during summer seasons (Dima and Wallace, 2003; Nguyen et al., 2013; Shaw, 2014). These similarities suggest that the SASM projects strongly on the zonal mean Hadley cell during NH summer and can be understood, at least to some extent, in terms of recent theories of zonally symmetric, angular momentum-conserving overturning circulations (e.g., Gadgil, 2003; Privé and Plumb, 2007; Bordoni and Schneider, 2008).

The 15-day timescale of the SASM onset transition is very abrupt compared to the seasonal cycle of insolation, which is strongly dominated by annual and semiannual Fourier harmonics (Weickmann and Chervin, 1988; Boos and Emanuel, 2009). From day 0 to day 15, GPCP precipitation over the SASM region almost doubles, from 3.1 mm day^{-1} to 5.6 mm day^{-1} , and near-surface flow across the SASM

sector at 15°N transitions from weak westerly zonal wind (1.6 m s^{-1}) to strong westerly zonal wind (6.0 m s^{-1}) and from northerly meridional wind (-0.2 m s^{-1}) to southerly meridional wind (1.4 m s^{-1}) (Fig. 2.2(c, d)). To reproduce the same 15-day transitions in these GPCP, U850, and V850 timeseries with a best fit of the first n Fourier harmonics (based on residual least squares minimization) requires at least $n = 8$, corresponding to much higher frequency variability than the seasonal cycle of insolation.

Spatial characteristics and local onset

While our index represents transitions in the large-scale SASM rather than a single region of its domain, it is of interest to explore spatial patterns of rainfall progression at and after monsoon onset. These are shown in Fig. 2.8 through climatological composites, centered on onset date, of GPCP precipitation on various days in the monsoon season. The rain belt propagation follows a similar progression as seen in previous studies (Wang and LinHo, 2002; Wang et al., 2009): Monsoon rainfall initially develops over the eastern equatorial Indian Ocean, eastern Bay of Bengal, Andaman Sea, Myanmar, and Thailand (days 0-5). By day 15, rains are established over Kerala, followed by a gradual northward progression into the Indian subcontinent over the following weeks.

To investigate the spatial characteristics of monsoon transitions over the SASM region, and the relation of local onset (withdrawal) dates with our large-scale index, we adapt the CHP method to define local onset (withdrawal) dates at each grid point. Rather than using CMFC, which can be very noisy at individual grid points, we use GPCP cumulative precipitation, which is a smoother, non-decreasing function (since precipitation rates, unlike MFC, are nonnegative) and we average over a $4^{\circ} \times 4^{\circ}$ area centered on each grid point, to smooth small-scale variability. We apply the change point detection method described in Section 3.1 to define the local onset and withdrawal at each grid point.

Fig. 2.10(a) shows the climatological mean and standard deviation of local onset dates, where regions with non-monsoonal precipitation (June-September rainfall less than 50% of annual total, Fig. 2.1) are masked out. We see a coherent region where the local onset dates are well defined, with standard deviations less than 20 days. In Kerala, local onset dates are very close to the climatological mean large-scale onset (day 138), although the southernmost region is masked because GPCP is unable to resolve all the regional features (Fig. 2.1). Going northward from Kerala,

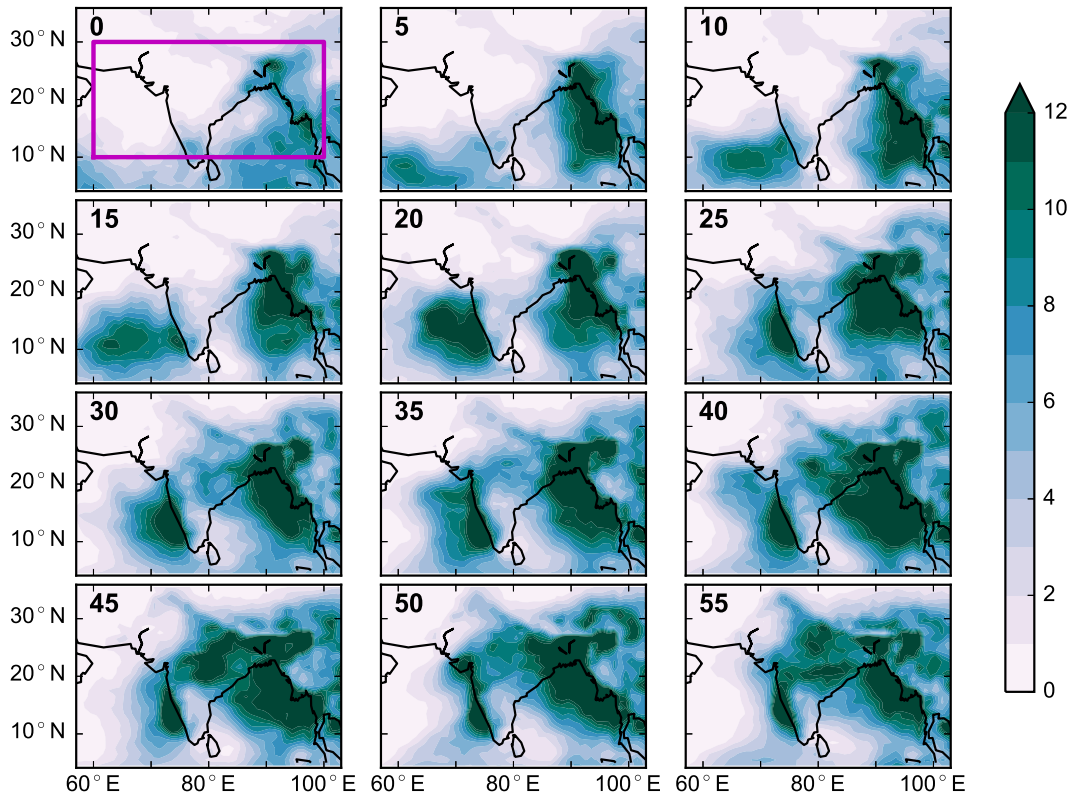


Figure 2.8: Maps of daily precipitation rates (mm day^{-1}) in GPCP climatological composites centered on onset date, for days 0 through 55. The magenta rectangle shows the averaging region for the CHP index.

local onset dates are progressively later, with central and northeastern India having local onset dates up to one month after the large-scale onset.

Fig. 2.10(b) shows the regression of local onset dates onto the large-scale onset date. Over the coherent region described for Fig. 2.10(a), the local onset dates are well correlated with the large-scale onset, with statistically significant regression coefficients of order 1 day day^{-1} over the peak rainfall regions. Thus, a later (earlier) large-scale onset corresponds to a delay (advance) of similar magnitude in local onset dates over the entire SASM region.

Toward the end of the season, the monsoon rain belts gradually withdraw southward across the region over approximately 1.5 months preceding the large-scale withdrawal date (Figs. 2.9, 2.11).

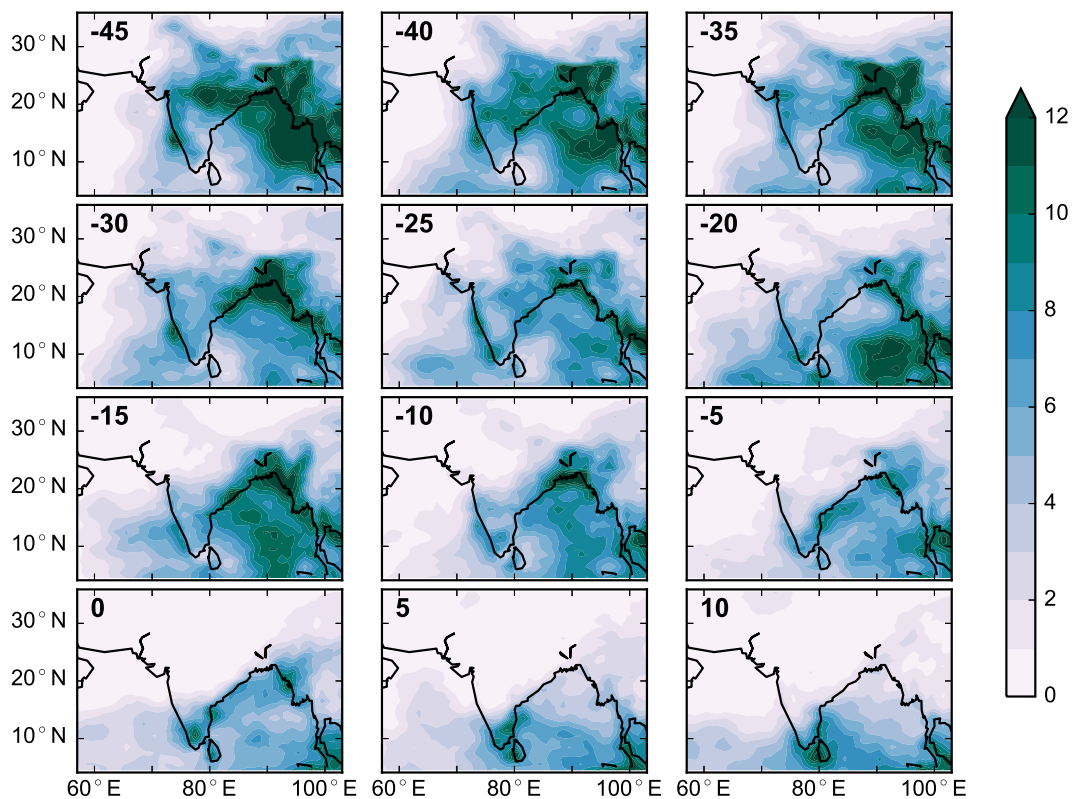


Figure 2.9: As in Fig. 2.8, but for composites centered on withdrawal date, for days -45 through 10.

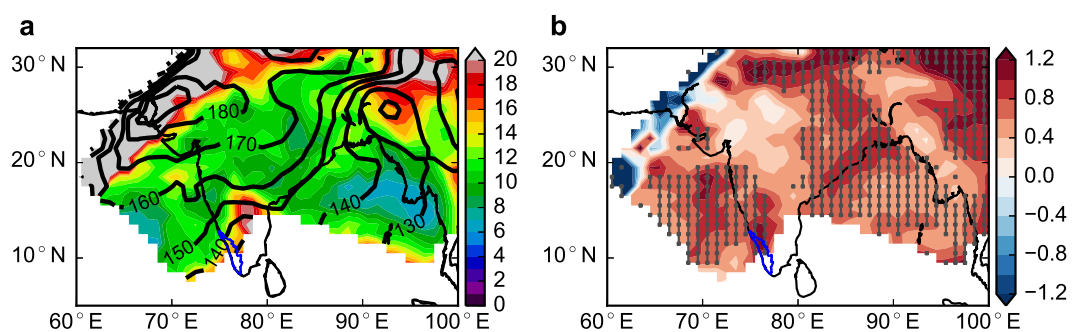


Figure 2.10: Local onset dates defined with CHP method using GPCP precipitation. (a) Climatological mean (contours) and standard deviation (colors) of onset dates. (b) Regression coefficients (day day^{-1}) of local onset dates onto large-scale CHP onset index, with gray stippling indicating the regions where the correlation is significant at the 5% level. Kerala state is outlined in blue.

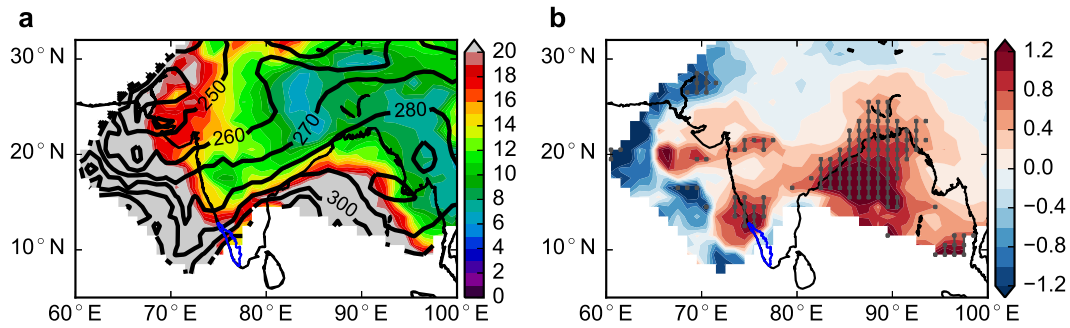


Figure 2.11: As in Fig. 2.10, but for withdrawal dates.

2.5 Conclusions

In this study, we have used the large-scale atmospheric moisture budget to propose a robust, objective definition of SASM onset and withdrawal, which captures the expected transitions in rainfall and winds. This method does not require any thresholds and is not susceptible to false onsets, making it ideal for analyzing variability and trends in SASM timing across datasets and climate models. CHP onset is highly correlated with the commonly used local operational index, the MOK, and is also correlated with subsequent variability of the SASM: earlier onsets are associated with longer monsoon seasons and enhanced seasonal rainfall.

The use of change point detection allows us to precisely characterize the duration and abruptness of monsoon onset and to construct composites of the different stages of the monsoon that are characterized by different timescales. We show that CHP-based onset and withdrawal dates correspond with transitions in the large-scale SASM atmospheric moisture budget between negative and positive net precipitation. In the SASM sector mean, seasonal transitions in precipitation and circulation are strikingly similar to those in the zonal mean Hadley circulation, with a migration of the local ITCZ from the SH to the NH concurrent with a transition from an equinox regime with meridional overturning cells in each hemisphere to a solstice regime dominated by a single, cross-equatorial winter cell, and corresponding changes in upper-level equatorial easterly jet and subtropical westerly jets.

Using the CHP method to define local onset and withdrawal dates at each grid point in the SASM domain, we find that local onset dates are approximately equal to the large-scale SASM onset date in Kerala, and are progressively later further northward, with local onset dates up to one month after large-scale onset in central and northeastern India. The local onset dates are well correlated with the large-

scale onset on interannual timescales, particularly in the peak rainfall regions, with a delay (advance) in large-scale onset associated with a delay (advance) of similar magnitude in local onset.

Future work includes using this newly defined index to quantify changes that occur in the leading energy and momentum budgets at SASM onset and withdrawal, as well as examining the reproducibility and future changes of SASM onset and withdrawal in models included in the CMIP5 archive.

2.6 Appendix: Supporting information

Domain selection

To calculate the CHP index, we use the same domain (Fig. 2.1) as in our previous study (Walker et al., 2015), which we chose to represent the large-scale monsoon, including the precipitation maxima over India and the Bay of Bengal. We analyzed the sensitivity of our results to the domain choice and found that expanding or shrinking the latitude or longitude range did not substantially alter our findings, as long as we do not extend the domain past 100°E into Southeast Asia, where the monsoon variability is distinct from the SASM (Walker et al., 2015).

We chose 10–30°N as our latitude boundaries in order to include the latitudes in which the monsoonal circulation behaves coherently across most or all of the 60–100°E sector: hence, we exclude the topography to the north and the oceanic regions to the south whose seasonal variability is not consistent with the summer monsoon (less than half of annual rainfall occurring during June–September, Fig. 2.1). Although Kerala, a major regional component of the SASM, does extend south of 10°N, the surrounding oceanic regions—comprising the majority of the SASM sector south of 10°N—feature a different seasonal behavior (Fig. 2.1). This is confirmed when we re-calculate the CHP onset extending the domain to 5–30°N: the correlation with MOK actually decreases from 0.82 (Section 2.3) to 0.76, indicating that 10°N is an appropriate southern boundary to represent the large-scale features we focus on here.

Interannual Variability

Table 2.2 shows that monsoon season length is strongly correlated with both onset date (-0.76) and withdrawal date (0.80), indicating that longer monsoon seasons are associated with earlier onset and later withdrawal, consistent with previous findings (Goswami, 2005; Cook and Buckley, 2009). Early onset, late withdrawal, and longer season length are also correlated with increased cumulative rainfall

over the monsoon season (Fig. 2.12, Table 2.2). This enhanced seasonal rainfall is approximately balanced by an increase in evaporation, leading to no significant correlations in the net precipitation (Fig. 2.12). The correlations in seasonal mean rates (Fig. 2.13, Table 2.2), while in some cases less robust, are all in the opposite direction as the correlations in the seasonal totals, indicating that season length—rather than changes in daily rates—is the primary cause for the observed correlations in Fig. 2.12. Thus, we conclude that the enhanced seasonal rainfall associated with early onsets, late withdrawals, and longer seasons is due to the increase in season length and is partially, but not completely, offset by a slight reduction in daily rainfall rates.

To investigate interannual variability in SASM timing associated with El Niño–Southern Oscillation (ENSO) variability, we use the Niño 3 index provided by the National Oceanic and Atmospheric Administration (NOAA) Climate Prediction Center (CPC) for the years 1980–2015. This index is a monthly average of sea surface temperatures from the Extended Reconstructed Sea Surface Temperature Version 4 (ERSST; Huang et al., 2015), averaged over the region 5°S – 5°N , 150°W – 90°W . We also conducted our analysis with the commonly used Niño 3.4 index (same as Niño 3 but averaged over 5°S – 5°N , 170°W – 120°W) and the results are all qualitatively similar but with weaker correlations, so we present the Niño 3 index, which displays the strongest correlations. We find that later onset dates are correlated with warm ENSO conditions in the previous March–May (MAM) and concurrent June–August (JJA), and shorter monsoon seasons are correlated with warm ENSO conditions in JJA (Table 2.2), consistent with previous findings (Fasullo and Webster, 2003; Goswami, 2005; Cook and Buckley, 2009; Noska and Misra, 2016).

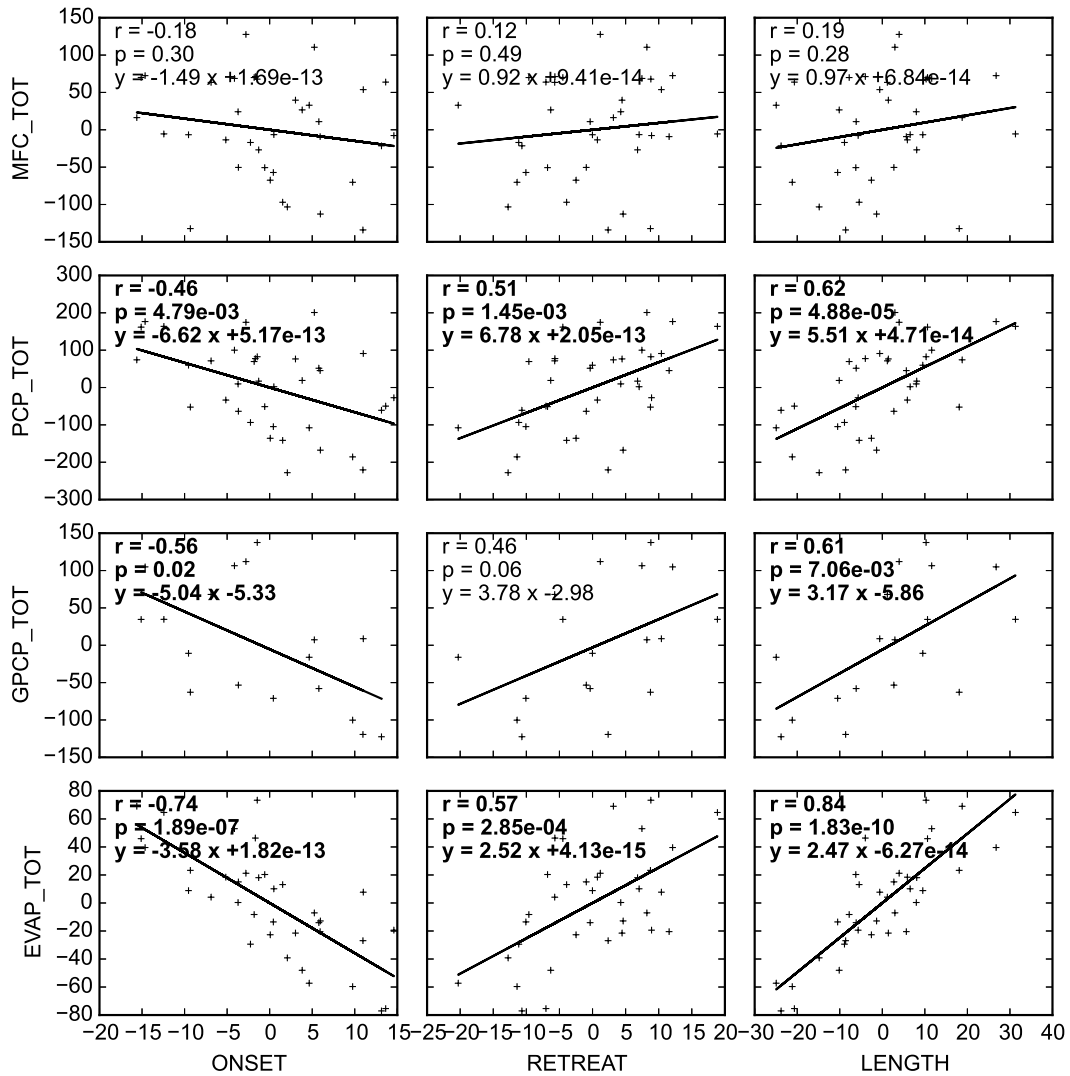


Figure 2.12: Scatter plots and linear regressions of detrended monsoon season totals (mm), from onset to retreat in each year, of MERRA-2 moisture flux convergence (MFC_TOT), MERRA-2 precipitation (PCP_TOT), GPCP precipitation (GPCP_TOT), and MERRA-2 evaporation (EVAP_TOT), averaged 10–30°N, 60–100°E vs. detrended SASM onset, retreat, and season length (days). Note that the GPCP dataset is shorter than MERRA-2, so higher correlation coefficients are required for statistical significance at the 5% level.

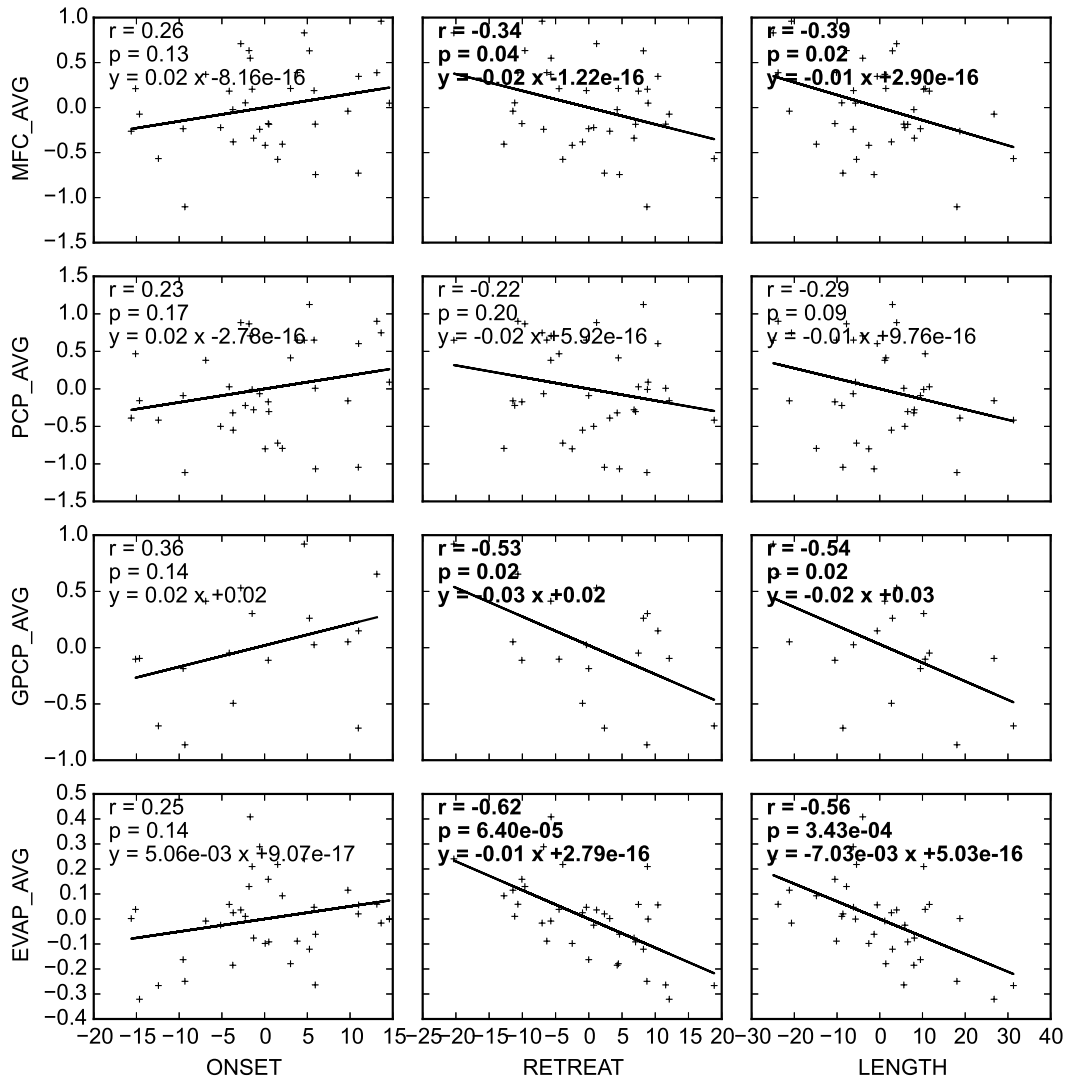


Figure 2.13: Scatter plots and linear regressions of detrended seasonal mean rates (mm day^{-1}), averaged from onset to retreat in each year, of MERRA-2 moisture flux convergence (MFC_AVG), MERRA-2 precipitation (PCP_AVG), GPCP precipitation (GPCP_AVG), and MERRA-2 evaporation (EVAP_AVG), averaged $10\text{--}30^\circ\text{N}$, $60\text{--}100^\circ\text{E}$ vs. detrended SASM onset, retreat, and season length. Note that the GPCP dataset is shorter than MERRA-2, so higher correlation coefficients are required for statistical significance at the 5% level.

Table 2.2: Interannual correlation coefficients between CHP indices, GPCP seasonal total and mean rainfall (from onset to withdrawal each year, averaged 10–30°N, 60–100°E), and ENSO indices. Values significant at the 5% level are indicated in bold. Note that the GPCP dataset is shorter than the other indices, so higher correlation coefficients are required for statistical significance at the 5% level.

	Onset Date	Withdrawal Date	Season Length
Onset Date	1.00	-0.22	-0.76
Withdrawal Date	-0.22	1.00	0.80
Season Length	-0.76	0.80	1.00
GPCP Seasonal Total Rainfall	-0.56	0.46	0.61
GPCP Seasonal Mean Rainfall	0.36	-0.53	-0.54
NINO3 MAM	0.41	0.08	-0.20
NINO3 JJA	0.39	-0.24	-0.40

Chapter 3

SEASONAL VARIABILITY

Abstract

We analyze seasonal changes in the dynamics and thermodynamics of the South Asian summer monsoon (SASM) in atmospheric reanalysis data, to evaluate the extent to which emerging theoretical frameworks are consistent with the observed monsoon. Climatological composites reveal that at monsoon onset, an abrupt strengthening and northward migration of the maximum in sub-cloud equivalent potential temperature (θ_{eb}) accompany the rapid northward movement of the monsoon rainbelt. These changes in θ_{eb} are driven by changes in near-surface specific humidity, rather than changes in near-surface temperature, whose gradient in fact decreases at monsoon onset, inconsistent with the traditional sea-breeze paradigm for the monsoon. These findings are inconsistent with the traditional paradigm of the monsoon as a sea breeze circulation and confirm the convectively coupled view of the SASM circulation as an energetically-direct overturning circulation as more fundamental for the understanding of monsoon dynamics.

Providing further support to this emerging view, we show that the SASM sector mean circulation at monsoon onset undergoes a rapid transition from an equinox circulation with a pair of tropical overturning cells, to a solstice circulation dominated by a strong cross-equatorial monsoonal cell and negligible overturning cell in the northern hemisphere. This transition corresponds to a transition in the leading order momentum budget, from an eddy-dominated equinox regime to a highly nonlinear monsoon regime which approaches conservation of angular momentum. These transitions are similar to those seen in idealized zonally symmetric studies of aquaplanet monsoons, suggesting that eddy-mean flow feedbacks identified in those studies may be acting in the SASM sector, and may contribute to the abruptness of the SASM onset. Our findings highlight the importance of nonlinear dynamics in the seasonal evolution of the SASM circulation and suggest that some fundamental aspects of the observed monsoon can be understood in the absence of land-sea contrast or other zonal asymmetries.

3.1 Introduction

One of the most striking features of the South Asian summer monsoon (SASM) is its rapid onset, with abrupt changes in circulation and precipitation as the rainy season begins (e.g., Walker and Bordoni, 2016). However, there remains much debate over which mechanisms drive these transitions and render them rapid. Proposed onset mechanisms have included a threshold response to a critical temperature distribution (e.g., Plumb and Hou, 1992), inertial instability of cross-equatorial flow (e.g., Krishnakumar and Lau, 1997; Tomas and Webster, 1997), wind-evaporation feedbacks (e.g., Minoura et al., 2003; Boos and Emanuel, 2008a; Boos and Emanuel, 2008b), and interactions with atmospheric intraseasonal oscillations (Wu and Zhang, 1998; Goswami et al., 2006b; Li and Pan, 2006; Hung and Hsu, 2008).

Several modeling studies have explored implications of dynamical and thermodynamical constraints on monsoonal circulations. One important class of theories builds on axisymmetric models of idealized Hadley circulations that exist in the absence of large-scale eddies and other zonal asymmetries. The widely accepted paradigm of these axisymmetric Hadley circulations is based on the nearly inviscid theory by Held and Hou (1980), who emphasized the importance of nonlinear advection and conservation of angular momentum in the upper branches of the Hadley cell and provided scalings for its width, strength, and heat and momentum transport. The dynamical constraint of conservation of angular momentum in the upper troposphere has been argued to be also relevant in axisymmetric models forced by a localized off-equatorial heating with zero gradients across the equator (Plumb and Hou, 1992; Emanuel, 1995), in which a deep, angular momentum-conserving, cross-equatorial Hadley circulation develops above a threshold forcing amplitude.

Recent work has however emphasized the importance of baroclinic eddies, which are neglected in axisymmetric theories, in the dynamics of the Hadley cell, with associated eddy momentum flux divergence forcing the zonally-averaged circulation to deviate from conservation of angular momentum (e.g., Walker and Schneider, 2006; Schneider, 2006). Interactions between baroclinic eddy fluxes and the tropical overturning circulation have also been argued to be implicated in the onset (and its rapidity) of large-scale monsoons by Schneider and Bordoni (2008) and Bordoni and Schneider (2008). More specifically, these studies suggest that the onset of large-scale monsoons corresponds with a transition in the tropical angular momentum budget between an equinox regime, in which the circulation is driven by extratropical large-scale eddies, to a monsoon regime, in which the circulation approaches

conservation of angular momentum and more directly responds to energetic constraints. Feedbacks between large-scale extratropical eddy fluxes of momentum, upper-level winds, sub-cloud moist static energy, and overturning circulation can render the transition rapid, leading to an abrupt monsoon onset, even in aquaplanet simulations with no surface inhomogeneities. Necessary for the development of these aquaplanet monsoons is not an imposed land-sea contrast, but rather a surface whose thermal inertia is low enough to allow for surface fluxes, and with them the circulation, to adjust rapidly.

In the zonal mean circulation, an abrupt transition from boreal spring to summer is also observed. Shaw (2014) finds that this seasonal change corresponds with a transition to a wave-dominated regime, in which planetary-scale wave latent heat and momentum transport dominate over zonal mean transport. Hypothesizing that these planetary-scale waves may be associated with monsoon-anticyclone systems and may be a driving mechanism in the seasonal transition, Shaw (2014) uses an idealized aquaplanet model to investigate whether zonally asymmetric heating perturbations in the subtropics can produce a transition in the zonal mean circulation similar to the observed seasonal transition. Above a certain perturbation amplitude, the anomalous circulation response and a localized reversal in absolute vorticity in the NH tropical upper troposphere are sufficient to trigger a transition to a solstice regime similar to that observed in the zonal mean in boreal summer, in which the circulation is dominated by a strong cross-equatorial winter cell which expands deep into the summer hemisphere.

The results from these earlier studies raise several questions: To what extent are the zonally-symmetric mechanisms discussed in Schneider and Bordoni (2008) and Bordoni and Schneider (2008) relevant to observed monsoons, which are inherently zonally localized? What is the leading order angular momentum balance in the SASM sector, and how does it change at monsoon onset? How do circulation changes in the SASM sector project onto circulation changes in the zonal mean? Are the sector and zonal mean circulations driven by similar dynamics?

In this study, we address these questions by using reanalysis data to investigate the seasonal transitions in large-scale dynamics and thermodynamics of the SASM. One specific goal is to explore the mechanisms governing its seasonal evolution and to link the SASM sector mean changes to the seasonal transitions of the zonal mean circulation. We construct climatological composites, centered on SASM onset date, to analyze important aspects of the energetics and momentum balance of

the circulation throughout the SASM sector, including atmospheric fields remote to the monsoon, which affect the large-scale transports of momentum and energy. Comparing SASM composites with predictions from theoretical studies and idealized simulations, we evaluate the extent to which these theoretical frameworks are consistent with the observed seasonal variability of the SASM.

3.2 Data and methods

For atmospheric data, we use NASA’s Modern-Era Retrospective analysis for Research and Applications, Version 2 (MERRA-2; Rienecker et al., 2011; Bosilovich et al., 2015), years 1980–2015, at a horizontal grid resolution of 0.5° (latitude) \times 0.625° (longitude). To assess seasonal variability, we compute daily mean values from the 3-hourly reanalysis. Pressure-level data are extracted on all 42 levels, except for the momentum budget calculations (Section 3.4), which are extracted at 17 pressure levels (1000, 925, 850, 775, 700, 600, 500, 400, 300, 250, 200, 150, 100, 70, 50, 30, and 20 hPa) for computational efficiency. For moisture and energy fluxes, we use the mass-weighted vertically integrated moisture fluxes from the reanalysis output; because of improvements in MERRA-2, global conservation of dry atmospheric mass is maintained in the data assimilation system, so these fluxes satisfy mass balance constraints (Takacs et al., 2015).

For precipitation, we use Global Precipitation Climatology Project Version 1.2 One-Degree Daily (GPCP; Huffman et al., 2001; Huffman et al., 2016) daily estimates at $1^\circ \times 1^\circ$ grid resolution, from 1997 (first complete year available) through October 2015 (final month available). For ocean mixed layer depths, we use a $2^\circ \times 2^\circ$ gridded monthly climatology from the Institut français de recherche pour l’exploitation de la mer (Ifremer), based on temperature profiles from the National Oceanographic Data Center’s World Ocean Database (WOD), the World Ocean Circulation Experiment (WOCE) database, and the Argo program (de Boyer Montégut et al., 2004).

Building on our previous work on SASM interannual variability (Walker et al., 2015) and onset/withdrawal indices (Walker and Bordoni, 2016), we define the SASM sector as 60–100°E. We chose this longitude range to represent the large-scale monsoon, including the precipitation maxima over India and the Bay of Bengal, and encompassing the broad sector where the circulation behaves coherently as an overturning circulation with the majority of mass transport within the meridional-vertical plane. As we will show later (Section 3.3), west of 60°E, the circulation is dominated by the lower-level Somali jet, rather than the meridional overturning

circulation of the SASM. East of 100°E , the monsoon in Southeast Asia displays variability distinct from the SASM (Walker et al., 2015).

To define onset and withdrawal of the SASM, we use a dynamical index based on the vertically integrated atmospheric moisture flux convergence (MFC) that we have recently introduced (Walker and Bordoni, 2016). Briefly, the change point index (CHPI) is computed in each year using a timeseries of MFC, averaged over $10\text{--}30^{\circ}\text{N}$, $60\text{--}100^{\circ}\text{E}$ (Fig. 3.1), to compute a cumulative timeseries of MFC accumulated since January 1 (CMFC), and then applying a two-phase linear regression of CMFC vs. day of year to detect change points over two ranges: days 1-250 for onset, and days 200-400 for withdrawal. We chose the averaging domain to correspond with the SASM sector in longitude and we selected the latitude limits to focus on the subtropical monsoonal precipitation, excluding the topography to the north and the oceanic regions to the south whose seasonal variability is not consistent with the summer monsoon, with less than half of the annual rainfall occurring during June–September (Fig. 3.1).

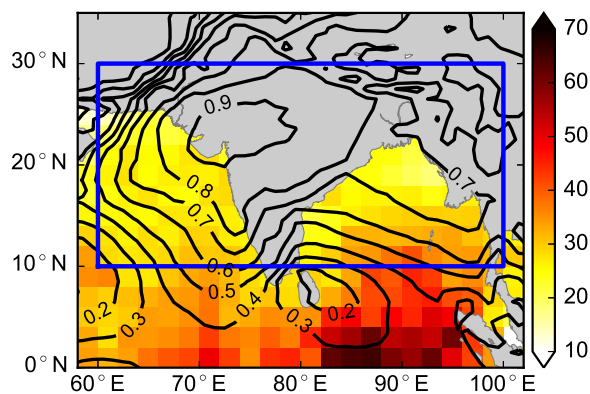


Figure 3.1: June–September (JJAS) fraction of yearly rainfall in GPCP climatology (contours) and ocean mixed layer depths (m) in Ifremer May climatology (colors). The blue rectangle shows the averaging region for the SASM onset index.

The climatological mean CHPI onset date is May 18, with a standard deviation of 8 days (Walker and Bordoni, 2016). It precedes typical onset indices by about 14 days because the change point represents the first day of the onset transition, rather than the first day when the monsoon rain and winds are well established. This index robustly captures the expected seasonal transitions in SASM winds and precipitation, with onset marking a sharp increase in rainfall over the SASM domain and initiation of strong lower-level southwesterly flow (Fig. 3.2(a,b), Walker and Bordoni, 2016).

Onset (withdrawal) also corresponds to a transition in the atmospheric moisture budget from negative to positive (positive to negative) net precipitation (Walker and Bordoni, 2016); hence the summer monsoon season defined by this index corresponds to the time period when net precipitation averaged over the SASM domain is positive.

To examine SASM seasonal variability, particularly the transitions associated with monsoon onset, we compute climatological composites of daily atmospheric fields, centered on the CHPI onset date in each year, so that day 0 corresponds to the onset date. We smooth these composites with a centered 5-day moving average.

3.3 Atmospheric circulation and thermodynamics

In our previous study (Walker and Bordoni, 2016), we described important aspects of the large-scale SASM seasonal evolution, focusing primarily on precipitation and lower-level winds to assess the performance of our newly defined index. We identified the stages of the SASM as “Pre-Monsoon” (two months preceding CHPI onset), “Onset” (an abrupt 15 day transition starting at CHPI onset), “Mature” (approximately three months following the Onset stage), and “Withdrawal” (a gradual transition occurring over approximately 1.5 months preceding CHPI withdrawal). Here we expand this analysis to a more complete description of the seasonal transitions in dynamics and thermodynamics of the SASM.

Precipitation and meridional overturning circulation

We characterize the SASM meridional overturning circulation (i.e., regional Hadley cells) by computing the Eulerian mass streamfunction (ψ) averaged in longitude across the SASM sector. The seasonal evolution of this circulation, along with precipitation and other atmospheric fields averaged over the SASM sector, are shown in Figs. 3.2, 3.3 and 3.4.

The Pre-Monsoon stage is characterized by a gradual transition during which the northern hemisphere (NH) Hadley cell contracts and the southern hemisphere (SH) Hadley cell strengthens and becomes cross-equatorial (Figs. 3.2(b), 3.3, 3.4(b)). The migration into the NH hemisphere of the SH Hadley cell’s ascending branch is accompanied by a corresponding migration in the sector mean intertropical convergence zone (ITCZ, indicated by the latitude of maximum precipitation) (Fig. 3.4(a)). From days 0 to 15 (Onset stage), changes in the overturning circulation become significantly more rapid, with the SH Hadley cell abruptly strengthening and expanding deep into the NH, and the NH Hadley cell contracting, weakening, and almost dis-

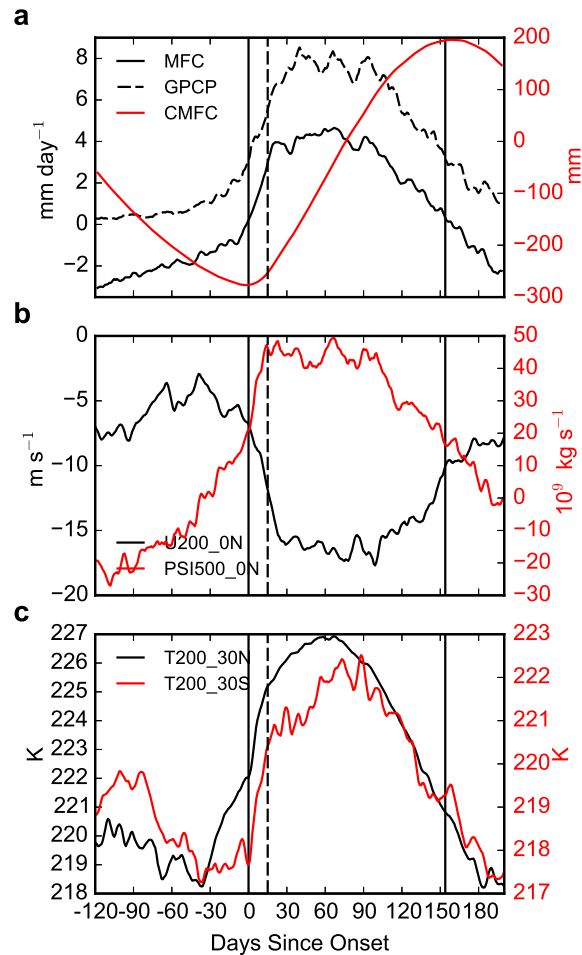


Figure 3.2: Climatological composites of MERRA-2 (1980-2015) and GPCP (1997-2015) daily fields centered on onset date, averaged $60\text{-}100^\circ\text{E}$, with vertical black lines indicating mean onset and withdrawal days, and dashed vertical black line indicating the start of the “Mature” stage (day 15). (a) Moisture budget averaged $10\text{-}30^\circ\text{N}$, showing MFC (solid black, mm day^{-1}), GPCP (dashed black, mm day^{-1}), and CMFC (red, mm). (b) 200 hPa zonal wind (black, m s^{-1}) and 500 hPa streamfunction (red, 10^9 kg s^{-1}) at 0°N . (c) 200 hPa atmospheric temperature at 30°N (black, K) and 30°S (red, K). Panel (a) is adapted from Walker and Bordoni (2016).

appearing (Figs. 3.2(b), 3.3, 3.4(b)). During this stage, heavy rainfall develops over the northeastern Arabian Sea and Bay of Bengal, and nearby coastal regions (Fig. 3.5(a)), and the sector mean ITCZ migrates rapidly northward to approximately 15°N (Fig. 3.4(a), 3.5(a)). By Day 15, mature monsoon conditions are well established, persisting for several months until tapering off into a gradual retreat (Fig. 3.4).

These seasonal transitions in SASM sector mean precipitation and circulation closely

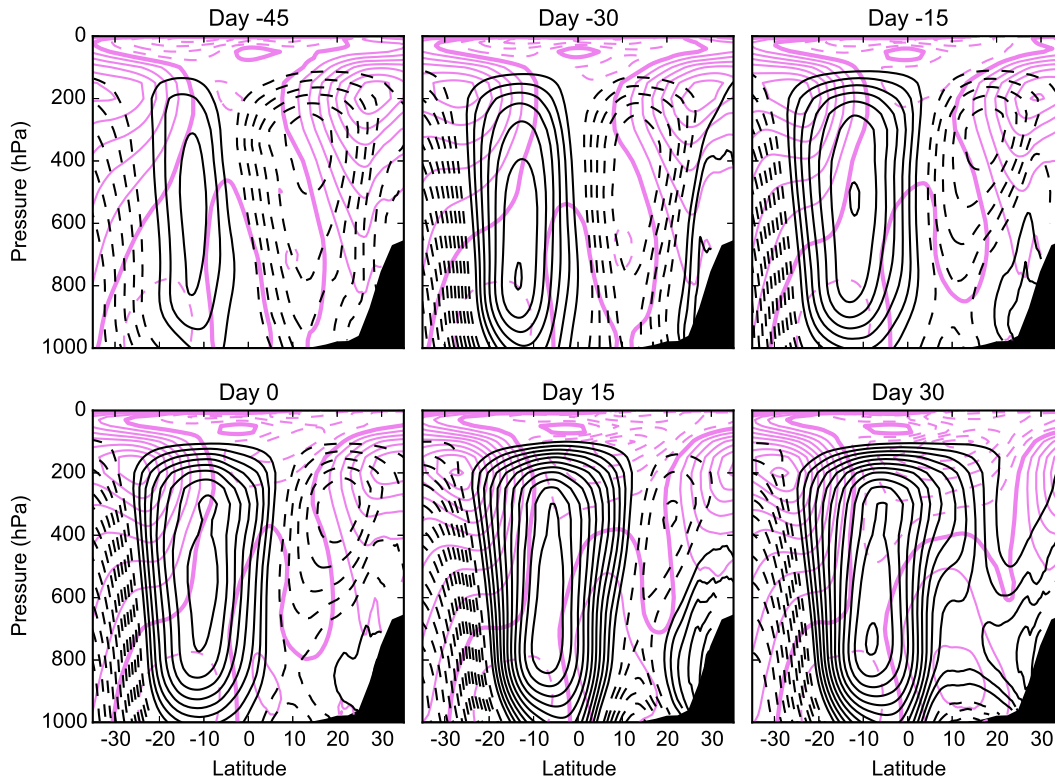


Figure 3.3: Latitude-pressure contours of SASM sector mean streamfunction (black, contour interval $5 \times 10^9 \text{ kg s}^{-1}$) and zonal wind (violet, contour interval 5 m s^{-1}), on days -45, -30, -15, 0, 15, and 30. Positive contours are solid and negative contours are dashed. The zero line is indicated by a heavy solid contour for the zonal wind, and is omitted for the streamfunction. Sector mean topography is shaded in black.

resemble those of the zonal mean Hadley circulation, from an equinox regime with two overturning cells, to a solstice regime dominated by a cross-equatorial SH cell and near disappearance of NH cell, accompanied by a northward migration of ITCZ (Dima and Wallace, 2003; Nguyen et al., 2013; Shaw, 2014). In the following sections, we will further explore the dynamics of this transition within the framework of the large-scale momentum and energy budgets. This is the first study to do so in the SASM sector, rather than in the global zonal mean. Implications for the theoretical understanding of monsoons will also be discussed.

Upper-level zonal winds and temperature

While their relevance to the observed Earth's zonally averaged Hadley cells has been questioned by recent work (e.g., Schneider, 2006; Walker and Schneider, 2006), there is evidence that axisymmetric theories of tropical overturning circulations

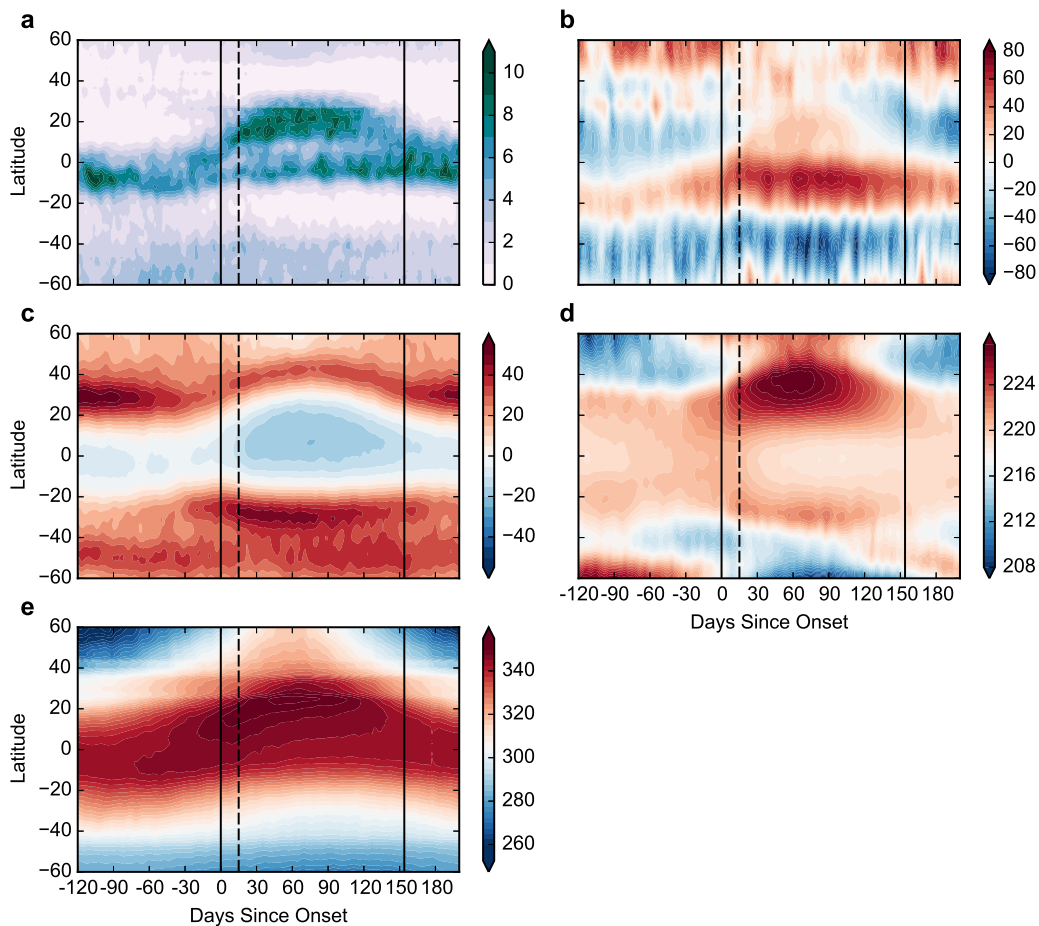


Figure 3.4: Seasonal evolution of (a) GPCP and (b-e) MERRA-2 climatological composites centered on onset date, averaged 60–100°E: (a) precipitation (mm day^{-1}), (b) 500 hPa streamfunction (10^9 kg s^{-1}), (c) 200 hPa zonal wind (m s^{-1}), (d) 200 hPa temperature (K), and (e) near-surface equivalent potential temperature (K). Vertical black lines indicate mean onset and withdrawal days, and dashed vertical black line indicates the start of the “Mature” stage (day 15). Panels (a, c) are adapted from Walker and Bordoni (2016).

might provide insight into the dynamics and response to perturbations of large-scale monsoonal, cross-equatorial circulations (e.g., Privé and Plumb, 2007; Bordoni and Schneider, 2008; Schneider and Bordoni, 2008). In the limit of angular momentum conservation, these cross-equatorial circulations are characterized by strong upper-level easterly flow in the deep tropics, flanked by a strong subtropical westerly jet in the winter hemisphere, and a weaker westerly jet in the summer hemisphere (Lindzen and Hou, 1988). The establishment of a monsoonal cross-equatorial circulation in the SASM sector at monsoon onset is accompanied by changes in upper-tropospheric winds that are consistent with this theoretical framework (Fig. 3.4). During the early

weeks of the Pre-Monsoon stage, when the NH overturning cell is cross-equatorial, the NH subtropical jet is much stronger than the SH subtropical jet. In the weeks leading up to onset, as the ITCZ migrates north of the equator and the SH cell becomes cross-equatorial, the NH subtropical jet weakens while the SH subtropical jet strengthens. During the Onset stage, as the SH cell rapidly expands deep into the NH, with its ascending branch migrating far from the equator, there is an abrupt strengthening and expansion of equatorial upper-level easterlies (Fig. 3.2(b), 3.4(c), 3.5(b)), and the SH subtropical jet also strengthens abruptly (Fig. 3.4(c)). A more detailed analysis of the momentum budget will be provided in Section 3.4.

Another feature of cross-equatorial angular momentum conserving circulations is the tendency to symmetrize upper-level atmospheric fields between the northern and southern hemispheres (Lindzen and Hou, 1988). Upper-level temperatures and winds in the SASM sector show that during the summer monsoon season, the SASM circulation exhibits such a symmetrization between hemispheres, with a subtropical maximum in each hemisphere and equatorial minimum (Fig. 3.4(c, d)). While an asymmetry exists between the temperature maxima in the NH and SH, possibly due to stronger wintertime extratropical eddy heat fluxes in the SH, the fields are remarkably symmetric in their seasonal evolution with the onset and progression of the SASM (Fig. 3.2(c)).

During the Onset stage, this pattern of subtropical maxima in each hemisphere intensifies and broadens, with the maxima in both U200 and T00 strengthening and shifting poleward from day 0 to day 15; even the day 0 to day 15 anomalies in sector mean U200 and T200 display the same pattern, with subtropical maxima in each hemisphere (Fig. 3.5). Thus, this tendency to symmetrize between hemispheres is evident in the SASM seasonal evolution, including the abrupt onset transition.

Quasi-equilibrium

Monsoon dynamics in a convective quasi-equilibrium framework have been explored in both modeling and observational studies (e.g., Emanuel, 1995; Chou et al., 2001; Neelin, 2007; Privé and Plumb, 2007). These studies argue that the maximum subcloud equivalent potential temperature (θ_{eb}) is approximately co-located with the peak monsoonal precipitation. This approximate co-location has been shown to hold in most monsoons regions both in the climatological mean (Nie et al., 2010) as well as on interannual timescales (Hurley and Boos, 2013; Walker et al., 2015). Does the maximum subcloud equivalent potential temperature track the monsoonal

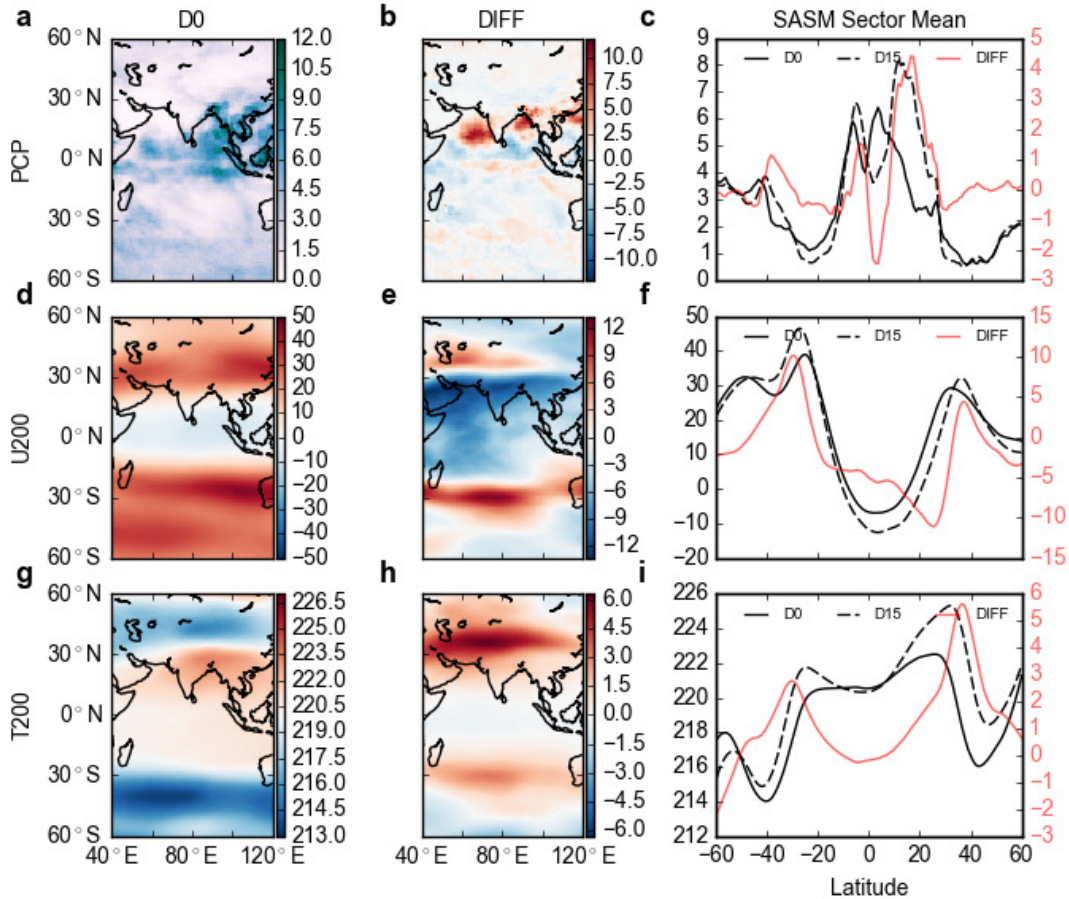


Figure 3.5: Maps of precipitation (a–c, mm day⁻¹), 200 hPa zonal wind (d–f, m s⁻¹), and 200 hPa temperature (g–i, K) on day 0 (a, d, g) and the anomaly from day 0 to day 15 (b, e, h). SASM sector mean fields vs. latitude on days 0, 15, and the anomaly from day 0 to 15 are shown in (c, f, i).

precipitation on seasonal time scales as well? If so, are the related changes primarily associated with variations in temperature or humidity? To answer these questions, we compute θ_{eb} from temperature and specific humidity extracted from the lowest model level in the MERRA-2 terrain-following hybrid-sigma coordinates. We find that the maximum in θ_{eb} does closely follow the ITCZ on seasonal timescales, migrating from SH to NH in the Pre-Monsoon stage, and abruptly strengthening and migrating into the NH subtropics during the Onset stage (Fig. 3.4). We also see the coupling between θ_{eb} and upper-level temperature (Fig. 3.4), which is also consistent with the quasi-equilibrium view of convection maintaining the vertical temperature structure close to a moist adiabat on relatively fast time scales. Fig. 3.6 shows that during the Onset stage, the strengthening and northward shift in maximum

θ_{eb} is due to changes in atmospheric near-surface humidity, with the near-surface temperature over India actually decreasing. This confirms how the importance of surface sensible heat fluxes as a fundamental driver of the monsoon has been over-emphasized in the literature and how latent heat fluxes are at least equally as, if not more important than, sensible heat fluxes for the monsoon strength (e.g., Molnar et al., 2010). In the convectively coupled view of large-scale circulations, monsoons are energetically-direct circulations that export the energy that enters into the atmospheric column through surface (dry and latent) enthalpy fluxes and radiative fluxes. Thus, near-surface temperatures are not an external forcing, but are a byproduct of the circulation itself. At monsoon onset, as the circulation strengthens and rainfall increases, the land-sea contrast in near-surface temperatures decreases but the near-surface moist enthalpy gradient increases.

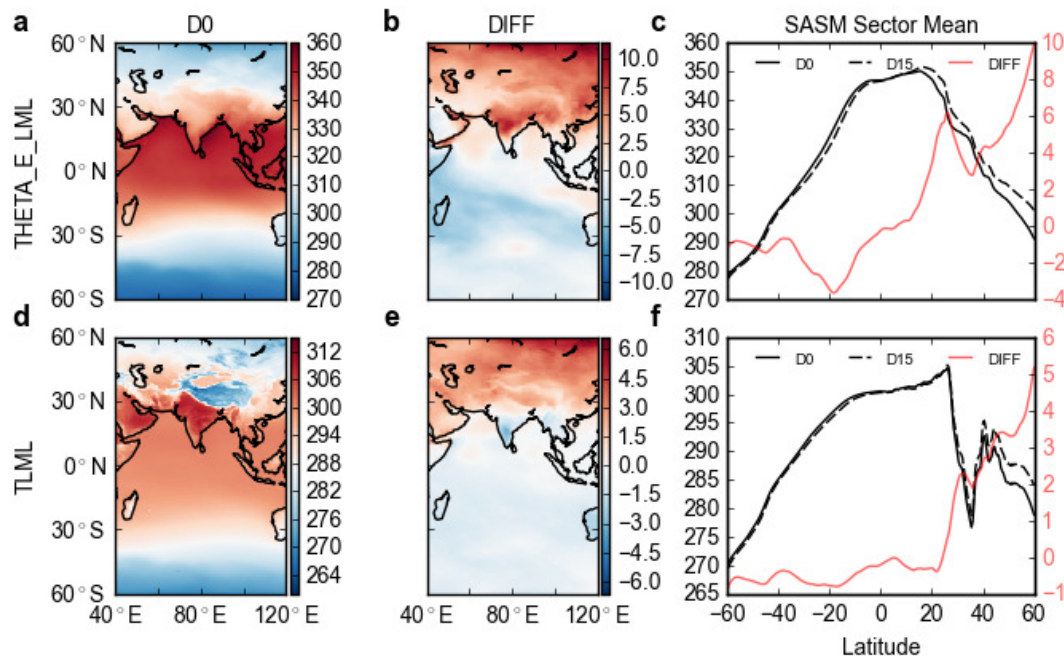


Figure 3.6: As in Fig. 3.5, but for near-surface equivalent potential temperature (a–c, K) and near-surface temperature (d–f, K).

Cross-equatorial energy transport

Recent studies of the zonal mean circulation have emphasized the importance of the energy budget in determining the position and variability of the zonal mean ITCZ on timescales from seasonal through interannual and longer (e.g., Kang et al., 2008; Kang et al., 2009; Frierson and Hwang, 2012; Donohoe et al., 2013; Donohoe et al., 2014; Frierson et al., 2013; Bischoff and Schneider, 2014; Schneider et al., 2014;

Adam et al., 2016). In this framework, energy imbalances between the northern and southern hemispheres, such as those associated with the seasonal cycle of insolation, are compensated by meridional transports of energy by the ocean and atmosphere from the warmer hemisphere to the cooler hemisphere. In the atmosphere, this cross-equatorial transport of moist static energy (MSE: $h = C_p T + gz + L_v q_v$) is primarily accomplished by the Hadley circulation. In the lower branch of the Hadley circulation, MSE transport is toward the ascending branch of the circulation (i.e., toward the ITCZ), and is dominated by the moist enthalpy ($C_p T + L_v q_v$). In the upper branch, MSE transport is in the opposite direction, away from the ITCZ, and is dominated by the geopotential (gz). Overall, the opposing transports tend to cancel each other out, but the upper branch dominates slightly, leading to a net meridional transport of MSE in the direction of the upper branch, away from the ITCZ (Held, 2001). Thus, an ITCZ in the NH (SH) is associated with a net southward (northward) cross-equatorial MSE transport by the Hadley circulation. Here we examine the cross-equatorial MSE transport across the SASM sector to evaluate to what extent similar characteristics are found in the SASM overturning circulation.

Fig. 3.7 shows the vertically integrated meridional fluxes in MSE, averaged 5°S – 5°N , as a function of longitude and day. During the summer monsoon season, there is a clear split in the MSE fluxes around 60°E : west of 60°E , MSE transport is positive and dominated by the lower-level moist enthalpy components, while east of 60°E , MSE transport is negative and dominated by the upper-level geopotential component. This is consistent with the findings of Heaviside and Czaja (2013), who identified two distinct categories of circulation associated with the Asian summer monsoon: a strong Somali jet off the eastern coast of Africa, with transport mostly occurring in the lower troposphere (surface up to approximately 600 hPa); and a deep meridional overturning circulation in the longitudes of monsoonal convection, with a vertical dipole structure in mass and energy transports. Fig. 3.7 confirms that 60°E is an appropriate western boundary to use in defining our SASM sector such that the sector-mean fields are representative of the SASM meridional overturning circulation.

Fig. 3.8 shows the seasonal evolution in cross-equatorial MSE fluxes, integrated across the Somali jet sector (40 – 60°E) and SASM sector (60 – 100°E). We see that in the SASM sector, the MSE transport and sector mean ITCZ display a seasonal evolution consistent with the energy budget framework. Around day -30, as the

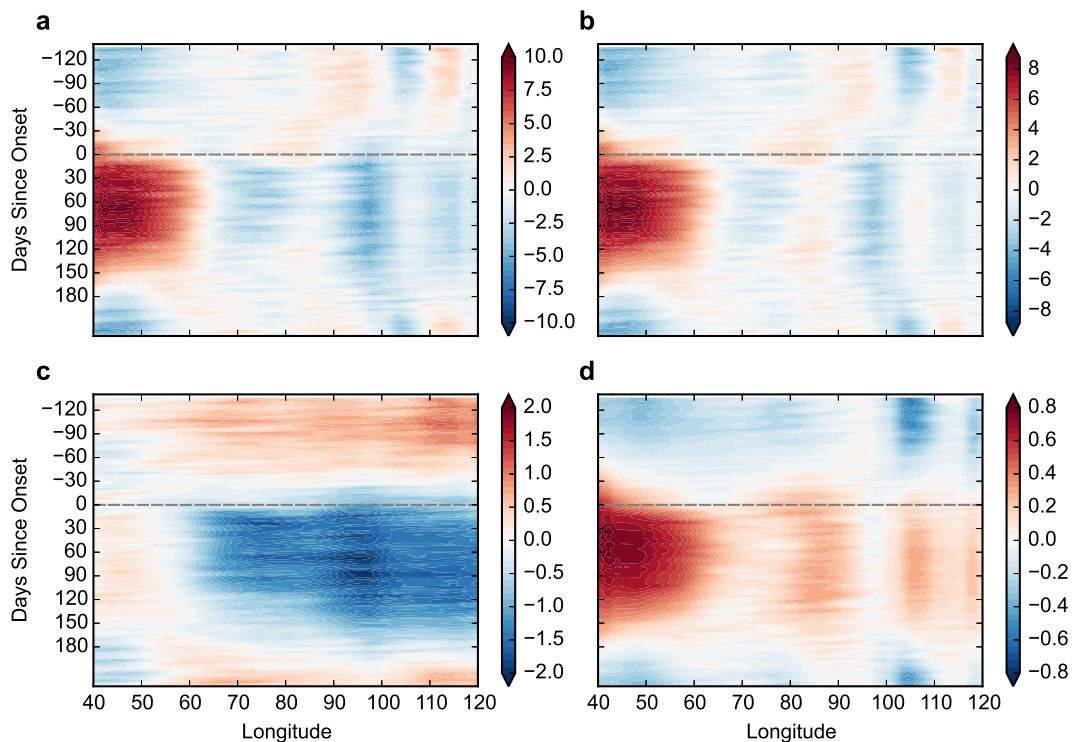


Figure 3.7: Meridional fluxes of MSE components, averaged 5°S – 5°N (10^9 W m^{-1}). (a) Total MSE flux $v(C_p T + gz + L_v q_v)$. (b) Enthalpy flux $vC_p T$. (c) Geopotential flux vgz . (d) Latent energy flux $vL_v q_v$.

SASM ITCZ migrates from the SH to the NH (Fig. 3.4(a)), the cross-equatorial MSE fluxes transition from northward to southward. Between days 0 and 15, as the ITCZ migrates deep into the NH subtropics and the SH Hadley cell abruptly strengthens, there is a concurrent increase in the magnitude of southward cross-equatorial MSE fluxes. In the Somali jet sector, cross-equatorial MSE fluxes become northward around day -30 and start to intensify over the following month, consistent with previous findings that intensification of the Somali jet precedes the onset of monsoon rainfall by several weeks (Boos and Emanuel, 2009). From day 0 to 15, the northward MSE fluxes in the Somali jet sector abruptly strengthen even further, culminating in very strong energy transport during the mature monsoon season.

Most of the MSE transported by the Somali jet across the equator eventually flows eastward into the SASM sector, where it is then returned across the equator in the upper branch of the SASM overturning circulation (Heaviside and Czaja, 2013). It is interesting that despite the significant contribution of these zonal flows to the SASM energy budget, the relationship between SASM sector mean ITCZ position

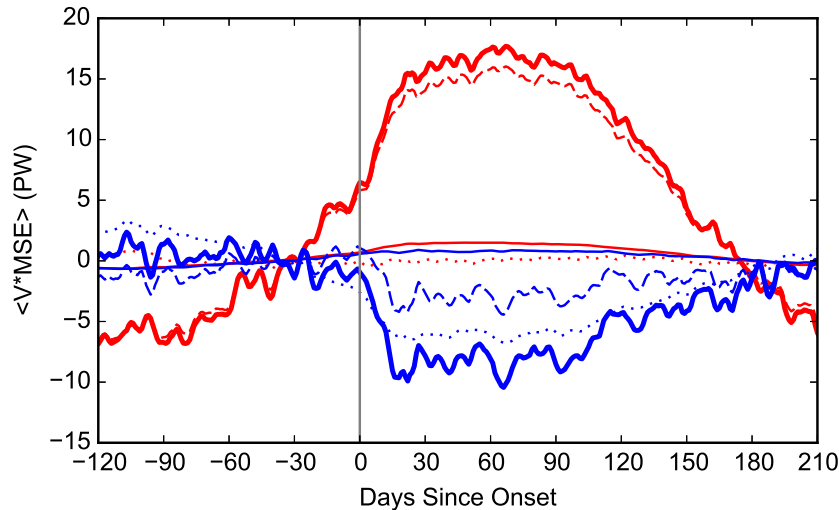


Figure 3.8: Cross-equatorial fluxes of MSE (PW) averaged 5°S – 5°N and integrated across the Somali jet sector (40 – 60°E , red) and SASM sector (60 – 100°E , blue), showing fluxes of total MSE (heavy solid), enthalpy (dashed), geopotential energy (dotted), and latent energy (solid).

and cross-equatorial MSE transport is similar to the energy budget framework for a closed meridional circulation. In future work, we will further explore these relationships and other aspects of the SASM energy budget.

3.4 Momentum budget

Leading order balances in the upper troposphere

To investigate the dominant balances in the zonal momentum budget, we decompose the flow into mean and eddy components as $A = [\bar{A}] + \bar{A}^* + A'$, where overbars denote time mean fields, computed with a 5-day moving average, centered on each day ($\bar{A} = \int_{t_1}^{t_2} A dt / (t_2 - t_1)$); primes denote deviations from these time means; square brackets denote the SASM sector mean ($[A] = \int_{x_1}^{x_2} A dx / (x_2 - x_1)$, with x_1 , x_2 corresponding to 60°E , 100°E); and asterisks denote deviations from the sector mean. Thus, the fields $[\bar{u}]$, $[\bar{v}]$, and $[\bar{\omega}]$ represent the quasi-steady (over 5 days) mean meridional circulation (MMC) within the SASM sector and the fields \bar{u}^* , \bar{v}^* , and $\bar{\omega}^*$ represent quasi-stationary eddies associated with deviations from this sector mean circulation. We define the mean and eddy components using the sector mean rather than the full zonal mean, following the approach of Yang et al. (2013), because we want the MMC to represent the SASM overturning circulation, rather than having the SASM circulation consolidated into the stationary eddy field.

In the upper troposphere, assuming negligible friction, the zonal momentum equation within the SASM sector is given by Eqs. 3.1–3.5:

$$\partial_t \bar{u} = ADV_{MMC} + EMFC_{ST} + EMFC_{TR} + CRS + f[\bar{v}] + f\bar{v}^* - \partial_x \bar{\Phi}^* \quad (3.1)$$

$$ADV_{MMC} = \frac{-[\bar{v}]}{\cos\theta} \partial_y([\bar{u}]\cos\theta) - [\bar{\omega}]\partial_p[\bar{u}] \quad (3.2)$$

$$EMFC_{ST} = -\partial_x(\bar{u}^*\bar{u}^*) - \frac{1}{\cos^2\theta} \partial_y(\bar{u}^*\bar{v}^*\cos^2\theta) - \partial_p(\bar{u}^*\bar{\omega}^*) \quad (3.3)$$

$$EMFC_{TR} = -\partial_x(\bar{u}'\bar{u}') - \frac{1}{\cos^2\theta} \partial_y(\bar{u}'\bar{v}'\cos^2\theta) - \partial_p(\bar{u}'\bar{\omega}') \quad (3.4)$$

$$CRS = -[\bar{u}]\partial_x\bar{u}^* - \frac{[\bar{v}]}{\cos\theta} \partial_y(\bar{u}^*\cos\theta) - [\bar{\omega}]\partial_p\bar{u}^* - \frac{\bar{v}^*}{\cos\theta} \partial_y([\bar{u}]\cos\theta) - \bar{\omega}^* \partial_p[\bar{u}] \quad (3.5)$$

The acceleration of zonal wind is comprised of the following components: advection by the MMC (ADV_{MMC}), eddy momentum flux convergence (EMFC) from stationary eddies ($EMFC_{ST}$) and transient eddies ($EMFC_{TR}$), cross-terms representing interactions between stationary eddies and the MMC (CRS), Coriolis forces, and the pressure gradient force (PGF: $-\partial_x \bar{\Phi}^*$). Note that with our definition of $[A]$, $\partial_x[A] \neq [\partial_x A]$ due to the boundary terms at x_1, x_2 , so although $[A^*]$ is identically zero, $[\partial_x A^*]$ is not. Thus, when taking the SASM sector mean of Eqs. 3.1–3.5, the term $[f\bar{v}^*]$ in Eq. 3.1 drops out, while the boundary term $[\partial_x \bar{\Phi}^*] = \bar{\Phi}^*|_{x_2} - \bar{\Phi}^*|_{x_1}$ does not; the ∂_x term in Eq. 3.3 becomes a boundary term $(\bar{u}^*\bar{u}^*)|_{x_2} - (\bar{u}^*\bar{u}^*)|_{x_1}$, and similarly for Eq. 3.4; and Eq. 3.5 reduces to a single term on the right-hand side: $CRS = -[\bar{u}](\bar{u}^*|_{x_2} - \bar{u}^*|_{x_1})$.

Fig. 3.9 shows the seasonal evolution of the dominant terms in the zonal momentum balance at 200 hPa, along with the zonal wind at this level. In the tropics, the dominant balance is between nonlinear advection by the MMC (ADV_{MMC}), Coriolis force on the MMC ($f[\bar{v}]$), and the pressure gradient term, consistent with previous findings for the Asian monsoon sector (Yang et al., 2013). Adding the meridional component of ADV_{MMC} and the MMC Coriolis term yields a term proportional to the meridional advection of absolute angular momentum by the MMC: $f[\bar{v}] -$

$\frac{1}{\cos\theta}[\bar{v}]\partial_y([\bar{u}]\cos\theta) = \frac{-1}{\cos\theta}[\bar{v}]\partial_y[\bar{m}]$, where m is the absolute angular momentum. Fig. 3.9 shows that advection of absolute angular momentum is very small in the tropics, compared to the extratropics. Thus it is evident that the SASM overturning circulation is highly nonlinear and approaches angular momentum conservation.

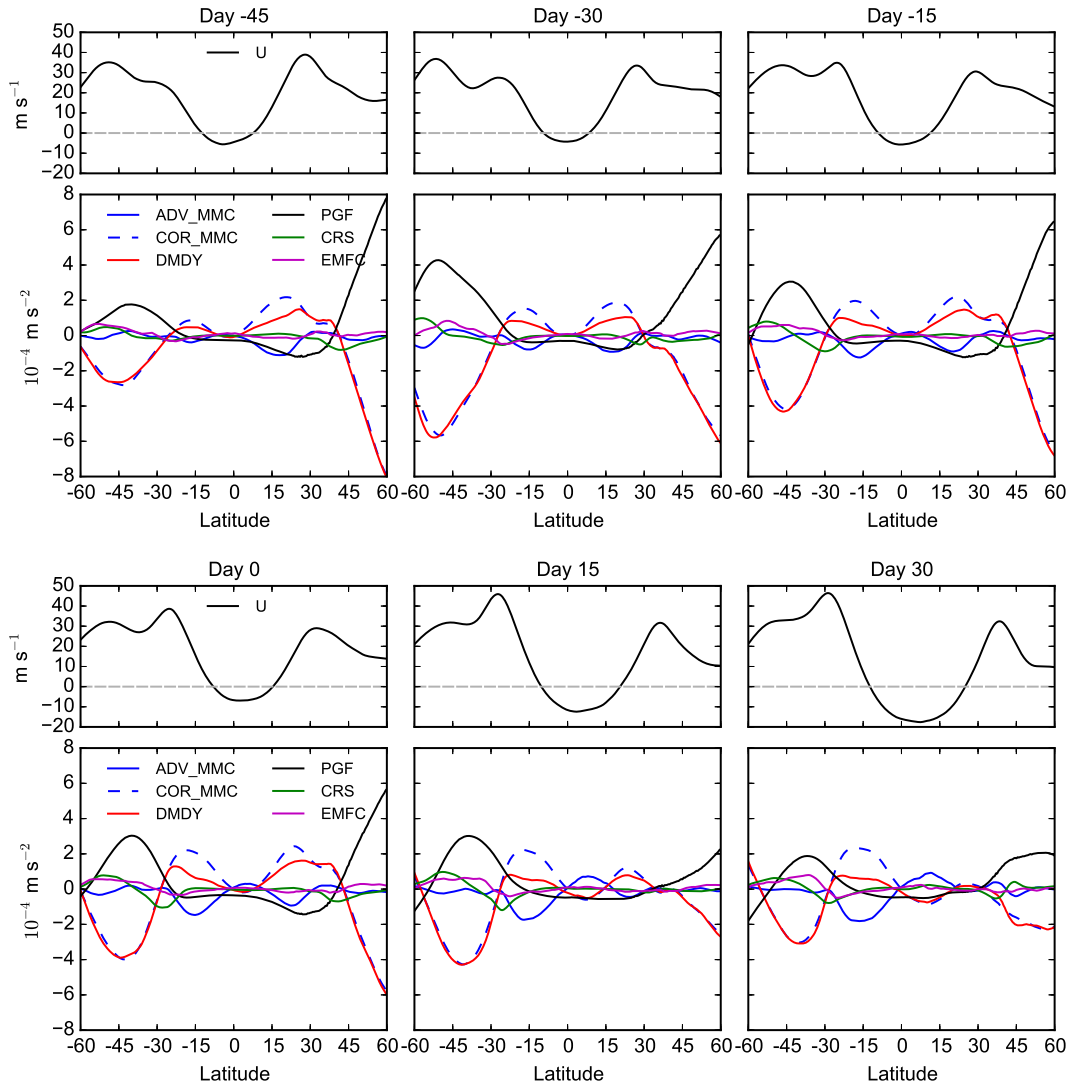


Figure 3.9: Dominant terms in the SASM sector mean zonal momentum balance (10^{-4} m s^{-2}) and zonal wind (m s^{-1}) at 200 hPa. The components of the momentum balance are: advection by MMC (solid blue), Coriolis MMC (dashed blue), pressure gradient force (black), eddy-mean flow cross term (green), and EMFC from transient and stationary eddies (violet). The sum of the MMC advection and Coriolis terms is shown as DMDY (red): $f[\bar{v}] - \frac{1}{\cos\theta}[\bar{v}]\partial_y([\bar{u}]\cos\theta) = \frac{-1}{\cos\theta}[\bar{v}]\partial_y[\bar{m}]$.

The seasonal evolution of upper-level zonal winds and momentum budget displays a coherent set of changes across both northern and southern hemispheres, extending

from the tropics to the extratropics, as the monsoon develops. On day -45, when the ITCZ is in the SH, we see a strong subtropical jet in the NH, centered around 28°N , which is sustained by westerly acceleration from the Coriolis force on the cross-equatorial NH Hadley cell; in the SH, there is a much weaker and broader subtropical jet centered around $25\text{-}30^{\circ}\text{S}$, almost merging with the strong midlatitude jet centered around 50°S , which is sustained by the PGF, EMFC, and eddy-mean flow cross terms. From days -30 to 0, as the SH Hadley cell becomes cross-equatorial and expands into the NH, while the NH cell contracts and weakens, the NH subtropical jet weakens while the SH subtropical jet intensifies and becomes stronger than the midlatitude jet. By day 30, when mature monsoon conditions are well established, the equatorial easterlies have strengthened and broadened across the tropics, consistent with the expansion of the SH cross-equatorial Hadley cell; the NH westerly jet has migrated north to approximately 38°N and, consistent with the near disappearance of the NH Hadley cell, it is no longer characteristic of a subtropical jet, instead being primarily sustained by the PGF; in the SH, the subtropical jet strongly dominates over the midlatitude jet; and the maximum in SH EMFC has migrated from the midlatitude baroclinic zone (where it was for days -45 to -30) to the poleward flank of the subtropical jet, as expected for a strong subtropical jet regime (Lee and Kim, 2003).

Onset mechanisms

In idealized monsoon studies, Bordoni and Schneider (2008) and Schneider and Bordoni (2008) found that at monsoon onset, the tropical circulation transitions from an equinox regime, in which midlatitude eddies dominate the zonal momentum budget, to a solstice regime, in which the cross-equatorial cell more closely approaches conservation of angular momentum and responds more directly to thermal driving. With this framework, they propose two dynamical feedbacks which contribute to the abruptness in monsoon onset, compared to the more gradual seasonal variation in solar radiative fluxes. The first feedback involves interactions between midlatitude eddies and the MMC: as the ascent latitude of the Hadley circulation migrates poleward with the seasonal changes in insolation, the cross-equatorial winter cell expands into the latitudes of upper-level tropical easterlies, where it is shielded from midlatitude eddies, which break at their critical latitudes near the zero line of the zonal wind (Randel and Held, 1991). This reduces the contribution of midlatitude eddies to the zonal momentum budget of the cross-equatorial cell, making it closer to angular momentum conserving, which strengthens the circulation, and strengthens

and broadens the region of tropical easterlies, thereby further shielding the MMC from midlatitude eddies, in a positive feedback. The second positive feedback arises from advection of lower MSE air by the lower branch of the cross-equatorial cell, moving the MSE maximum—and thus the ascending branch of the cell—further poleward, which also strengthens the cell, and strengthens and broadens the tropical easterlies. For these feedbacks to render the onset transition rapid, the underlying surface must have a low enough thermal inertia for the second feedback to operate efficiently and to allow the circulation to adjust rapidly.

Fig. 3.3 shows that the SASM onset transition is consistent with the first dynamical feedback. Prior to onset day, much of the MMC is in a region of upper-level westerlies, with the majority of mass transport (indicated by the maximum in streamfunction) occurring in the latitudes of upper-level westerlies. During the onset stage, the MMC abruptly expands into the region of upper-level easterlies, while the upper-level easterlies strengthen and expand. By day 15, most of the MMC mass transport occurs in latitudes of upper-level easterlies, where it is more shielded from the influence of midlatitude eddies.

To further explore the interactions between eddies and the SASM mean flow, we use the zonal momentum budget (Equations 3.1–3.5) to decompose the streamfunction into mean, eddy and pressure gradient components. Fig. 3.10 shows the mean (MMC) and eddy (transient and stationary EMFC plus eddy-mean flow cross terms) components along with the total streamfunction for days -30, 0, and 30. Since the MMC and eddy components are calculated by dividing the zonal momentum terms by the Coriolis parameter, these components are masked out near the equator where $f \rightarrow 0$. Prior to onset, the mean and eddy components are approximately equal in magnitude. As the monsoon develops from days 0 to 30, the MMC component strengthens and expands deep into the NH subtropics, while the eddy component stays roughly the same and remains in the SH, where it contributes only weakly to the flow, its influence confined to the descending branch of the Hadley cell. This behavior is consistent with idealized simulations of the zonal mean circulation, which show a transition between an equinox regime with eddies strongly contributing to the Hadley circulation, to a solstice regime where eddies have minimal impact on the Hadley cell, which approaches angular momentum conservation (Schneider and Bordoni, 2008).

The SASM onset transition is also consistent with the second dynamical feedback proposed by Bordoni and Schneider (2008) and Schneider and Bordoni (2008) and

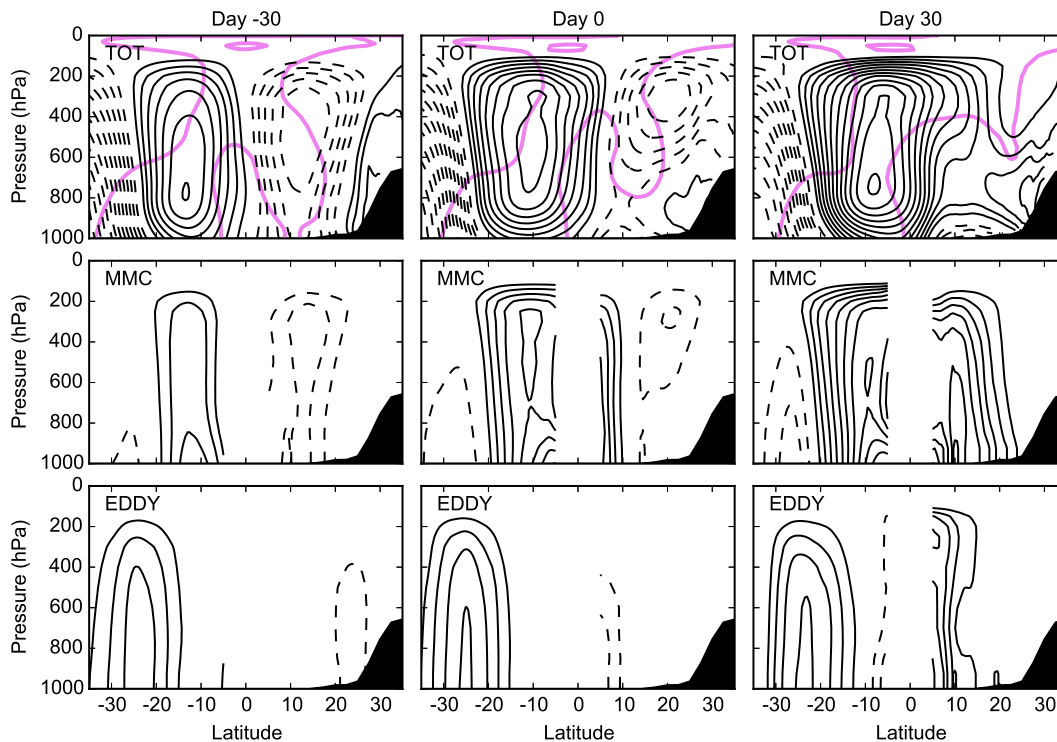


Figure 3.10: Latitude-pressure contours of SASM sector mean streamfunction (black, contour interval $5 \times 10^9 \text{ kg s}^{-1}$) and the zero line of zonal wind (violet) on days -30, 0, and 30, showing the total, mean, and eddy components of the streamfunction.

the role of surface thermal inertia. As a proxy for surface thermal inertia, we consider the surface type (land vs. ocean) and for ocean regions, the mixed layer depth, assuming that shallower mixed layers have lower thermal inertia than deeper mixed layers. Fig. 3.1 shows that during May—the month corresponding to SASM onset in the climatological mean—surface thermal inertia decreases northward in the SASM sector, with shallowest mixed layers in the northern Arabian Sea and Bay of Bengal, consistent with previous studies (Rao et al., 1989), and an increasing fraction of land in the sector northward from approximately 10°N . The latitude of maximum θ_{eb} , which gradually migrates northward in the pre-monsoon stage (Fig. 3.4(e)), reaches 15.5°N at day 0; at this latitude, the Indian subcontinent constitutes a significant fraction of the SASM sector and ocean mixed layers are very shallow ($< 30 \text{ m}$). Thus day 0 marks the expansion of the SASM circulation into latitudes with lower surface thermal inertia; we speculate that this allows the second feedback to operate efficiently and the circulation to adjust rapidly to mature monsoon conditions within just a few weeks.

3.5 Discussion and conclusions

In this work, we have analyzed observed seasonal changes in the dynamics and thermodynamics of the SASM, with the specific goal of evaluating these changes within the framework of emerging theories of monsoons. We find that monsoon onset marks a transition in the SASM large-scale dynamics, from an equinox regime with a pair of tropical overturning cells, to a solstice regime characterized by a strong cross-equatorial SH cell with ascending branch in the NH subtropics and negligible NH summer cell. The leading order momentum budget in the SASM sector after monsoon onset is indicative of highly nonlinear dynamics, with eddies only playing a minor role in the monsoonal cell. Not surprisingly, many features of the monsoonal cross-equatorial cell are qualitatively similar to those predicted by the axisymmetric, angular momentum-conserving theory for tropical circulations with off-equatorial peak heating (Lindzen and Hou, 1988). These features include the relative strengthening and weakening of subtropical jets in each hemisphere as the ITCZ migrates across the equator, the strengthening and broadening of tropical upper-level easterlies as the monsoon develops, and the symmetrization between the NH and SH in upper-level temperatures and zonal winds.

The transition in the leading order momentum budget in the SASM, with the nonlinear terms becoming increasingly important at and after monsoon onset, and the expansion of the SH overturning circulation into latitudes of upper-level easterlies, are similar to transitions in the tropical overturning circulation seen at monsoon onset in idealized zonally-symmetric, aquaplanet studies (Bordoni and Schneider, 2008; Schneider and Bordoni, 2008). This suggests that eddy-mean flow feedbacks identified in those studies may be acting in the SASM sector, and may be involved in and contribute to the abruptness of the SASM onset. At monsoon onset, ocean mixed layer depths are shallow under the ascending branch, allowing for rapid adjustments of the circulation and the ITCZ over the ocean as well as over land.

As the monsoon develops, the maxima in precipitation and upper-level temperatures closely follow the maximum in θ_{eb} , consistent with quasi-equilibrium convective dynamics. At monsoon onset, the rapid migration of the sector mean ITCZ and the likewise rapid broadening and strengthening of the monsoonal overturning cell are accompanied by an abrupt strengthening and northward migration of the maximum in θ_{eb} . Importantly, these changes in θ_{eb} result from changes in near-surface specific humidity, rather than changes in near-surface temperature, with the near-surface meridional temperature gradient actually decreasing at monsoon onset. This is

inconsistent with the traditional sea-breeze paradigm for the monsoon and confirms the convectively coupled view of the SASM circulation as an energetically-direct overturning circulation as more fundamental for the understanding of monsoon dynamics.

The fact that the observed SASM onset appears in the momentum balance as a transition from an eddy-dominated regime to an axisymmetric-like angular momentum-conserving regime suggests that important aspects of its fundamental dynamics, such as driving mechanisms, can be understood without any zonal asymmetries. In fact, the circulation changes that occur at monsoon onset over the SASM sector, and that closely resemble those in the zonal mean circulation, have been reproduced in aquaplanet studies. These results might seem at odds with the analysis of Shaw (2014), who shows how growth of stationary-wave fluxes of momentum and energy dominating over the zonal mean transport is implicated in the observed rapid transition in the NH zonal mean circulation. In her analysis, however, the seasonal development of monsoons and associated oceanic anticyclones is by construction embedded in the stationary fluxes. Here, by performing similar analyses limited to the SASM sector, we are able to show how the zonally-localized dynamics during the monsoon season is dominated by sector mean transport, rather than stationary deviations from the sector mean, suggestive of a nonlinear dynamical regime. The nonlinear response to the insolation forcing in the SASM sector can drive rapid circulation changes without an explicit role for stationary eddies and can project strongly on likewise rapid changes in the zonal mean circulation.

This is of course not to say that zonal asymmetries do not play any role in monsoonal circulations, which are associated with strong zonal asymmetries both in the forcing and resulting flows. An outstanding question that deserves further study is to what extent zonally-symmetric theories can provide insight into the response of zonally-asymmetric monsoons to radiative perturbations, such as those associated with increased greenhouse gas concentration. One robust response to warming is, for instance, increased land-sea thermal contrast (Byrne and O’Gorman, 2013). Recent modeling and observational work, including this one, indicates that this does not imply *per se* increased monsoonal circulation strength, and that other factors, including local and remote forcing need to be considered in evaluating this response. While pertaining to the seasonal evolution of the SASM, the results presented in this paper do suggest that zonally symmetric theories might provide a useful starting point for such studies.

Chapter 4

INTERANNUAL VARIABILITY

Walker, J. M., S. Bordoni, and T. Schneider (2015). “Interannual Variability in the Large-Scale Dynamics of the South Asian Summer Monsoon”. In: *J. Clim.* 28.9, pp. 3731–3750. DOI: 10.1175/JCLI-D-14-00612.1.

Abstract

This study identifies coherent and robust large-scale atmospheric patterns of interannual variability of the South Asian summer monsoon (SASM) in observational data. A decomposition of the water vapor budget into dynamic and thermodynamic components shows that interannual variability of SASM net precipitation ($P - E$) is primarily caused by variations in winds rather than in moisture. Using linear regression analyses, we find that strong monsoons are distinguished from weak monsoons by a northward expansion of the cross-equatorial monsoonal circulation, with increased precipitation in the ascending branch. Interestingly, and in disagreement with the view of monsoons as large-scale sea-breeze circulations, strong monsoons are associated with a decreased meridional gradient in the near-surface atmospheric temperature in the SASM region. Teleconnections exist from the SASM region to the southern hemisphere, whose midlatitude poleward eddy energy flux correlates with monsoon strength. Possible implications of these teleconnection patterns for understanding SASM interannual variability are discussed.

4.1 Introduction

The South Asian summer monsoon (SASM) displays variability on timescales from intraseasonal, through interannual, to decadal and beyond (e.g., Webster et al., 1998; Gadgil, 2003; Turner and Annamalai, 2012; Schneider et al., 2014). The standard deviation of interannual variability of SASM rainfall amounts to approximately 10% of the long-term mean summer rainfall (Gadgil, 2003). This year-to-year variability of the SASM is sufficient to trigger drought and flood conditions, with major agricultural, economic, and social impacts (e.g., Gadgil and Kumar, 2006).

Despite having been studied for many decades, the interannual variability of the SASM remains poorly understood and predicted. Many factors that influence variations of the SASM precipitation on interannual timescales have been investigated.

Some studies have focused on the influence of sea surface temperatures (SSTs), particularly El Niño and the Southern Oscillation (ENSO; e.g., Pant and Parthasarathy, 1981; Rasmusson and Carpenter, 1982; Meehl, 1987; Webster and Yang, 1992) and the east-west Indian Ocean Dipole (IOD; e.g., Cherchi and Navarra, 2012). Others have focused on land processes such as snow cover on the Tibetan plateau and in Eurasia (e.g., Blanford, 1884; Hahn and Shukla, 1976; Meehl, 1994; Shuen et al., 1998; Wu and Kirtman, 2003). Of these factors, the strongest association has been found with ENSO. However, ENSO variations account for less than half of the total variation in SASM precipitation (Webster et al., 1998), and the relationship appears to have weakened in recent decades (Kumar et al., 1999; Kumar et al., 2006).

In this study, we investigate the interannual variability of the SASM using observational data. Although there is considerable regional variability within the SASM domain, we first address the year-to-year variations of the large-scale monsoonal circulation, rather than local or regional features, and we primarily focus on large-scale atmospheric budgets such as the moisture, energy, and momentum budgets. Our approach is motivated by recent advances in the fundamental theoretical understanding of large-scale monsoonal circulations, such as the SASM.

Traditionally, the SASM has been viewed as a large-scale sea-breeze circulation, driven by surface temperature contrasts and their associated atmospheric pressure gradients between the Asian continent to the north and the Indian ocean to the south (e.g., Webster and Fasullo, 2003). The sea-breeze paradigm has been extended to include the effects of elevated diabatic heating from moist convection (e.g., Webster et al., 1998) and the Tibetan plateau (e.g., Li and Yanai, 1996), consistent with recent observational studies that have shown that interannual variability of the SASM circulation is more strongly correlated with upper-tropospheric thermal contrasts than lower-tropospheric thermal contrasts (Dai et al., 2013; Sun et al., 2010). Whether the emphasis is on surface thermal contrasts or upper-tropospheric thermal contrasts, however, these studies take the surface inhomogeneities between land and ocean as an essential mechanism driving the SASM circulation; they view the meridional temperature gradient as a driver of monsoon circulations that can, to some extent, be considered as controlled by factors external to the monsoon circulations.

In recent years, an alternative theoretical framework has emerged, which views the SASM as the regional manifestation of the seasonal migration of the intertropical convergence zone (ITCZ) (e.g., Chao, 2000; Chao and Chen, 2001; Gadgil, 2003).

The monsoonal convergence is the root of the ascending branch of a thermally-direct monsoonal overturning circulation, which shapes meridional temperature gradients and approaches conservation of angular momentum in its upper branch (e.g., Privé and Plumb, 2007; Schneider and Bordoni, 2008; Bordoni and Schneider, 2008). In support of this view, modeling studies have shown that monsoonal circulations can exist even on aquaplanets without any land-ocean thermal contrasts (Privé and Plumb, 2007; Bordoni and Schneider, 2008), provided that the lower boundary has a small enough thermal inertia to allow for the ITCZ to migrate poleward into the subtropics. In this framework, the meridional temperature gradient (e.g., Li and Yanai, 1996) and convective heating (e.g., Gill, 1980) are viewed as being primarily controlled by the monsoon circulation, forming the atmosphere's response to the seasonal variation of insolation. Consistent with quasi-equilibrium (QE) theories of moist convection (e.g., Emanuel et al., 1994), latent heat release is posited to relax the atmosphere to a convectively neutral stratification, rather than to act as a driver for the monsoonal circulation (e.g., Privé and Plumb, 2007). Observational studies have confirmed that the free-tropospheric temperature in the ascending branch of the SASM circulation is coupled to the sub-cloud equivalent potential temperature, a finding consistent with the assumption of convective quasi-equilibrium (Nie et al., 2010; Hurley and Boos, 2013).

To the extent that monsoonal circulations form an essential part of the seasonal Hadley circulation, analyses of large-scale budgets zonally averaged over wide longitude sectors can prove useful in investigating how SASM interannual variability arises. For instance, Schneider and Bordoni (2008) and Bordoni and Schneider (2008) suggest that the onset of the SASM might be interpreted as a shift of the dominant balance in the upper-tropospheric zonal momentum budget, from a budget dominated by eddy momentum fluxes to one dominated by momentum transport by the cross-equatorial Hadley cell. Other studies have analyzed how extratropical thermal forcings, such as changes in glaciation or in the strength of the Atlantic meridional overturning circulation, can influence the location of the zonally and annually averaged ITCZ, through shifts toward a differentially warming hemisphere (e.g., Chiang and Bitz, 2005; Kang et al., 2008; Chiang and Friedman, 2012; Bischoff and Schneider, 2014). These studies have emphasized the role of the cross-equatorial energy transport and the atmospheric energy budget in controlling the position of the tropical precipitation, through mechanisms that might also be relevant to the SASM (Schneider et al., 2014)

Here we investigate SASM interannual variability observationally, beginning by developing a new index for the SASM strength that links monsoon precipitation to the large-scale circulation more directly than existing indices. We examine correlations between the SASM strength and large-scale dynamics both within the monsoon region and globally, to explore possible local and non-local influences on the monsoon. Using reanalysis and precipitation data, we seek to answer the following questions:

1. Is the interannual variability in SASM precipitation dominated by changes in the circulation or by changes in atmospheric moisture?
2. What large-scale dynamic and thermodynamic patterns are associated with strong and weak monsoon years?
3. Are there connections between extratropical eddy activity and SASM interannual variability?

To address question (1), we decompose the atmospheric moisture budget of the SASM into dynamic and thermodynamic components, and we use linear regression analyses to address questions (2) and (3). Section 2 describes the data sources and methods used in our analysis. In Section 3, we examine the atmospheric moisture budget of the SASM and introduce the new monsoon index. In Section 4, we evaluate dynamic and thermodynamic patterns associated with strong and weak monsoon years. In Section 5, we explore teleconnections between the SASM and the extratropics, especially in the southern hemisphere. In Section 6, we discuss the possible influence of ENSO and IOD on the results presented in Sections 4 and 5. We summarize our findings and provide concluding remarks in Section 7.

4.2 Data and methods

Winds, atmospheric temperature, and specific humidity for the years 1979 – 2011 are used from the 6-hourly data of the European Centre for Medium-Range Weather Forecasts (ECMWF) ERA-Interim Reanalysis (Dee et al., 2011), on 60 vertical levels on terrain-following coordinates up to 0.1 hPa and with T255 horizontal resolution (grid resolution approximately $0.7^\circ \times 0.7^\circ$). Precipitation data are from the Global Precipitation Climatology Project (GPCP; Adler et al., 2003) Version 2.2, a set of gridded monthly precipitation estimates based on satellite and rain gauge data, at $2.5^\circ \times 2.5^\circ$ horizontal resolution. To determine which findings

are robust across datasets, we compare our results with the following additional reanalysis products: National Center for Environmental Prediction/National Center for Atmospheric Research (NCEP/NCAR) Reanalysis (NCEP1; Kalnay et al., 1996), National Center for Environmental Prediction/Department of Energy (NCEP/DOE) Reanalysis 2 (NCEP2; Kanamitsu et al., 2002), ECMWF ERA-40 Reanalysis (ERA40; Uppala et al., 2005), and the Twentieth Century Reanalysis Project Version 2 from the National Oceanic and Atmospheric Administration (NOAA) and the University of Colorado Cooperative Institute for Research in Environmental Sciences (CIRES) at the University of Colorado (20CENTURY; Compo et al., 2011). The findings presented here are robust across all of these reanalysis products except where otherwise noted.

To examine the interannual variations of the SASM, we focus on the warm season months from June to September (JJAS), and we introduce a novel yearly monsoon index based on the large-scale moisture budget. The methodology used to develop this monsoon index is described in detail in Section 3; in essence, our index is based on ERA-Interim JJAS averaged moisture flux convergence over a region representative of the large-scale SASM circulation (60-100°E, 10-30°N). This region is similar to SASM regions used in previous studies (Goswami et al., 1999; Wang and Fan, 1999; Hurley and Boos, 2013); it was chosen to include the climatological precipitation maxima over India and the Bay of Bengal. The results shown here are robust to different choices of averaging regions, as long as the averaging region does not extend in longitude too far east into Southeast Asia, where the interannual precipitation variability is anti-correlated with that of the Indian monsoon, as will be discussed in Section 4.

Large-scale dynamics and precipitation patterns associated with strong and weak South Asian summer monsoons are investigated by performing linear regression analyses using the monsoon strength index, normalized by its standard deviation, and the atmospheric and precipitation fields from ERA-Interim and GPCP, respectively. For each data field considered (e.g., wind, temperature, precipitation), the linear regression is calculated at each data point by regressing the 1979-2011 timeseries of yearly JJAS averaged values of the data field at that point, against the monsoon index. Focus is on the interannual variability; the long-term linear trend from 1979-2011 is removed from the monsoon index and from the data fields in the regression analysis. However, in Appendix A we provide a brief discussion of trends inferred from the ERA-Interim and other reanalysis products, and compare those with trends recently

highlighted in the literature (e.g., Bollasina et al., 2011; Zuo et al., 2013).

Statistical significance of the correlation coefficient at each point is computed by a Student's t-test, and correlations that are statistically significant at the 5% level are highlighted. Composite analysis of the five strongest and five weakest monsoon years shows similar results to the linear regression analysis.

Given that interannual variability in SSTs of surrounding ocean basins has been shown to influence the SASM interannual variability in many previous studies, we also explore if and to what extent patterns exposed here are associated with ENSO and IOD variability.

As an ENSO index, we use the June-August (JJA) average Niño 3.4 index (Trenberth, 1997a) from NOAA. Anomalous ENSO signals tend to be maximal during the boreal winter months December-February (DJF); the JJA average value of Niño 3.4 is strongly correlated with its average value in the following DJF, and thus the JJA Niño 3.4 represents El Niño/La Niña conditions that are developing during the summer monsoon season and the following winter.

The IOD is a measure of the SST gradient between the western equatorial Indian Ocean and the south-eastern equatorial Indian Ocean (Saji et al., 1999). As an index for the IOD, we use the JJA average Dipole Mode Index (DMI) derived from the Hadley Centre Sea Ice and Sea Surface Temperature data set (HadISST), provided by the Japan Agency for Marine-Earth Science and Technology (http://www.jamstec.go.jp/frsgc/research/d1/iod/e/iod/dipole_mode_index.html).

Transient eddy fields are computed for each month of each year by subtracting the monthly mean field from that year and by taking an average, weighted by the number of days per month, of the monthly eddy fields for the seasonal average. Horizontal eddy momentum flux divergence is computed as $\nabla \cdot (\overline{u'u'} \cos \phi)$, where $\mathbf{u} = (u, v)$ is the horizontal velocity field, ϕ latitude, and primes denote transient eddy fields.

4.3 Atmospheric moisture budget

Dynamic and thermodynamic components of interannual variability

In a long-term mean, when changes in atmospheric moisture content can be neglected, the vertically integrated moisture budget relates the net precipitation ($P - E$) to the convergence of the water vapor flux, that is

$$\overline{P} - \overline{E} = \text{MFC} = - \int_0^{p_s} \nabla_p \cdot (\overline{\mathbf{u}q}) \frac{dp}{g} \quad (4.1)$$

where MFC is the vertically integrated horizontal moisture flux convergence, $\nabla_p \cdot ()$ the horizontal divergence in pressure coordinates, $\mathbf{u} = (u, v)$ the horizontal wind vector, q the specific humidity, P the precipitation rate, and E the evaporation rate (Peixoto and Oort, 1992). Overbars denote the time mean, in our case over a season.

We study the large-scale SASM moisture budget by averaging the vertically integrated horizontal moisture flux convergence from Eq. (4.1) over the region 60-100°E, 10-30°N, shown in Fig. 4.3, using the ERA-Interim winds and specific humidity averaged over JJAS of each year. This formulation allows us to decompose the monsoon net precipitation into dynamic and thermodynamic components, similar to decompositions performed in previous studies for the zonally averaged circulation (e.g., Held and Soden, 2006), for the response of monsoons to orbital precession (Clement et al., 2004; Merlis et al., 2013), and for the response of monsoons to anthropogenic forcings (Hsu et al., 2013). Specifically, we decompose the yearly JJAS horizontal moisture fluxes $\mathbf{u}q$ according to Eq. (4.2),

$$\delta(\mathbf{u}q) = \bar{\mathbf{u}}\delta q + \bar{q}\delta\mathbf{u} + \delta\mathbf{u}\delta q \quad (4.2)$$

where δ represents the year-to-year deviation from the climatological mean. In Eq. (4.2), the first term on the right hand side represents the thermodynamic component, in which the winds are fixed at their climatological value, and the atmospheric moisture varies from year to year; the second term represents the dynamic component, in which the atmospheric moisture is fixed at its climatological value, and the winds vary from year to year; and the third term is the quadratic term, which we found to be negligible in the SASM moisture budget.

Fig. 4.1 shows that the interannual variability in SASM net precipitation in ERA-Interim is dominated by the dynamic component, which accounts for 92% of the interannual variability, while the thermodynamic component accounts for only 8%. Decomposition of the dynamic term into zonal and meridional components shows that both components contribute significantly to the total variability; the zonal component dominates slightly, with correlation coefficients of 0.62 and 0.38 between the dynamic term of MFC and its zonal and meridional components, respectively. The dominance of the dynamic term is robust across all reanalysis datasets, with the year-to-year variations in SASM net precipitation strongly dominated by variations in the monsoon winds and circulation, rather than variations in atmospheric moisture. This emphasizes the importance of understanding interannual patterns in the

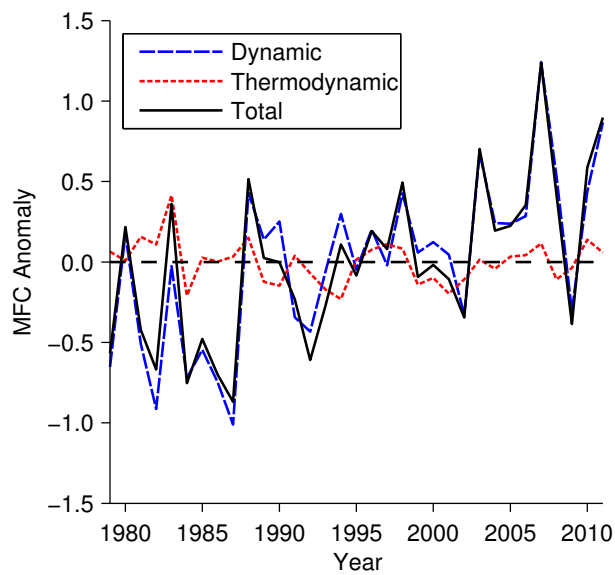


Figure 4.1: Interannual variability of the SASM strength, based on the ERA-Interim atmospheric moisture budget, showing the dynamic component, thermodynamic component, and total variability (mm day^{-1}).

SASM large-scale circulation to understand the interannual variability of the SASM precipitation.

Large-scale monsoon index

The choice of an index to characterize the interannual variability of the SASM has been studied extensively in recent decades. There is no consensus on a single index as the best measure of SASM strength, and many different approaches have been used.

The All India Rainfall (AIR) index is an area-weighted average of rainfall measured at rain-gauge stations distributed over India (Parthasarathy et al., 1992; Parthasarathy et al., 1995). It has been used by the Indian Meteorological Department in many studies of SASM interannual variability and prediction (e.g., Shukla and Mooley, 1987; Yasunari, 1991; Meehl, 1987). While a particularly relevant monsoon index from a socio-economic perspective, the AIR may not fully represent the large-scale monsoonal circulation, since it is limited to the Indian subcontinent and does not include neighboring land and ocean areas with significant monsoon precipitation (cf. Goswami et al., 1999).

Webster and Yang (1992) introduced a dynamically based monsoon index, in which

the large-scale monsoonal circulation is interpreted as a Rossby-wave response to mid-tropospheric latent heat released by monsoon convection over South Asia. The dynamic response is dominated by the lowest baroclinic mode and exhibits vertical wind shear related to the strength of the heat source, and thus to the monsoon precipitation (Webster, 1972; Gill, 1980). Webster and Yang (1992) defined their monsoon index (hereafter WYI) as the zonal wind shear between 850 and 200 hPa, $U_{850}-U_{200}$, averaged over the region $40-110^{\circ}\text{E}$, $0-20^{\circ}\text{N}$. Through thermal wind balance, WYI is linked to the zonal wind shear to the meridional temperature gradient and hence to the land-sea thermal contrast. This index, by construction, captures well the SASM in terms of the zonal wind shear; it also captures the strength of the low-level westerly jet and upper-level easterly jet in the NCEP/NCAR reanalysis (Wang and Fan, 1999).

However, the weak correlation between the WYI and the AIR (Webster and Yang, 1992), as well as significant influences of Western Pacific convective activity on the WYI (Ailikun and Yasunari, 1998; Wang and Fan, 1999), have motivated the introduction of other dynamically based indices to represent the SASM. Other wind shear-based indices include the westerly shear averaged over a different region (Wang and Fan, 1999), and the shear in meridional velocity (Goswami et al., 1999); these indices have been shown to correlate well with each other and with the WYI and AIR.

In the previous section, we showed that the vertically integrated moisture flux convergence averaged over the region $60-100^{\circ}\text{E}$, $10-30^{\circ}\text{N}$, an index which we shall denote as MFC, is by construction related to the SASM net precipitation. Fig. 4.2 shows MFC along with ERA-Interim and GPCP precipitation averaged over the same geographic region, and along with the AIR index from the Indian Institute of Tropical Meteorology. MFC is highly correlated with these other measures of SASM precipitation, with correlation coefficients of 0.87, 0.75 and 0.80 between the detrended MFC and the detrended ERA-Interim precipitation, GPCP precipitation, and AIR, respectively. The correlation between the detrended MFC and WYI is weak (0.22) and not statistically significant at the 5% level, consistent with the weak correlation between WYI and AIR (Webster and Yang, 1992).

Since the interannual variability in MFC is dominated by the dynamic component, MFC is a measure of both net precipitation intensity and of the strength of the large-scale SASM circulation. Therefore, we select MFC as an index for the SASM strength because it accounts for most of the interannual variability in both the

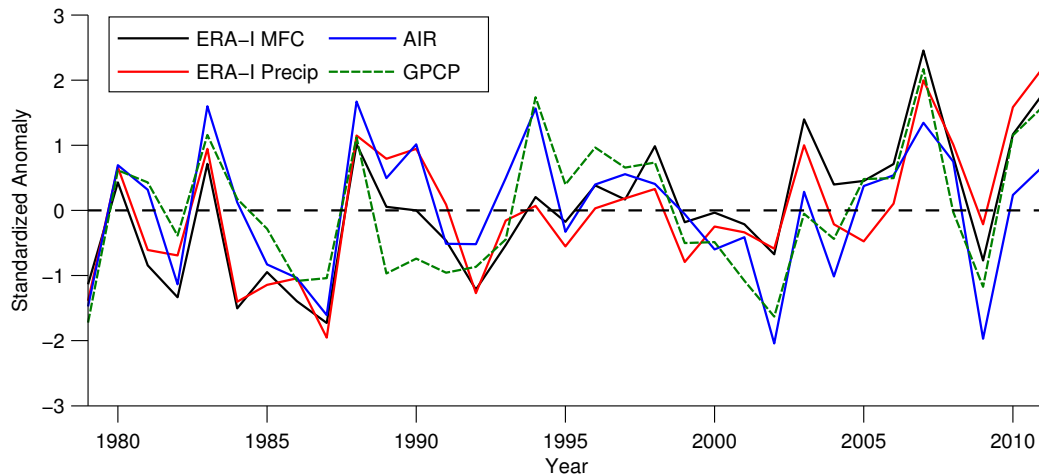


Figure 4.2: Timeseries of the MFC index, based on ERA-Interim atmospheric moisture budget, along with precipitation from ERA-Interim and GPCP averaged over the same region ($60\text{-}100^{\circ}\text{E}$, $10\text{-}30^{\circ}\text{N}$), and the AIR index. Each timeseries is based on JJAS averages, and is shown as the standardized anomaly from the climatological mean.

precipitation and circulation of the SASM. Additionally, it is more robust than precipitation data alone because the moisture flux convergence is controlled by large-scale processes which are better constrained by data. Unlike other dynamical indices which are based on wind shear, under the assumption that temperature gradients are driving the monsoon circulation, MFC is a dynamical index that does not require any such assumptions about the driving mechanisms of the SASM.

On top of the strong interannual variability, the MFC index in Fig. 4.2 shows a slight increasing trend. This is in disagreement with trends in Indian precipitation highlighted by other studies (e.g., Ramanathan et al., 2005; Bollasina et al., 2011) and, as discussed in Appendix A, is not robust across all datasets.

4.4 Large-scale patterns of monsoon variability

Precipitation and meridional overturning circulation

The MFC index of SASM interannual variability allows us to investigate large-scale dynamic and thermodynamic patterns associated with strong (weak) monsoon years. Fig. 4.3 shows the climatology of GPCP precipitation over the SASM domain (a) and the local regression coefficients of the precipitation field onto the MFC index (b). A similar analysis using ERA-Interim data shows that the contribution of evaporation is negligible (not shown), so that the variability in total precipitation associated with strong (weak) monsoons is approximately equal to the variability in net precipitation.

Over India and much of South Asia, there is a strong positive correlation between the measured precipitation and the MFC index. Over the eastern Bay of Bengal, which is a center of maximum SASM precipitation in the climatological mean, the interannual variability of precipitation is negatively correlated with the MFC index; precipitation over this region is lower during a strong SASM. This zonal asymmetry is robust across multiple precipitation datasets and different monsoon indices (not shown), and is consistent with Wang et al. (2001), who show that the two precipitation maxima over India and over the eastern Bay of Bengal have distinct interannual variations.

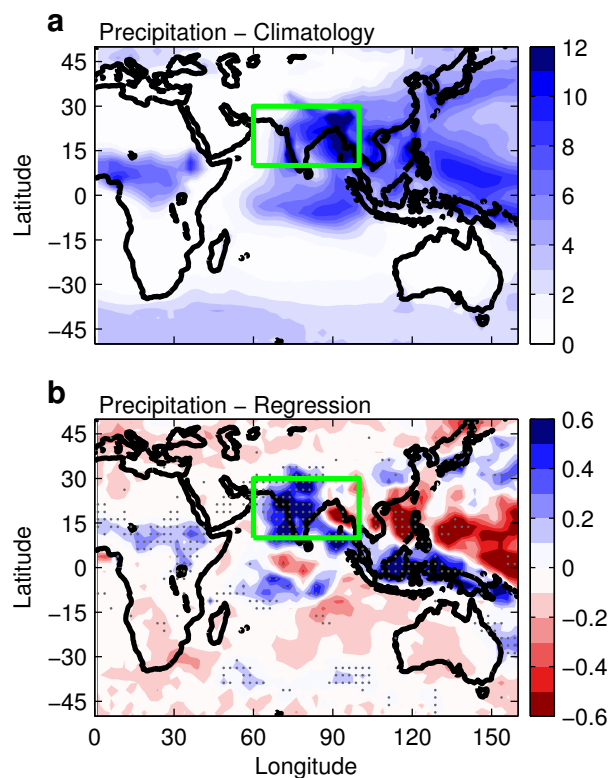


Figure 4.3: JJAS precipitation (mm day^{-1}) from GPCP, showing (a) 1979-2011 climatology, and (b) regression coefficients from linear regression of JJAS precipitation for each year against the standardized MFC index. Gray stippling shows regions where the regression coefficient is significant at the 5% level. The green rectangle shows the averaging region for the monsoon strength index.

East of the SASM region, over the tropical Pacific Ocean, the regression analysis shows a strong negative correlation between precipitation and SASM strength north of the equator, and a strong positive correlation south of the equator (Fig. 4.3), indicating a southward shift of the ITCZ over the western tropical Pacific. While

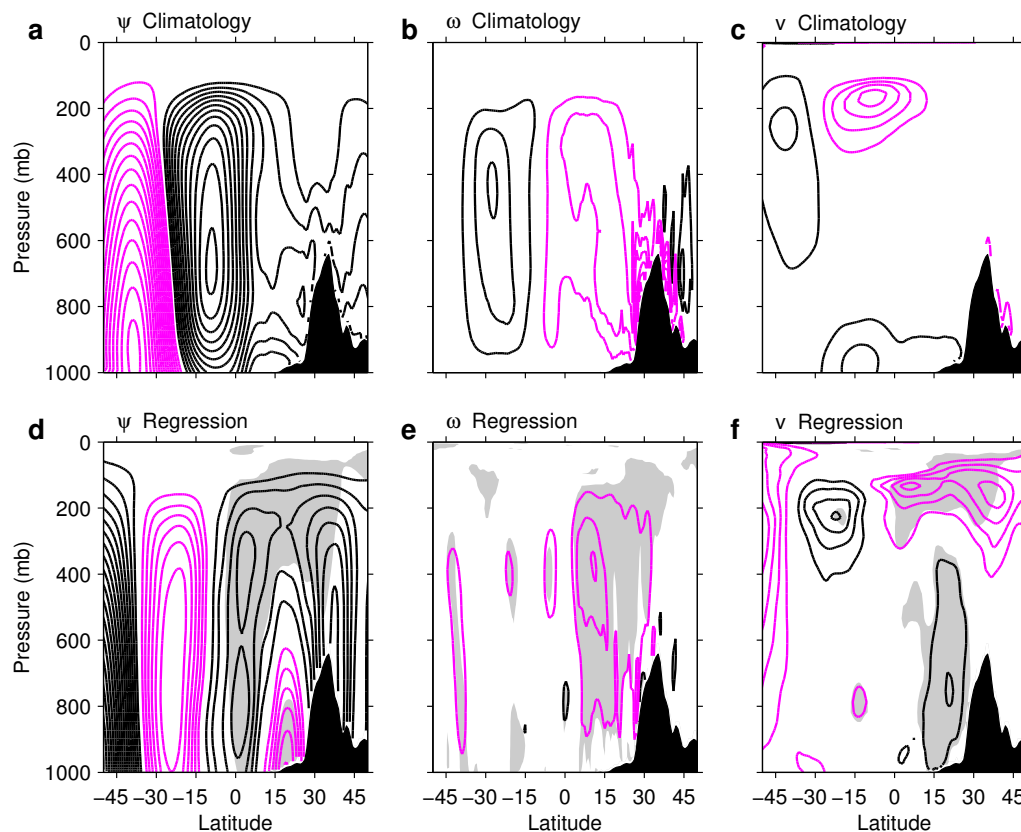


Figure 4.4: Climatology (a-c) and regression coefficients onto MFC index (d-f) of JJAS ERA-Interim SASM sector mean streamfunction, vertical pressure velocity, and meridional velocity. Black contours are positive while violet contours are negative; zero contours are omitted. Gray shading in d-f shows regions where the regression coefficient is significant at the 5% level. Black shading shows the sector mean topography. Contour intervals are: (a) $5 \times 10^9 \text{ kg s}^{-1}$, (b) 0.02 Pa s^{-1} , (c) 2 m s^{-1} , (d) $0.5 \times 10^9 \text{ kg s}^{-1}$, (e) 0.002 Pa s^{-1} , (f) 0.1 m s^{-1} .

evident in ERA-Interim and partly explained by ENSO variability, this feature does not appear to be robust across all reanalysis datasets.

Fig. 4.4a-c shows the ERA-Interim JJAS climatology of the SASM meridional overturning circulation, as measured by the $60\text{-}100^\circ\text{E}$ sector mean (hereafter denoted as the SASM sector) Eulerian mass streamfunction (Fig. 4.4a), vertical pressure velocity (Fig. 4.4b), and meridional velocity (Fig. 4.4c). The climatological fields of meridional and vertical pressure velocity show northward flow from the southern hemisphere to the northern hemisphere in the lower troposphere, ascent in the northern hemisphere tropics and subtropics, southward cross-equatorial flow in the upper troposphere, and subsidence in the southern hemisphere tropics and subtrop-

ics. Together these winds form a thermally direct circulation that has the character of a broad, cross-equatorial Hadley cell, consistent with previous descriptions of the SASM (e.g., Trenberth et al., 2005; Webster et al., 1998). This circulation is illustrated in the climatological Eulerian mass streamfunction in Fig. 4.4a, with maximum streamfunction, and hence maximum meridional mass transport, near the equator. Within the SASM sector, the dominant mass balance is between the meridional and vertical fluxes, as expected, with zonal fluxes into or out of the sector contributing less than 30% of the mass budget. The maximum SASM precipitation is located in the latitudes of the ascending branch of this circulation (Figs. 4.3, 4.6), where the ascending motion maximizes.

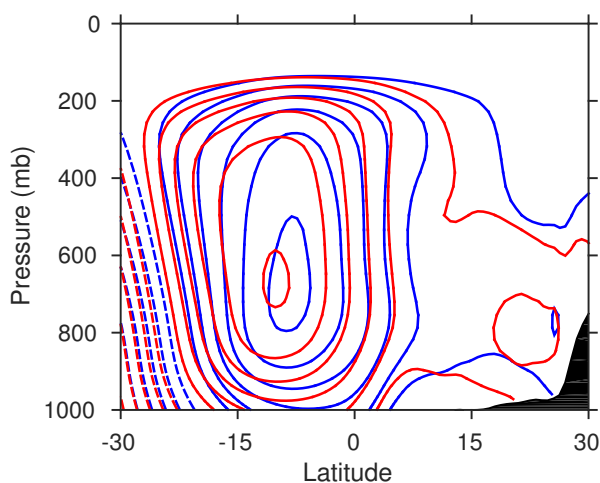


Figure 4.5: Streamfunctions representing “Strong” (blue) and “Weak” (red) monsoonal circulations, defined as those associated with a ± 2 standard deviation excursion of the MFC index. Positive contours are solid, negative contours are dashed, and zero contours are omitted. Contour interval is $5 \times 10^9 \text{ kg s}^{-1}$.

Linear regression of the streamfunction, vertical pressure velocity and meridional velocity onto the monsoon index (Fig. 4.4d-f) shows that strong monsoons are associated with a change in the structure of the meridional circulation, with increased ascent farther north and a correspondingly northward extended circulation. To further highlight differences in the SASM overturning circulation between strong and weak monsoon years, in Fig. 4.5, we show “Strong” (“Weak”) streamfunctions defined as the climatological streamfunction plus (minus) the regression coefficient times 2 standard deviations of MFC. The northward expansion of the strong monsoon circulation compared to the weak monsoon is evident, with a statistically significant positive correlation coefficient of 0.46 between the latitude of maximum streamfunction and the MFC index; this corresponds to a northward shift of approximately

1.38° in the latitude of maximum streamfunction per standard deviation of the MFC index (i.e., a 5.5° shift between the ± 2 standard deviations for strong/weak monsoons in Fig. 4.5). Similarly, there is a statistically significant increase in streamfunction values in the ascending branch of the circulation (Fig. 4.4d).

Using GPCP precipitation data to define “Strong” (“Weak”) precipitation profiles as defined for the streamfunction, we see in Fig. 4.6 that in the SASM sector, strong monsoons are associated with a strengthening of the precipitation and a northward shift of approximately 5° in the latitude of maximum precipitation. Note that this result is not robust across all datasets, so it remains uncertain whether strong monsoons are indeed associated with a northward shift of the local ITCZ within the SASM sector. However, the northward shift in the meridional overturning circulation is robust.

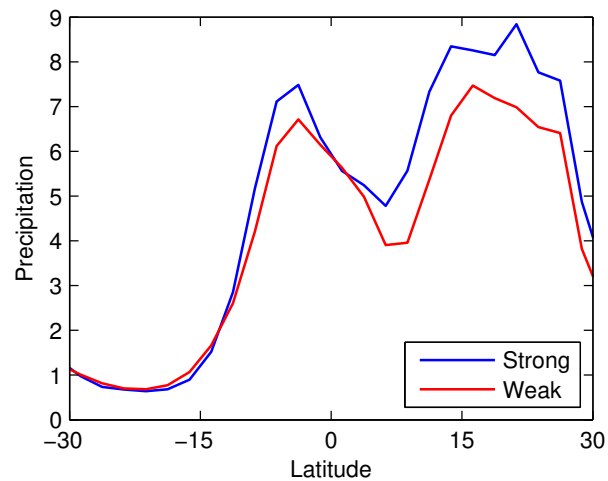


Figure 4.6: SASM sector GPCP JJAS precipitation profiles (mm day^{-1}) for “Strong” (blue) and “Weak” (red) monsoons.

Zonal winds

Fig. 4.7 shows the climatology of ERA-Interim zonal winds at 850 hPa and 200 hPa, while Fig. 4.8 shows the SASM sector mean zonal winds. The main features of the monsoonal circulation are evident in the climatology, with an upper-level easterly jet in the tropics, a poleward displaced upper-level westerly jet, and lower-level westerly flow in the northern tropics over the Arabian Sea, Bay of Bengal, and Indian sub-continent. These features are also evident in a zonal average over the SASM sector (Fig. 4.8), which additionally reveals two distinct upper-level westerly jets in the southern hemisphere, with the subtropical jet centered near 30°S and the

midlatitude jet centered near 45°S .

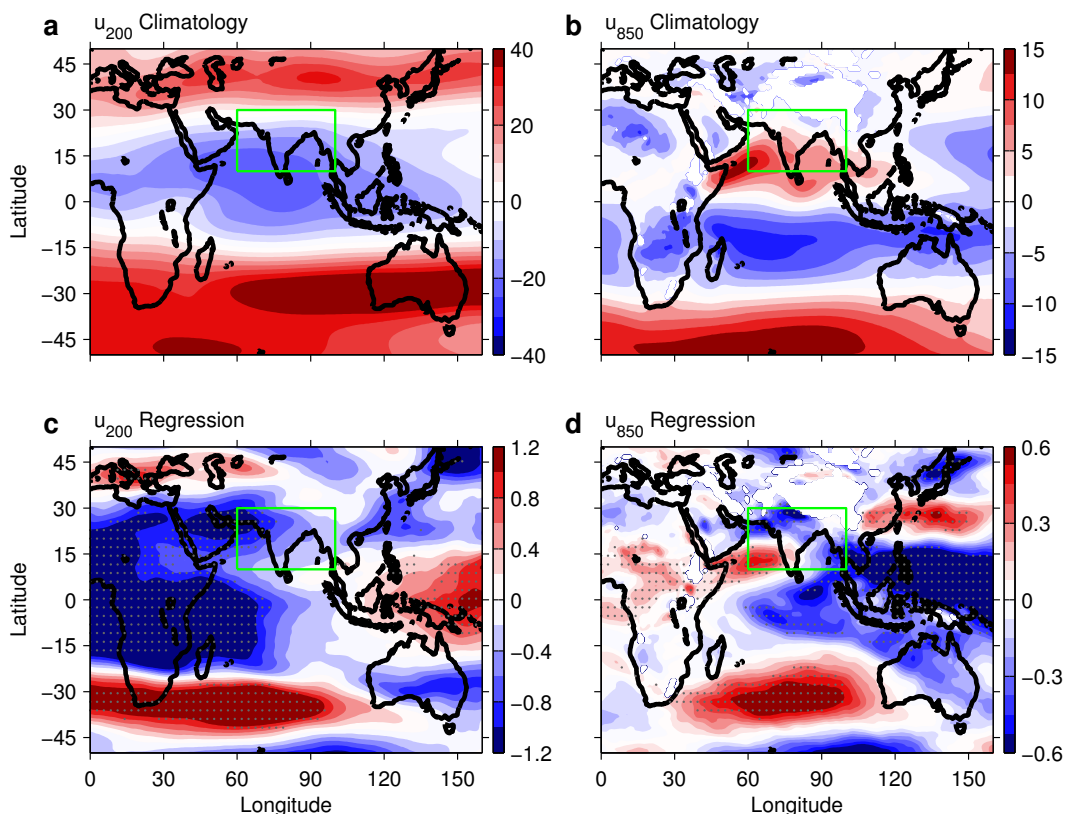


Figure 4.7: Climatology (a-b) and regression coefficient onto MFC index (c-d) of JJAS ERA-Interim zonal wind (m s^{-1}) at 200 hPa and 850 hPa. Gray stippling shows the regions where the regression coefficient is significant at the 5% level. The green rectangle shows the averaging region for the MFC index.

Linear regression onto the MFC index shows that strong monsoons are associated with a strengthened upper-level easterly jet in the tropics, enhanced lower-level westerly flow over the Arabian Sea, decreased lower-level westerly flow over the eastern Bay of Bengal, and increased lower-level easterly trade winds throughout the tropical Pacific Ocean (Fig. 4.7), consistent with previous findings (Webster and Yang, 1992; Wang and Fan, 1999). The zonally asymmetric lower-level zonal wind anomalies over the SASM region are consistent with the precipitation anomalies shown in Fig. 4.3b, with weakened zonal winds and weakened convergence over the eastern Bay of Bengal, corresponding to weakened precipitation in strong monsoons.

Figs. 4.7 and 4.8 also show correlations between the MFC index and the zonal winds in the extratropics, with significant correlations in the southern hemisphere; these will be explored further in Section 5.

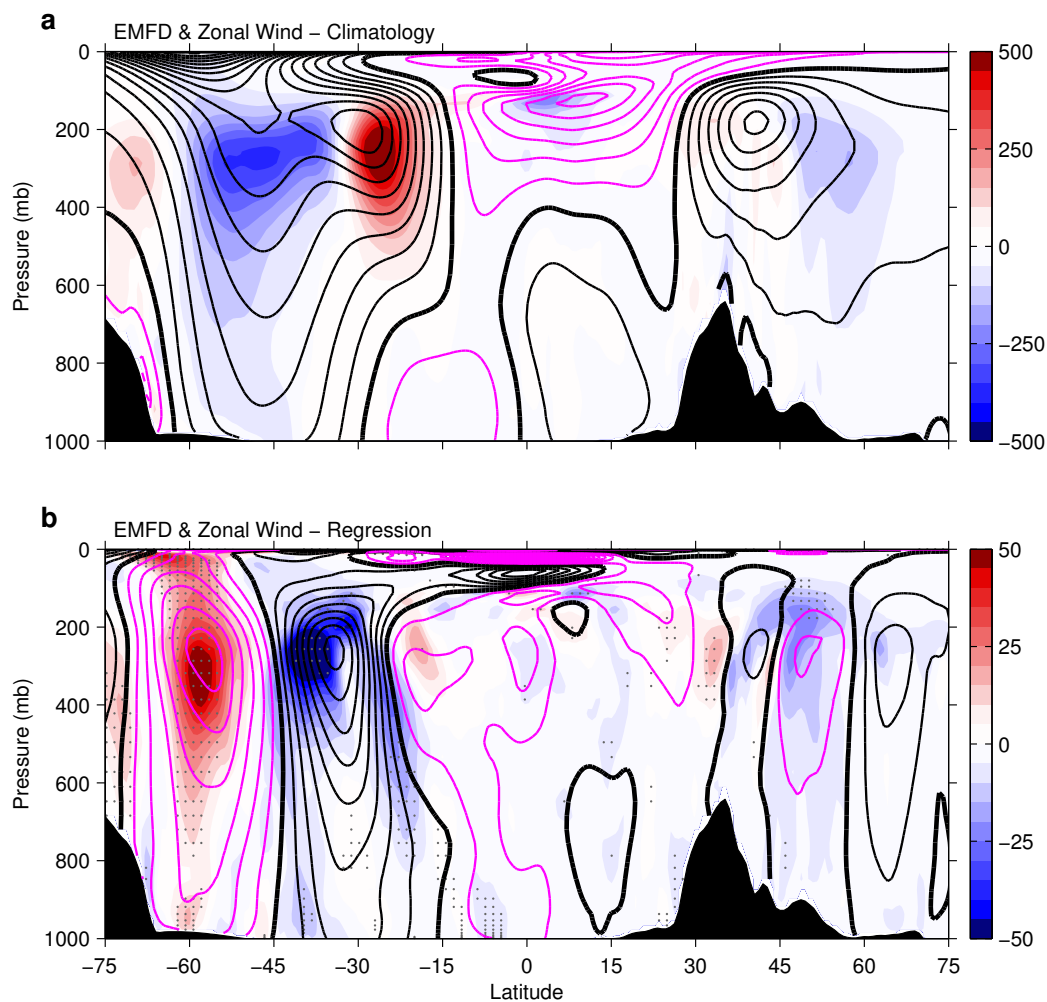


Figure 4.8: Climatology (a) and regression coefficient onto MFC index (b) of JJAS ERA-Interim SASM sector EMFD (colors, m s^{-2}) and zonal wind (contours, m s^{-1}). Positive contours are in black, negative contours in violet, and zero contours in heavy black. Gray stippling shows the regions where the EMFD regression coefficient is significant at the 5% level. Black shading shows the sector mean topography. Contour levels of zonal wind are: (a) 5 m s^{-1} and (b) 0.25 m s^{-1} .

Atmospheric temperature

In addition to the meridional overturning circulation and zonal winds, we look at atmospheric temperatures, particularly their meridional gradient, to seek patterns in upper- and lower-level temperatures associated with strong (weak) monsoons and to investigate the land-sea thermal contrast in the context of interannual variability. If the monsoon is largely driven by the land-sea thermal contrast, then we might expect that stronger monsoons would be accompanied by an increased near-surface

thermal contrast, with higher than average temperatures over India and/or lower than average temperatures over the Indian Ocean. However, as far back as 1921, it was observed that average temperature in India is higher in summers with low monsoon rainfall than in summers with high monsoon rainfall (Simpson, 1921).

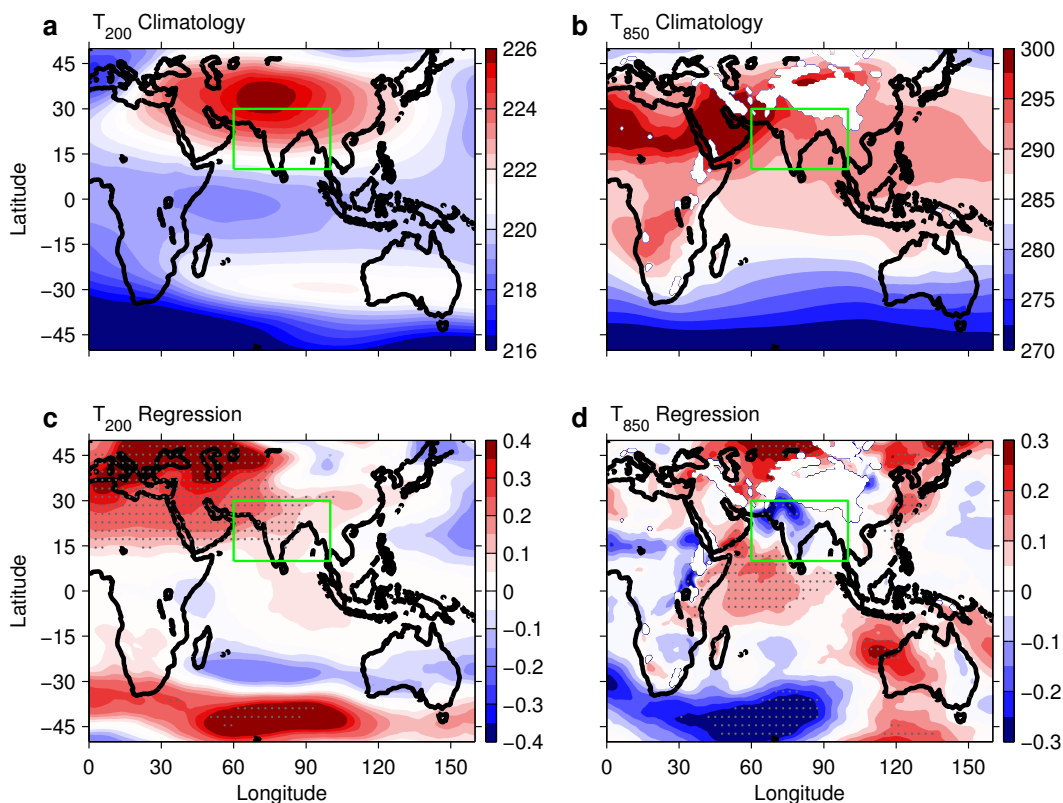


Figure 4.9: Climatology (a-b) and regression coefficient onto MFC index (c-d) of JJAS ERA-Interim atmospheric temperature (K) at 200 hPa and 850 hPa. Gray stippling shows the regions where the regression coefficient is significant at the 5% level. The green rectangle shows the averaging region for the MFC index.

Fig. 4.9 shows the climatology of ERA-Interim atmospheric temperatures at 850 hPa and 200 hPa. We see the reversal of the meridional temperature gradient at both levels, with temperature increasing poleward, and a strong maximum in upper-level temperature west of the Tibetan Plateau, consistent with previous studies (Molnar et al., 2010). Linear regression onto the monsoon index shows that strong monsoons are associated with an increased meridional gradient in upper-tropospheric temperature in the monsoon region (Fig. 4.9c) (Li and Yanai, 1996; Sun et al., 2010; Hurley and Boos, 2013; Dai et al., 2013). We also see that strong monsoons are associated with positive anomalies in upper-level atmospheric temperature in the subtropics and extratropics of both hemispheres (Fig. 4.9c), consistent with a previous study

(Hurley and Boos, 2013). This symmetric pattern can be partially understood through axisymmetric theories of the circulation induced by off-equatorial heating (Lindzen and Hou, 1988), which argue that for angular momentum conserving cross-equatorial circulations, free-tropospheric temperatures are symmetric about the equator, with an equatorial minimum and subtropical maxima in each hemisphere. For a circulation with ascending branch farther poleward, the subtropical maxima likewise shift poleward, along with the equatorial minimum becoming more pronounced. While similar changes are seen in subtropical temperatures (Fig. 4.9c), a deepening of the equatorial temperature minimum is not evident.

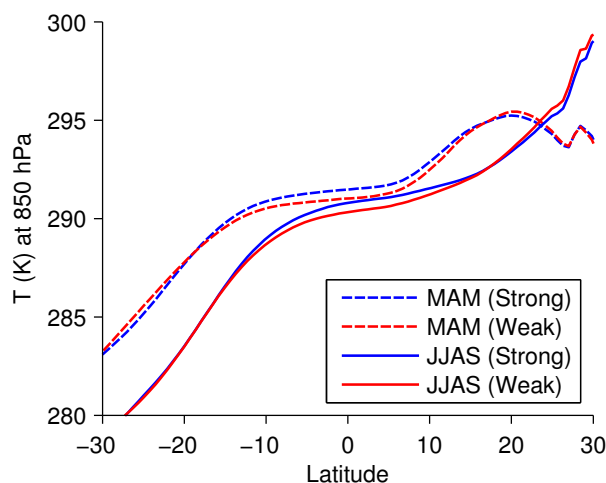


Figure 4.10: SASM sector lower-tropospheric temperature (K) in MAM (dashed) and JJAS (solid) for “Strong” (blue) and “Weak” (red) monsoons, using ERA-Interim temperatures at 850 hPa.

Fig. 4.9 shows that strong monsoons are correlated with negative anomalies in near-surface temperature over India and a reduced meridional gradient in near-surface temperature between India and the ocean to the south. When the 850 hPa atmospheric temperature is averaged over land only (T_{land}) and over ocean only (T_{ocean}) over the region from 60-100°E, 10°S-30°N, we find that the near-surface land-ocean thermal contrast $dT = T_{land} - T_{ocean}$ is negatively correlated with the monsoon strength index, with a statistically significant correlation coefficient of -0.46 .

These results are consistent with a similar linear regression involving sub-cloud atmospheric temperatures in a previous study (Hurley and Boos, 2013), but they are inconsistent with other studies (Sun et al., 2010; Dai et al., 2013), which found a positive correlation between monsoon strength and lower-tropospheric thermal

contrast (although this correlation was much weaker than the correlation with upper-level thermal contrast). A possible reason for this discrepancy is the choice of monsoon index. Sun et al. (2010) and Dai et al. (2013) use the shear-based Webster-Yang index for monsoon strength, which by construction is more strongly correlated with the meridional temperature gradient; however, it correlates less strongly with measures of monsoon precipitation and circulation strength.

One might posit that the near-surface thermal contrast could be higher than average in the spring and early stages of a strong summer monsoon, driving a stronger circulation. Once the monsoon has matured, the increased rainfall and soil moisture cool the lower troposphere over the Indian sub-continent, resulting in a negative correlation in the overall JJAS average. To investigate this possibility, we regressed the preceding spring March-May (MAM) averaged atmospheric temperatures onto the JJAS summer monsoon index and found that a reduced meridional gradient in near-surface temperature is also present in the spring preceding a strong monsoon, as illustrated in the “Strong” and “Weak” temperature profiles in Fig. 4.10. Comparing all reanalysis datasets, we do not find any robust indication of an increased near-surface thermal contrast in the spring preceding a strong monsoon, whereas we do find a robust decreased near-surface thermal contrast during the JJAS monsoon season. These results suggest that the near-surface temperature gradient should not be considered as an external forcing for the monsoon, but is itself a response to the atmospheric circulation, with stronger monsoonal circulations and increased monsoon rainfall smoothing the thermal gradient.

The regression of near-surface atmospheric temperatures onto the MFC index also shows statistically significant correlations in the southern-hemisphere extratropics, with strong monsoons correlated with a negative anomaly in near-surface temperature from approximately 30°S to 50°S, throughout the SASM longitudes and to the west (Fig. 4.9). The center of the cooling anomaly and the boundary between cooling and warming anomalies vary in longitude between reanalysis datasets, with these features shifted west in some datasets compared to ERA-Interim; however, the presence of a cooling anomaly over the extratropical southern Indian Ocean is a robust feature across all reanalysis products. This teleconnection pattern will be explored further in Section 5.

To investigate the possible role of convective quasi-equilibrium in the SASM circulation, we also looked at sub-cloud equivalent potential temperatures (θ_{eb}) in the five reanalysis datasets (not shown). Consistent with quasi-equilibrium and previ-

ous observational studies (Nie et al., 2010; Hurley and Boos, 2013), we find that the latitude of maximum θ_{eb} coincides with the latitude of maximum upper-level temperature in the climatology. Performing a linear regression analysis of θ_{eb} onto the MFC index, we find that strong monsoons are associated with an increased meridional gradient in JJAS sub-cloud equivalent potential temperature (θ_{eb}) across the SASM region, while the latitude of maximum θ_{eb} is the same for strong and weak monsoons, consistent with previous findings (Hurley and Boos, 2013).

4.5 Teleconnections with southern hemisphere extratropics

The northward shift of the monsoonal circulation during strong monsoon years (Fig. 4.4), along with the lower near-surface air temperature over the extratropical southern Indian Ocean (Fig. 4.9), is suggestive of a possible link between the monsoonal circulation and extratropical southern hemisphere thermal forcing. Recent model studies (e.g., Chiang and Bitz, 2005; Broccoli et al., 2006; Kang et al., 2008; Chiang and Friedman, 2012; Frierson and Hwang, 2012; Bischoff and Schneider, 2014; Schneider et al., 2014) have shown that thermal forcing in the extratropics can induce a shift in the zonally-averaged ITCZ toward a differentially warming hemisphere: The extratropical thermal forcing is communicated by anomalous mid-latitude eddy energy export out of the tropics, and the Hadley circulation responds with an anomalous cross-equatorial component. The anomalous Hadley circulation causes an energy transport away, and a moisture transport toward, the differentially heated hemisphere. The findings that strong monsoons years are associated with both a poleward shift of the circulation's ascending branch (Fig. 4.4) and anomalous cooling in the southern hemisphere midlatitudes (Fig. 4.9) suggest that similar mechanisms may be operating within the SASM sector on interannual time scales.

To investigate this further, we perform linear regression analysis of the mass-weighted vertically integrated transient eddy fluxes of moist static energy (MSE) against the MFC index. We find that strong monsoons are associated with negative anomalies in MSE eddy fluxes, dominated by dry static energy fluxes, in a wide band from approximately 30-45°S (Fig. 4.11). Although this feature is only statistically significant in a narrow range of longitudes according to the point-wise t-test we use, it is spatially correlated across a broad longitude band, suggesting it is dynamically significant. It is also robust across all reanalysis datasets except NCEP2. This suggests that within the SASM sector during strong monsoons, extratropical cooling and increased poleward eddy energy flux in the southern hemisphere might play a role in the northward shift of the monsoon circulation, in analogy to the response

of the zonally-averaged precipitation to extratropical forcing. Lending further evidence to this hypothesis, we find that an increase of one standard deviation in MFC is associated with a statistically significant anomalous cross-equatorial MSE transport (primarily by the mean meridional overturning circulation) of -1.7 PW across the SASM sector; that is, the northward shift of the SASM circulation and anomalous cooling in the southern hemisphere extratropics during a strong monsoon are accompanied by anomalous southward cross-equatorial energy transport toward the differentially cooler hemisphere.¹ Of course, these correlations alone are not sufficient to establish causality, and future modeling work will be needed to determine the mechanisms involved and the direction of causality.

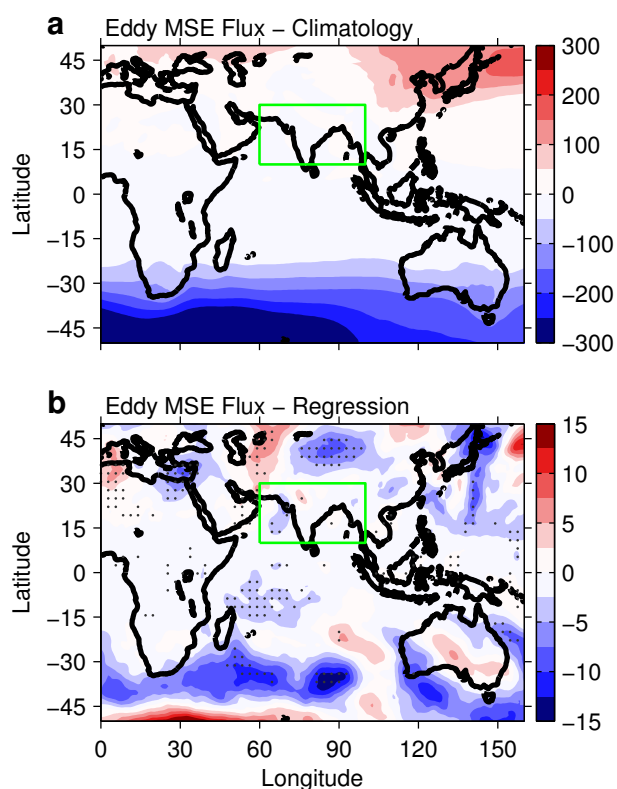


Figure 4.11: Climatology (a) and regression coefficient onto monsoon index (b) of JJAS ERA-Interim vertically integrated MSE transient eddy fluxes (kW M^{-1}). Gray stippling shows the regions where the regression coefficient is significant at the 5% level. The green rectangle shows the averaging region for the MFC index.

The southern hemisphere cooling associated with strong SASM is also consistent

¹We find a similar result when using the energy fluxes from ERA-Interim derived components provided by NCAR (<https://climatedataguide.ucar.edu/climate-data/era-interim-derived-components>), in which the mass budget is balanced with a barotropic wind correction (Trenberth, 1997b).

with findings by Wang et al. (2013) for the global monsoon, who found that there is a significant positive correlation between the strength of the northern hemisphere summer monsoon and the thermal contrast between the northern and southern hemispheres.

Since the eddy dry static energy fluxes comprise the vertical component of the Eliassen-Palm (EP) flux, our findings suggest that variations in southern hemisphere wave activity are associated with monsoon variations. To further explore this teleconnection, we look at the eddy momentum fluxes, which represent the meridional component of the EP flux. We perform linear regression analysis of the SASM sector average eddy momentum flux divergence (EMFD) and zonal winds onto the MFC index. Fig. 4.8a shows the JJAS climatology of the monsoon sector zonal winds and transient EMFD. In the southern hemisphere, we see a region of momentum divergence in the upper troposphere extending approximately from 15°S to 30°S , within the subtropical westerly jet centered near 30°S , a region of momentum convergence in the upper troposphere extending approximately $30 - 60^{\circ}\text{S}$, within the region of maximum baroclinicity, and a midlatitude jet centered near 45°S . The zero contour of the zonal wind closely follows the edge of the region of EMFD, indicating that large-scale extratropical eddies do not propagate past their critical latitudes (Randel and Held, 1991).

The linear regression of EMFD and zonal wind onto the MFC index reveals correlations in the southern hemisphere extratropics that are robust across datasets. Both regression fields display a dipole pattern, in which strong monsoons are associated with positive (negative) anomalies in zonal wind (EMFD) from approximately $20 - 45^{\circ}\text{S}$ and negative (positive) anomalies in zonal wind (EMFD) from approximately $45 - 70^{\circ}\text{S}$ (Fig. 4.8). Fig. 4.12 shows strong and weak monsoon composites (as defined in the previous section) of zonal wind and EMFD in the southern hemisphere. We can see that in strong monsoon years relative to weak monsoon years: 1) the midlatitude jet weakens and shifts approximately 3° equatorward (from approximately 49°S to 46°S); 2) the subtropical jet strengthens and shifts approximately 2° poleward (from approximately 29°S to 31°S); 3) the separation between the subtropical and midlatitude jets is reduced from approximately 20° to 15° ; and 4) the region of eddy momentum flux convergence strengthens and its maximum shifts approximately 15° equatorward (from approximately 54°S to 39°S). These features suggest an equatorward shift of the midlatitude jet, which comes closer to merging with the subtropical jet. This is consistent with the enhanced near-surface

meridional temperature gradient between the southern hemisphere subtropics and midlatitudes (Fig. 4.9d), implying stronger upper-level westerlies between 20-45°S, by thermal wind balance (Fig. 4.7d). This results in enhanced baroclinicity farther equatorward and so more eddy momentum flux convergence (wave activity divergence) farther equatorward. The strengthened subtropical jet may also result from increased angular momentum advection by the stronger monsoonal circulation.

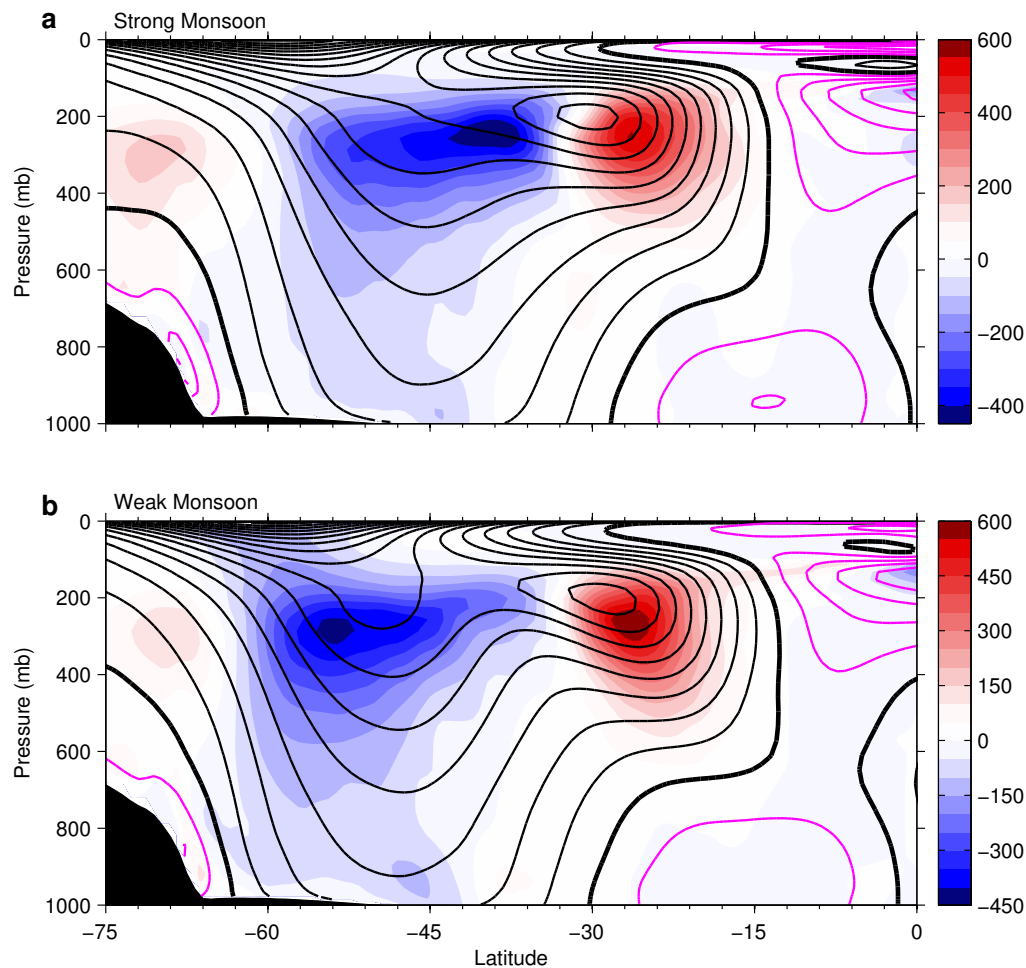


Figure 4.12: Southern hemisphere JJAS ERA-Interim SASM sector EMFD (colors, m s^{-2}) and zonal wind (contours, m s^{-1}) representing (a) “Strong” and (b) “Weak” SASM years. Zonal wind contours are 5 m s^{-1} , with positive contours in black, negative contours in violet, and zero contours in heavy black. Black shading shows the sector mean topography.

The changes in southern hemisphere extratropical EMFD and eddy-driven jet that accompany strong (weak) monsoons are similar to those associated with Southern

Annular Mode variability (Thompson and Wallace, 2000; Barnes and Hartmann, 2010; Hendon et al., 2014), although more zonally localized. This suggests an association between SASM and Southern Annular Mode variability, which will be explored in more depth in future work. These features are also qualitatively consistent with findings by Ceppi and Hartmann (2013), who find interannual correlations between the position of the descending branch of the Hadley cell and the speed of the eddy-driven jet in the full zonal mean.

4.6 Correlations with modes of SST variability

Since ENSO is one of the main modes of interannual variability associated with the SASM strength (e.g., Webster et al., 1998; Meehl, 1987), we use the ENSO index described in Section 2 to determine the correlation between our monsoon index and ENSO, as well as the extent to which our findings are correlated with ENSO variability.

There is a statistically significant negative correlation of -0.39 between MFC and ENSO, consistent with previous studies, which have found that strong El Niño warm events are often associated with Indian monsoon failures (e.g., Pant and Parthasarathy, 1981; Rasmusson and Carpenter, 1982).

To investigate the role of ENSO variability in the findings presented in Sections 4 and 5, we repeat the analyses with linear variability associated with the ENSO index removed from all fields and the resulting fields regressed onto the MFC index (not shown). We find that the anomalies in the monsoonal meridional overturning circulation, precipitation, and temperature within the SASM region, and southern hemisphere EMFD in strong (weak) monsoons are not significantly related to ENSO variability. Some anomalies in extratropical zonal wind, temperature, and eddy energy fluxes associated with strong (weak) monsoons are partially related to, but not completely accounted for by ENSO variability; these anomalies are weakened but still evident and statistically significant when ENSO variability is removed. In general, ENSO variability is not the predominant mode of variability for any of the findings presented here.

Since ENSO and IOD both measure zonal asymmetries of SSTs, we also use both indices to explore in more detail the anti-correlation in monsoon precipitation anomalies between the eastern Bay of Bengal and the rest of the SASM domain (Fig. 4.3 and related discussion in Section 4). We find that the anti-correlation is still evident and statistically significant when ENSO is removed. A similar analysis also

shows that the IOD index, described in Section 2, has a negligible contribution to the anti-correlation in the precipitation anomalies. Thus, the zonal asymmetry in interannual variability of precipitation between South Asia and the eastern Bay of Bengal is not linearly related to either ENSO or IOD.

4.7 Summary and concluding remarks

We investigated the interannual variability of precipitation and large-scale dynamics of the SASM using reanalysis and precipitation data from various sources. Using the vertically integrated moisture flux convergence in the SASM region as an index for monsoon strength, we decomposed the net precipitation variability into dynamic and thermodynamic components, and we performed linear regression analyses to identify numerous coherent and robust large-scale atmospheric patterns associated with monsoon variations. We find that:

1. The interannual variability of the monsoonal precipitation is mainly due to variability in circulation rather than variability in moisture.
2. Strong monsoons are characterized by a northward shift of the ascending branch of the cross-equatorial monsoonal circulation.
3. There is a negative correlation between the SASM strength and the near-surface thermal contrast between the continent and the Indian Ocean, in contrast with the traditional view of monsoons as land-sea breeze circulations. This suggests that the near-surface atmospheric temperature distribution is itself a response to the atmospheric circulation rather than a forcing factor.
4. Within the SASM sector, teleconnections exist between the monsoon strength and the southern hemisphere extratropical atmospheric temperatures, eddy MSE fluxes, EMFD, and jet structure.

In the southern hemisphere extratropics, strong monsoon years are correlated with near-surface atmospheric cooling and increased poleward eddy fluxes of MSE in the southern hemisphere midlatitudes, suggesting that extratropical thermal forcing in the winter hemisphere may play a role in the northward shift of the monsoonal circulation during strong monsoons. Strong monsoons are also associated with southern hemisphere variability similar to the Southern Annular Mode, with a northward shift and strengthening of eddy momentum flux convergence in the southern hemisphere

extratropics, accompanied by a northward shift of the midlatitude westerly jet and strengthening of the subtropical westerly jet.

Although our findings are suggestive of a possible mechanism contributing to the interannual variability of the SASM, namely, an extratropical thermal forcing in the southern hemisphere leading to a northward shift in the monsoonal circulation during strong monsoons, in order to confirm causality the observational analysis will need to be supplemented with modeling work, including an analysis of zonal energy fluxes, to assess the extent to which mechanisms found in the zonal mean are operating within the monsoon sector. Modeling studies similar to Kang et al. (2014) may be relevant to understanding the mechanisms underlying the observational findings presented here. In addition, although the northward shift of the monsoonal circulation during strong monsoons is a robust finding across all datasets examined here, these datasets are inconclusive regarding whether the northward shift in circulation is accompanied by a northward shift in the latitude of maximum precipitation within the SASM sector. Further analysis is needed to clarify this relationship. Despite these caveats, this study reveals robust large-scale connections between the southern hemisphere and the SASM on interannual time scales. Further examination of these connections will eventually result in better understanding and prediction of SASM interannual variability.

In contrast to the interannual variability we examined, changes in monsoon precipitation in response to greenhouse warming in climate models are dominated by the thermodynamic component, rather than the dynamic component (e.g., Cherchi et al., 2011; Hsu et al., 2013). Since these global warming simulations cover a much wider range of temperature increases than the interannual variability within the current climate, it seems reasonable that the thermodynamic component plays a much larger role in these climate experiments. It will be of interest to explore if SASM interannual variability in historical climate simulations in the World Climate Research Programme Coupled Model Intercomparison Project Phase 5 (CMIP5) reveals similar patterns as the ones highlighted in this observational study.

4.8 Appendix: Long-term trends

In our analysis we have focused on the interannual variability of the SASM during JJAS, with the long-term trends omitted from all fields. In this section we investigate long-term trends in SASM rainfall inferred from reanalysis, gauge-based, and satellite data products.

Identification of long-term trends in the seasonal-mean SASM rainfall is complicated by variability on interdecadal and sub-seasonal time scales, as well as regional variability within the SASM domain and inconsistencies between precipitation datasets. Some studies indicate the presence of a long-term decreasing trend in Indian summer monsoon rainfall since the mid 20th century (e.g., Ramanathan et al., 2005; Bollasina et al., 2011; Turner and Annamalai, 2012). Gautam et al. (2009) find a steady increase in June rainfall over India in recent decades, accompanied by a decreasing trend in rainfall from July to September. Analysis of precipitation over numerous regions in India indicates compensating positive and negative long-term trends in different regions, tending to cancel out in the area average (Naidu et al., 2009). Goswami et al. (2006a) find increasing trends in the frequency and magnitude of extreme rain events over India in recent decades, with no significant long-term trend in the seasonal mean monsoon rainfall due to the compensating tendencies of extreme wet and dry events.

We investigate the long-term trends in SASM precipitation in the datasets previously discussed (ERA-Interim, ERA40, NCEP1, NCEP2, 20CENTURY, GPCP, and AIR), as well as the following precipitation products: CPC Merged Analysis of Precipitation (CMAP), a merged analysis of rain gauge, satellite and reanalysis data (Xie and Arkin, 1997); gauge-based data from the University of East Anglia Climatic Research Unit (CRU; Harris et al., 2014); NOAA's gauge-based PRECipitation REConstruction over Land (PREC/L; Chen et al., 2002); and satellite-based precipitation estimates from NASA's Tropical Rainfall Measuring Mission (TRMM; Huffman et al., 2007). For all datasets we compute trends over the common period from 1979 to 2011, except for ERA40 (1979-2002) and TRMM (1998-2011), which do not cover the entire 33-year period.

Figs. 4.13 and 4.14 show the linear trends in JJAS precipitation over the SASM domain. There is substantial regional variability throughout the domain, with most datasets indicating statistically significant positive and negative trends in different regions. There is little agreement between the datasets, and no robust regional patterns are evident.

The area average JJAS rainfall over the SASM domain is shown in Fig. 4.15 for the period 1979-2011, and the values filtered by a 5-year running mean are shown in Fig. 4.16. In the unfiltered values in Fig. 4.15, it is evident that the interannual variability dominates over the long-term trend in all datasets except NCEP2. In the 5-year running mean values (Fig. 4.16), we see positive trends in some datasets

and negative trends in others, as well as strong interdecadal variability in all of the precipitation datasets (Fig. 4.16b) which is not evident in the reanalysis products (Fig. 4.16a). The linear trends computed from the SASM area averages are summarized in Table 4.1. Statistically significant trends are found only within the reanalysis products, and these include both positive and negative trends.

Thus, it is difficult to draw any general conclusions about the long-term trends in SASM rainfall in recent decades. Discrepancies among datasets are large, as are regional variations within the domain.

Table 4.1: Linear trends in SASM JJAS yearly and 5-year running mean precipitation ($\text{mm day}^{-1} (33 \text{ years})^{-1}$) over the period 1979-2011 (ERA40: 1979-2002, TRMM:1998-2011). All values are based on area averages over the region 60-100°E, 10-30°N, except AIR which is an average over India. The trend in 5-year running mean is omitted from TRMM due to insufficient number of years in the data. Trends which are statistically significant at the 5% level are in bold.

Dataset	Yearly Trend	5-yr Trend
ERA-I	+0.72	+0.59
ERA40	+1.89	+1.87
NCEP1	-0.56	-0.72
NCEP2	-1.30	-1.56
20CENTURY	-0.23	-0.55
AIR	+0.09	-0.10
CMAP	+0.12	+0.13
CRU	+0.68	+0.42
GPCP	+0.35	+0.23
PREC/L	+0.53	+0.12
TRMM	+1.95	N/A

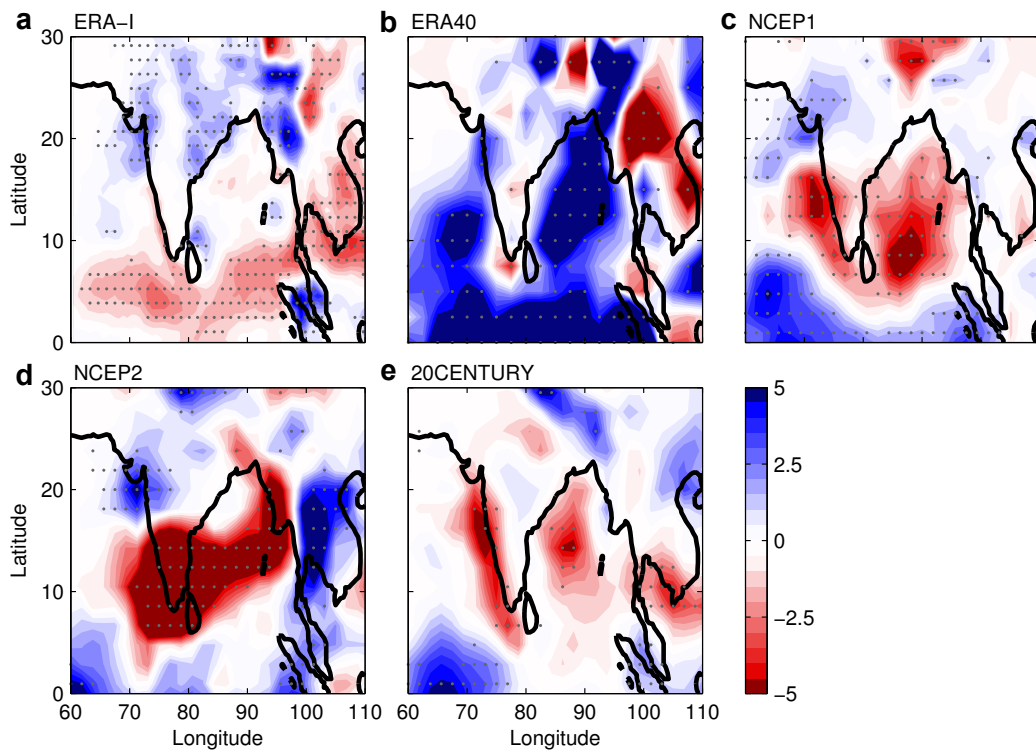


Figure 4.13: Linear trend ($\text{mm day}^{-1} \text{ year}^{-1}$) in reanalysis precipitation over the period 1979-2011 (ERA40: 1979-2002). Gray stippling shows the regions where the trend is significant at the 5% level.

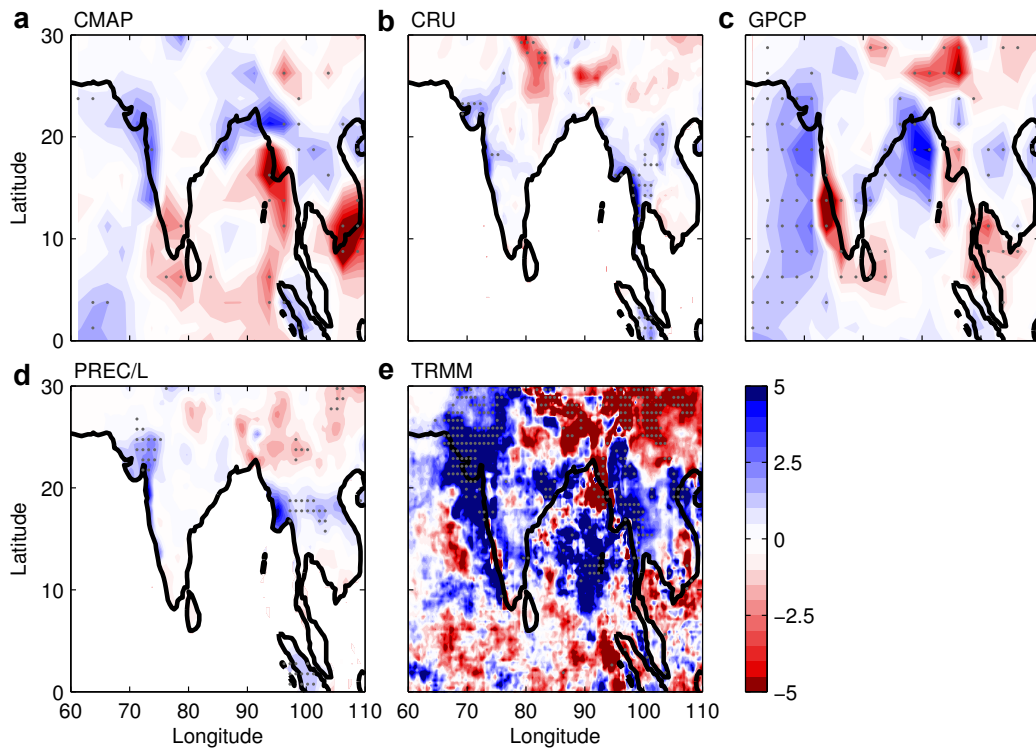


Figure 4.14: Same as in Fig. 4.13, but for various other precipitation datasets. Trends computed over 1979-2011 (TRMM: 1998-2011).

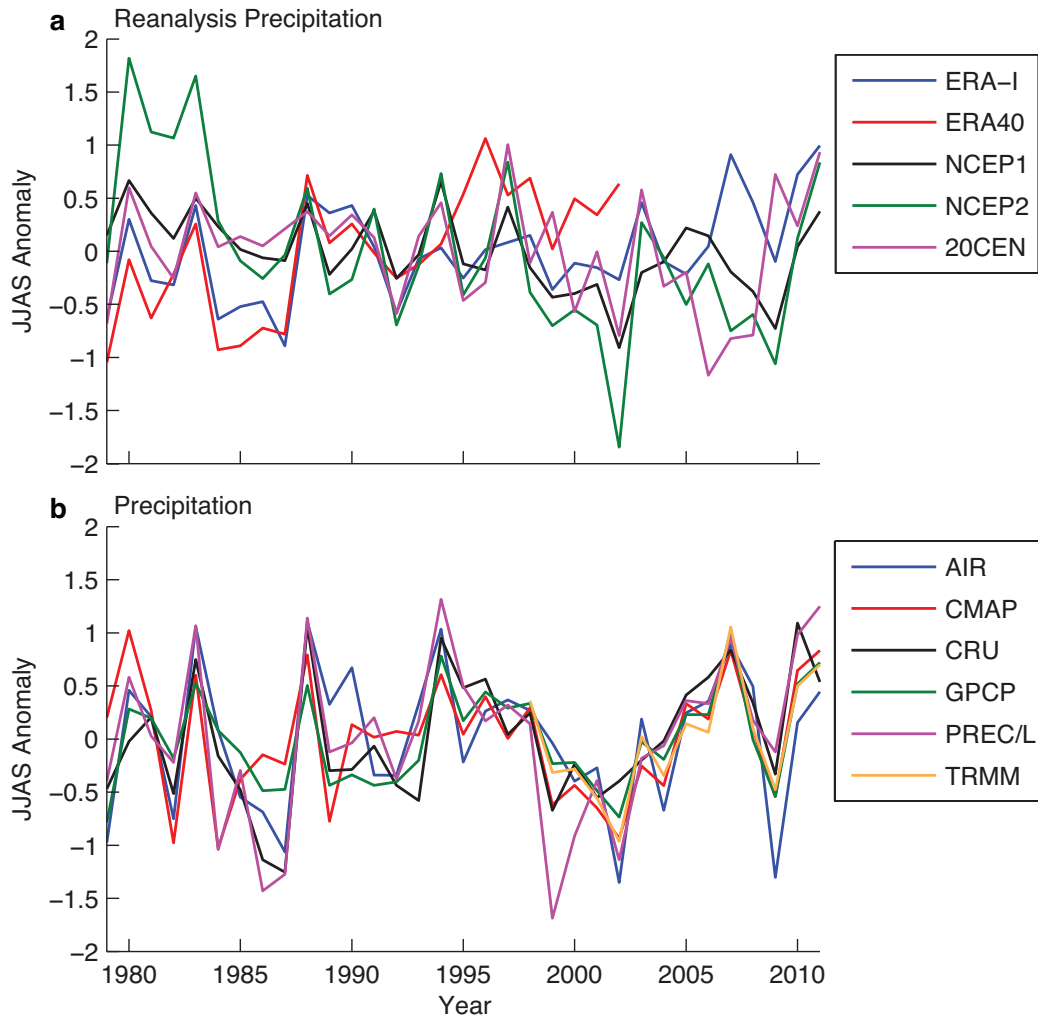


Figure 4.15: Anomalies in SASM JJAS precipitation (mm day^{-1}) in reanalysis and precipitation data over the period 1979-2011 (ERA40: 1979-2002, TRMM: 1998-2011). All values are based on area averages over the region $60\text{-}100^\circ\text{E}$, $10\text{-}30^\circ\text{N}$, except AIR which is an average over India.

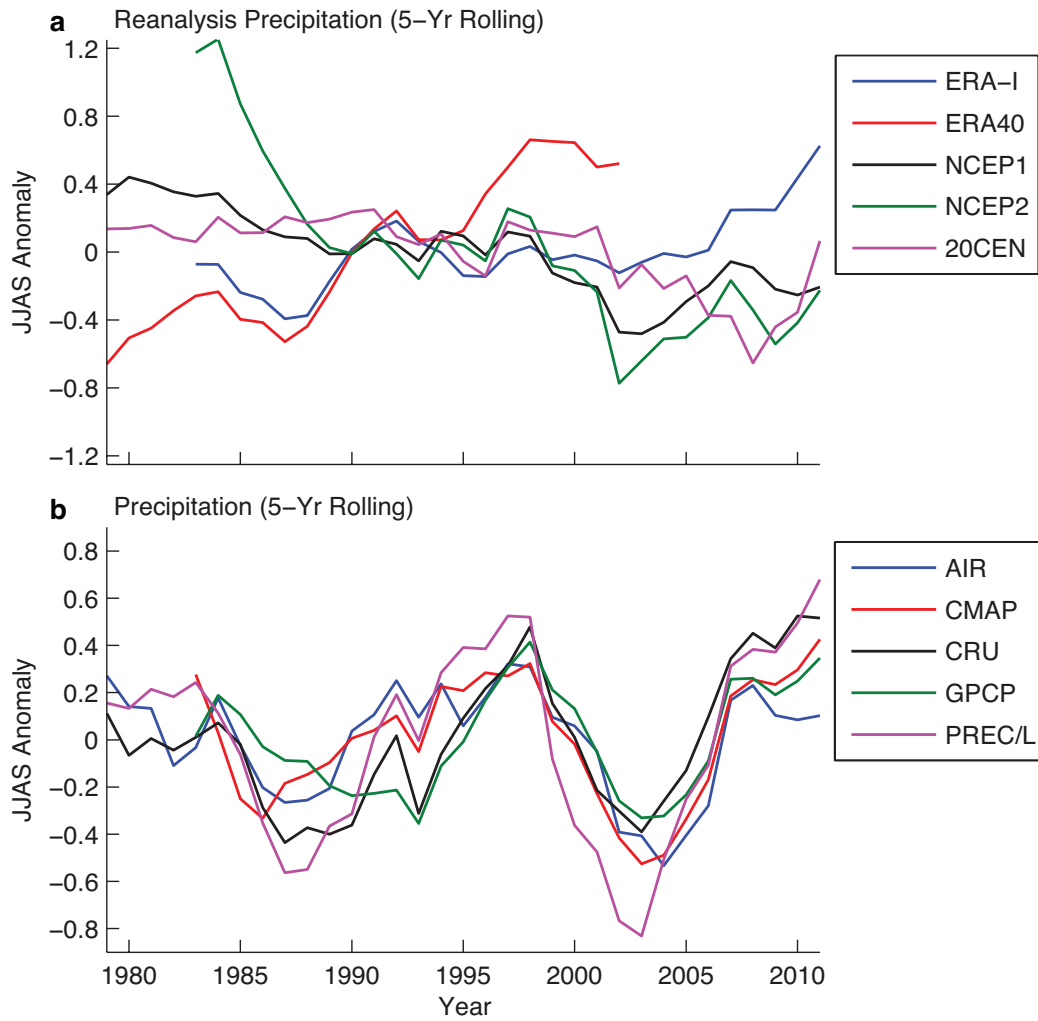


Figure 4.16: Same as in Fig. 4.15, but with 5-year running mean.

BIBLIOGRAPHY

- Adam, O., T. Bischoff, and T. Schneider (2016). “Seasonal and Interannual Variations of the Energy Flux Equator and ITCZ. Part I: Zonally Averaged ITCZ Position”. In: *J. Clim.* 29.9, pp. 3219–3230. DOI: 10.1175/JCLI-D-15-0512.1.
- Adamson, G. C. D. and D. J. Nash (2012). “Long-term variability in the date of monsoon onset over western India”. In: *Clim. Dyn.* 40, pp. 2589–2603. DOI: 10.1007/s00382-012-1494-x.
- Adler, R. F., G. J. Huffman, A. Chang, R. Ferraro, P.-P. Xie, J. Janowiak, B. Rudolf, U. Schneider, S. Curtis, D. Bolvin, A. Gruber, J. Susskind, P. Arkin, and E. Nelkin (2003). “The Version-2 Global Precipitation Climatology Project (GPCP) Monthly Precipitation Analysis (1979-Present)”. In: *J. Hydrometeorol.* 4.6, pp. 1147–1167. DOI: 10.1175/1525-7541(2003)004<1147:TVGPCP>2.0.CO;2.
- Ailikun, B. and T. Yasunari (1998). “On the two indices of Asian summer monsoon variability and their implications”. In: *Ext. Abstr. Int. Conf. Monsoon Hydrol. Cycle*. Kyongju, Korea: Korean Meteorological Society, pp. 222–224.
- Ananthkrishnan, R. and M. K. Soman (1988). “The onset of the southwest monsoon over Kerala: 1901–1980”. In: *J. Climatol.* 8.3, pp. 283–296. DOI: 10.1002/joc.3370080305.
- Barnes, E. A. and D. L. Hartmann (2010). “Dynamical Feedbacks of the Southern Annular Mode in Winter and Summer”. In: *J. Atmos. Sci.* 67.7, pp. 2320–2330. DOI: 10.1175/2010JAS3385.1.
- Bischoff, T. and T. Schneider (2014). “Energetic Constraints on the Position of the Intertropical Convergence Zone”. In: *J. Clim.* 27.13, pp. 4937–4951. DOI: 10.1175/JCLI-D-13-00650.1.
- Blanford, H. F. (1884). “On the connexion of the Himalaya snowfall with dry winds and seasons of drought in India”. In: *Proc. R. Soc. London* 37, pp. 3–22.
- Bollasina, M. A., Y. Ming, and V. Ramaswamy (2011). “Anthropogenic Aerosols and the Weakening of the South Asian Summer Monsoon.” In: *Science* 334.6055, pp. 502–505. DOI: 10.1126/science.1204994.
- Boos, W. R. and K. A. Emanuel (2008a). “Wind–Evaporation Feedback and Abrupt Seasonal Transitions of Weak, Axisymmetric Hadley Circulations”. In: *J. Atmos. Sci.* 65.7, pp. 2194–2214. DOI: 10.1175/2007JAS2608.1.
- Boos, W. R. and K. A. Emanuel (2008b). “Wind–Evaporation Feedback and the Axisymmetric Transition to Angular Momentum–Conserving Hadley Flow”. In: *J. Atmos. Sci.* 65.12, pp. 3758–3778. DOI: 10.1175/2008JAS2791.1.

- Boos, W. R. and K. A. Emanuel (2009). “Annual intensification of the Somali jet in a quasi-equilibrium framework: Observational composites”. In: *Q. J. R. Meteorol. Soc.* 135.639, pp. 319–335. DOI: 10.1002/qj.388.
- Bordoni, S. and T. Schneider (2008). “Monsoons as eddy-mediated regime transitions of the tropical overturning circulation”. In: *Nat. Geosci.* 1.8, pp. 515–519. DOI: 10.1038/ngeo248.
- Bosilovich, M., S. Akella, L. Coy, R. Cullather, C. Draper, R. Gelaro, R. Kovach, Q. Liu, A. Molod, P. Norris, K. Wargan, W. Chao, R. Reichle, L. Takacs, Y. Vikhliav, S. Bloom, A. Collow, S. Firth, G. Labow, G. Partyka, S. Pawson, O. Reale, S. D. Schubert, and M. Suarez (2015). “MERRA-2 : Initial Evaluation of the Climate”. In: *NASA Tech. Rep. Ser. Glob. Model. Data Assim.* 43.NASA/TM–2015-104606.
- Broccoli, A. J., K. A. Dahl, and R. J. Stouffer (2006). “Response of the ITCZ to Northern Hemisphere cooling”. In: *Geophys. Res. Lett.* 33.1, p. L01702. DOI: 10.1029/2005GL024546.
- Byrne, M. P. and P. A. O’Gorman (2013). “Land–Ocean Warming Contrast over a Wide Range of Climates: Convective Quasi-Equilibrium Theory and Idealized Simulations”. In: *J. Clim.* 26.12, pp. 4000–4016. DOI: 10.1175/JCLI-D-12-00262.1.
- Ceppi, P. and D. L. Hartmann (2013). “On the Speed of the Eddy-Driven Jet and the Width of the Hadley Cell in the Southern Hemisphere”. In: *J. Clim.* 26.10, pp. 3450–3465. DOI: 10.1175/JCLI-D-12-00414.1.
- Chao, W. C. (2000). “Multiple Quasi Equilibria of the ITCZ and the Origin of Monsoon Onset”. In: *J. Atmos. Sci.* 57.5, pp. 641–652. DOI: 10.1175/1520-0469(2000)057<0641:MQEOTI>2.0.CO;2.
- Chao, W. C. and B. Chen (2001). “The Origin of Monsoons”. In: *J. Atmos. Sci.* 58.22, pp. 3497–3507. DOI: 10.1175/1520-0469(2001)058<3497:T00M>2.0.CO;2.
- Chen, M., P. Xie, J. E. Janowiak, and P. A. Arkin (2002). “Global Land Precipitation: A 50-yr Monthly Analysis Based on Gauge Observations”. In: *J. Hydrometeorol.* 3.3, pp. 249–266. DOI: 10.1175/1525-7541(2002)003<0249:GLPAYM>2.0.CO;2.
- Cherchi, A., A. Alessandri, S. Masina, and A. Navarra (2011). “Effects of increased CO₂ levels on monsoons”. In: *Clim. Dyn.* 37.1-2, pp. 83–101. DOI: 10.1007/s00382-010-0801-7.
- Cherchi, A. and A. Navarra (2012). “Influence of ENSO and of the Indian Ocean Dipole on the Indian summer monsoon variability”. In: *Clim. Dyn.* 41.1, pp. 81–103. DOI: 10.1007/s00382-012-1602-y.
- Chiang, J. C. H. and C. M. Bitz (2005). “Influence of high latitude ice cover on the marine Intertropical Convergence Zone”. In: *Clim. Dyn.* 25.5, pp. 477–496. DOI: 10.1007/s00382-005-0040-5.

- Chiang, J. C. and A. R. Friedman (2012). “Extratropical Cooling, Interhemispheric Thermal Gradients, and Tropical Climate Change”. In: *Annu. Rev. Earth Planet. Sci.* 40.1, pp. 383–412. doi: 10.1146/annurev-earth-042711-105545.
- Chou, C., J. D. Neelin, and H. Su (2001). “Ocean-atmosphere-land feedbacks in an idealized monsoon”. In: *Q. J. R. Meteorol. Soc.* 127.576, pp. 1869–1891. doi: 10.1002/qj.49712757602.
- Clement, A. C., A. Hall, and A. Broccoli (2004). “The importance of precessional signals in the tropical climate”. In: *Clim. Dyn.* 22.4, pp. 327–341. doi: 10.1007/s00382-003-0375-8.
- Compo, G. P., J. S. Whitaker, P. D. Sardeshmukh, N. Matsui, R. J. Allan, X. Yin, B. E. Gleason, R. S. Vose, G. Rutledge, P. Bessemoulin, S. Brönnimann, M. Brunet, R. I. Crouthamel, a. N. Grant, P. Y. Groisman, P. D. Jones, M. C. Kruk, a. C. Kruger, G. J. Marshall, M. Maugeri, H. Y. Mok, Ø. Nordli, T. F. Ross, R. M. Trigo, X. L. Wang, S. D. Woodruff, and S. J. Worley (2011). “The Twentieth Century Reanalysis Project”. In: *Q. J. R. Meteorol. Soc.* 137.654, pp. 1–28. doi: 10.1002/qj.776.
- Cook, B. I. and B. M. Buckley (2009). “Objective determination of monsoon season onset, withdrawal, and length”. In: *J. Geophys. Res.* 114.D23, p. D23109. doi: 10.1029/2009JD012795.
- Dai, A., H. Li, Y. Sun, L.-C. Hong, L. Ho, C. Chou, and T. Zhou (2013). “The relative roles of upper and lower tropospheric thermal contrasts and tropical influences in driving Asian summer monsoons”. In: *J. Geophys. Res. Atmos.* 118.13, pp. 7024–7045. doi: 10.1002/jgrd.50565.
- de Boyer Montégut, C., G. Madec, A. S. Fischer, A. Lazar, and D. Iudicone (2004). “Mixed layer depth over the global ocean: An examination of profile data and a profile-based climatology”. In: *J. Geophys. Res. C Ocean.* 109.12, pp. 1–20. doi: 10.1029/2004JC002378.
- Dee, D. P., S. M. Uppala, A. J. Simmons, P. Berrisford, P. Poli, S. Kobayashi, U. Andrae, M. A. Balmaseda, G. Balsamo, P. Bauer, P. Bechtold, A. C. M. Beljaars, L. van de Berg, J. Bidlot, N. Bormann, C. Delsol, R. Dragani, M. Fuentes, A. J. Geer, L. Haimberger, S. B. Healy, H. Hersbach, E. V. Hólm, L. Isaksen, P. Kållberg, M. Köhler, M. Matricardi, A. P. McNally, B. M. Monge-Sanz, J.-J. Morcrette, B.-K. Park, C. Peubey, P. de Rosnay, C. Tavolato, J.-N. Thépaut, and F. Vitart (2011). “The ERA-Interim reanalysis: configuration and performance of the data assimilation system”. In: *Q. J. R. Meteorol. Soc.* 137.656, pp. 553–597. doi: 10.1002/qj.828.
- Dima, I. M. and J. M. Wallace (2003). “On the Seasonality of the Hadley Cell”. In: *J. Atmos. Sci.* 60.12, pp. 1522–1527. doi: 10.1175/1520-0469(2003)060<1522:OTSOTH>2.0.CO;2.

- Donohoe, A., J. Marshall, D. Ferreira, K. Armour, and D. McGee (2014). “The Interannual Variability of Tropical Precipitation and Interhemispheric Energy Transport”. In: *J. Clim.* 27.9, pp. 3377–3392. doi: 10.1175/JCLI-D-13-00499.1.
- Donohoe, A., J. Marshall, D. Ferreira, and D. Mcgee (2013). “The Relationship between ITCZ Location and Cross-Equatorial Atmospheric Heat Transport: From the Seasonal Cycle to the Last Glacial Maximum”. In: *J. Clim.* 26.11, pp. 3597–3618. doi: 10.1175/JCLI-D-12-00467.1.
- Emanuel, K. A. (1995). “On Thermally Direct Circulations in Moist Atmospheres”. In: *J. Atmos. Sci.* 52.9, pp. 1529–1534.
- Emanuel, K. A., J. D. Neelin, and C. S. Bretherton (1994). “On large-scale circulations in convecting atmospheres”. In: *Q. J. R. Meteorol. Soc.* 120.519, pp. 1111–1143. doi: 10.1002/qj.49712051902.
- Fasullo, J. and P. J. Webster (2003). “A Hydrological Definition of Indian Monsoon Onset and Withdrawal”. In: *J. Clim.* 16.19, pp. 3200–3211. doi: 10.1175/1520-0442(2003)016<3200a:AHDOIM>2.0.CO;2.
- Fieux, M. and H. Stommel (1977). “Onset of the Southwest Monsoon over the Arabian Sea from Marine Reports of Surface Winds: Structure and Variability”. In: *Mon. Weather Rev.* 105.2, pp. 231–236. doi: 10.1175/1520-0493(1977)105<0231:OOTSMO>2.0.CO;2.
- Flatau, M. K., P. J. Flatau, and D. Rudnick (2001). “The dynamics of double monsoon onsets”. In: *J. Clim.* 14.21, pp. 4130–4146. doi: 10.1175/1520-0442(2001)014<4130:TDODMO>2.0.CO;2.
- Frierson, D. M. W. and Y.-T. Hwang (2012). “Extratropical Influence on ITCZ Shifts in Slab Ocean Simulations of Global Warming”. In: *J. Clim.* 25.2, pp. 720–733. doi: 10.1175/JCLI-D-11-00116.1.
- Frierson, D. M. W., Y.-T. Hwang, N. S. Fučkar, R. Seager, S. M. Kang, A. Donohoe, E. a. Maroon, X. Liu, and D. S. Battisti (2013). “Contribution of ocean overturning circulation to tropical rainfall peak in the Northern Hemisphere”. In: *Nat. Geosci.* 6.11, pp. 940–944. doi: 10.1038/ngeo1987.
- Gadgil, S. and K. Kumar (2006). “The Asian monsoon - agriculture and economy”. In: *The Asian Monsoon*. Ed. by B. Wang. Chichester, UK: Praxis Publishing Ltd. Chap. 18, pp. 651–683.
- Gadgil, S. (2003). “The Indian monsoon and its variability”. In: *Annu. Rev. Earth Planet. Sci.* 31.1, pp. 429–467. doi: 10.1146/annurev.earth.31.100901.141251.
- Gautam, R., N. C. Hsu, K.-M. Lau, and M. Kafatos (2009). “Aerosol and rainfall variability over the Indian monsoon region: distributions, trends and coupling”. In: *Ann. Geophys.* 27.9, pp. 3691–3703. doi: 10.5194/angeo-27-3691-2009.

- Gill, A. E. (1980). "Some simple solutions for heat-induced tropical circulation". In: *Q. J. R. Meteorol. Soc.* 106.449, pp. 447–462. DOI: 10.1002/qj.49710644905.
- Goswami, B. N. (2005). "ENSO control on the south Asian monsoon through the length of the rainy season". In: *Geophys. Res. Lett.* 32, pp. 2005–2007. DOI: 10.1029/2005GL023216.
- Goswami, B. N., V. Krishnamurthy, and H. Annamalai (1999). "A broad-scale circulation index for the interannual variability of the Indian summer monsoon". In: *Q. J. R. Meteorol. Soc.* 125.554, pp. 611–633. DOI: 10.1002/qj.49712555412.
- Goswami, B. N., V. Venugopal, D. Sengupta, M. S. Madhusoodanan, and P. K. Xavier (2006a). "Increasing trend of extreme rain events over India in a warming environment." In: *Science* 314.5804, pp. 1442–1445. DOI: 10.1126/science.1132027.
- Goswami, B. N., G. Wu, and T. Yasunari (2006b). "The annual cycle, intraseasonal oscillations, and roadblock to seasonal predictability of the Asian summer monsoon". In: *J. Clim.* 19, pp. 5078–5099.
- Hahn, D. G. and J. Shukla (1976). "An Apparent Relationship between Eurasian Snow Cover and Indian Monsoon Rainfall". In: *J. Atmos. Sci.* 33, pp. 2461–2462. DOI: 10.1175/1520-0469(1976)033<2461:AARBES>2.0.CO;2.
- Harris, I., P. D. Jones, T. J. Osborn, and D. H. Lister (2014). "Updated high-resolution grids of monthly climatic observations - the CRU TS3.10 Dataset". In: *Int. J. Climatol.* 34.3, pp. 623–642.
- Heaviside, C. and A. Czaja (2013). "Deconstructing the Hadley cell heat transport". In: *Q. J. R. Meteorol. Soc.* 139.677, pp. 2181–2189. DOI: 10.1002/qj.2085.
- Held, I. M. and A. Y. Hou (1980). "Nonlinear axially symmetric circulations in a nearly inviscid atmosphere". In: *J. Atmos. Sci.* 37.3, pp. 515–533.
- Held, I. M. (2001). "The Partitioning of the Poleward Energy Transport between the Tropical Ocean and Atmosphere". In: *J. Atmos. Sci.* 58.8, pp. 943–948. DOI: 10.1175/1520-0469(2001)058<0943:TPOTPE>2.0.CO;2.
- Held, I. M. and B. J. Soden (2006). "Robust Responses of the Hydrological Cycle to Global Warming". In: *J. Clim.* 19.21, pp. 5686–5699. DOI: 10.1175/JCLI3990.1.
- Hendon, H. H., E.-P. Lim, and H. Nguyen (2014). "Seasonal Variations of Subtropical Precipitation Associated with the Southern Annular Mode". In: *J. Clim.* 27.9, pp. 3446–3460. DOI: 10.1175/JCLI-D-13-00550.1.
- Hoskins, B. and M. Rodwell (1995). "A model of the Asian summer monsoon. Part I: The global scale". In: *J. Atmos. Sci.* 52.9, pp. 1329–1340. DOI: [http://dx.doi.org/10.1175/1520-0469\(1995\)052<1329:AMOTAS>2.0.CO;2](http://dx.doi.org/10.1175/1520-0469(1995)052<1329:AMOTAS>2.0.CO;2).

- Hsu, P.-C., T. Li, H. Murakami, and A. Kitoh (2013). “Future change of the global monsoon revealed from 19 CMIP5 models”. In: *J. Geophys. Res. Atmos.* 118.3, pp. 1247–1260. doi: 10.1002/jgrd.50145.
- Huang, B., V. F. Banzon, E. Freeman, J. Lawrimore, W. Liu, T. C. Peterson, T. M. Smith, P. W. Thorne, S. D. Woodruff, and H.-M. Zhang (2015). “Extended Reconstructed Sea Surface Temperature Version 4 (ERSST.v4). Part I: Upgrades and Intercomparisons”. In: *J. Clim.* 28.3, pp. 911–930. doi: 10.1175/JCLI-D-14-00006.1.
- Huffman, G. J., D. T. Bolvin, and R. F. Adler (2016). *GPCP Version 1.2 One-Degree Daily Precipitation Data Set*. Boulder, Colorado. doi: <http://dx.doi.org/10.5065/D6D50K46>. Accessed 24 May 2016.
- Huffman, G. J., R. F. Adler, M. M. Morrissey, D. T. Bolvin, S. Curtis, R. Joyce, B. McGavock, and J. Susskind (2001). “Global Precipitation at One-Degree Daily Resolution from Multisatellite Observations”. In: *J. Hydrometeorol.* 2.1, pp. 36–50. doi: 10.1175/1525-7541(2001)002<0036:GPAODD>2.0.CO;2.
- Huffman, G. J., D. T. Bolvin, E. J. Nelkin, D. B. Wolff, R. F. Adler, G. Gu, Y. Hong, K. P. Bowman, and E. F. Stocker (2007). “The TRMM Multisatellite Precipitation Analysis (TMPA): Quasi-Global, Multiyear, Combined-Sensor Precipitation Estimates at Fine Scales”. In: *J. Hydrometeorol.* 8, pp. 38–55. doi: 10.1175/JHM560.1.
- Hung, C.-W. and H.-H. Hsu (2008). “The First Transition of the Asian Summer Monsoon, Intraseasonal Oscillation, and Taiwan Mei-yu”. In: *J. Clim.* 21, pp. 1552–1568. doi: 10.1175/2007JCLI1457.1.
- Hurley, J. V. and W. R. Boos (2013). “Interannual variability of monsoon precipitation and subcloud equivalent potential temperature”. In: *J. Clim.* 26, pp. 9507–9527.
- Kalnay, E., M. Kanamitsu, R. Kistler, W. Collins, D. Deaven, L. Gandin, M. Iredell, S. Saha, G. White, J. Woollen, Y. Zhu, M. Chelliah, W. Ebisuzaki, W. Higgins, J. Janowiak, K. C. Mo, C. Ropelewski, J. Wang, A. Leetmaa, R. Reynolds, R. Jenne, and D. Joseph (1996). “The NCEP/NCAR 40-Year Reanalysis Project”. In: *Bull. Am. Meteorol. Soc.* 77.3, pp. 437–471.
- Kanamitsu, M., W. Ebisuzaki, J. Woollen, S.-K. Yang, J. J. Hnilo, M. Fiorino, and G. L. Potter (2002). “NCEP-DOE AMIP-II Reanalysis (R-2)”. In: *Bull. Am. Meteorol. Soc.* 83.11, pp. 1631–1643. doi: 10.1175/BAMS-83-11-1631.
- Kang, S. M., D. M. W. Frierson, and I. M. Held (2009). “The Tropical Response to Extratropical Thermal Forcing in an Idealized GCM: The Importance of Radiative Feedbacks and Convective Parameterization”. In: *J. Atmos. Sci.* 66.9, pp. 2812–2827. doi: 10.1175/2009JAS2924.1.

- Kang, S. M., I. M. Held, D. M. W. Frierson, and M. Zhao (2008). “The Response of the ITCZ to Extratropical Thermal Forcing: Idealized Slab-Ocean Experiments with a GCM”. In: *J. Clim.* 21.14, pp. 3521–3532. DOI: 10.1175/2007JCLI2146.1.
- Kang, S. M., I. M. Held, and S.-P. Xie (2014). “Contrasting the tropical responses to zonally asymmetric extratropical and tropical thermal forcing”. In: *Clim. Dyn.* 42.7-8, pp. 2033–2043. DOI: 10.1007/s00382-013-1863-0.
- Krishnakumar, V. and K.-M. Lau (1997). “Symmetric instability of monsoon flows”. In: *Tellus A* 49, pp. 228–245. DOI: 10.1034/j.1600-0870.1997.t01-1-00005.x.
- Kumar, K. K., B. Rajagopalan, and M. A. Cane (1999). “On the Weakening Relationship Between the Indian Monsoon and ENSO”. In: *Science* 284.5423, pp. 2156–2159. DOI: 10.1126/science.284.5423.2156.
- Kumar, K. K., B. Rajagopalan, M. Hoerling, G. Bates, and M. Cane (2006). “Unraveling the mystery of Indian monsoon failure during El Niño.” In: *Science* 314.5796, pp. 115–9. DOI: 10.1126/science.1131152.
- Lee, S. and H.-k. Kim (2003). “The Dynamical Relationship between Subtropical and Eddy-Driven Jets”. In: *J. Atmos. Sci.* 60.12, pp. 1490–1503. DOI: 10.1175/1520-0469(2003)060<1490:TDRBSA>2.0.CO;2.
- Li, C. and M. Yanai (1996). “The onset and interannual variability of the Asian summer monsoon in relation to land-sea thermal contrast”. In: *J. Clim.* 9.2, pp. 358–375. DOI: 10.1175/1520-0442(1996)009<0358:TOAIVO>2.0.CO;2.
- Li, C. and J. Pan (2006). “Atmospheric Circulation Characteristics Associated with the Onset of Asian Summer Monsoon”. In: *Adv. Atmos. Sci.* 23.6, pp. 925–939.
- Lindzen, R. S. and A. Y. Hou (1988). “Hadley circulations for zonally averaged heating centered off the equator”. In: *J. Atmos. Sci.* 45.17, pp. 2416–2427. DOI: 10.1175/1520-0469(1988)045<2416:HCFZAH>2.0.CO;2.
- Meehl, G. A. (1987). “The annual cycle and interannual variability in the tropical Pacific and Indian-Ocean regions”. In: *Mon. Weather Rev.* 115, pp. 27–50. DOI: [http://dx.doi.org/10.1175/1520-0493\(1987\)115<0027:TACAIV>2.0.CO;2](http://dx.doi.org/10.1175/1520-0493(1987)115<0027:TACAIV>2.0.CO;2).
- Meehl, G. (1994). “Influence of the land surface in the Asian summer monsoon: External conditions versus internal feedbacks”. In: *J. Clim.* 7.7, pp. 1033–1049.
- Merlis, T. M., T. Schneider, S. Bordoni, and I. Eisenman (2013). “The Tropical Precipitation Response to Orbital Precession”. In: *J. Clim.* 26.6, pp. 2010–2021. DOI: 10.1175/JCLI-D-12-00186.1.
- Minoura, D., R. Kawamura, and T. Matsuura (2003). “A Mechanism of the Onset of the South Asian Summer Monsoon”. In: *J. Meteorol. Soc. Japan* 81.3, pp. 563–580. DOI: 10.2151/jmsj.81.563.

- Molnar, P., W. R. Boos, and D. S. Battisti (2010). “Orographic Controls on Climate and Paleoclimate of Asia: Thermal and Mechanical Roles for the Tibetan Plateau”. In: *Annu. Rev. Earth Planet. Sci.* 38.1, pp. 77–102. doi: 10.1146/annurev-earth-040809-152456.
- Naidu, C. V., K. Durgalakshmi, K. Muni Krishna, S. Ramalingeswara Rao, G. C. Satyanarayana, P. Lakshminarayana, and L. Malleswara Rao (2009). “Is summer monsoon rainfall decreasing over India in the global warming era?” In: *J. Geophys. Res.* 114, p. D24108. doi: 10.1029/2008JD011288.
- Neelin, J. (2007). “Moist dynamics of tropical convection zones in monsoons, teleconnections and global warming”. In: *Glob. Circ. Atmos.* Ed. by T. Schneider and A. H. Sobel. Princeton University Press, pp. 267–301.
- Nguyen, H., A. Evans, C. Lucas, I. Smith, and B. Timbal (2013). “The Hadley Circulation in Reanalyses: Climatology, Variability, and Change”. In: *J. Clim.* 26.10, pp. 3357–3376. doi: 10.1175/JCLI-D-12-00224.1.
- Nie, J., W. R. Boos, and Z. Kuang (2010). “Observational Evaluation of a Convective Quasi-Equilibrium View of Monsoons”. In: *J. Clim.* 23.16, pp. 4416–4428. doi: 10.1175/2010JCLI3505.1.
- Noska, R. and V. Misra (2016). “Characterizing the onset and demise of the Indian summer monsoon”. In: *Geophys. Res. Lett.* 43.9, pp. 4547–4554. doi: 10.1002/2016GL068409.
- Pant, G. B. and S. B. Parthasarathy (1981). “Some aspects of an association between the southern oscillation and indian summer monsoon”. In: *Arch. Meteor. Geophys. Bioklim. Ser. B* 29, pp. 245–262.
- Parthasarathy, B., R. Kumar, and D. Kothawale (1992). “Indian summer monsoon rainfall indices, 1871-1990”. In: *Meteorol. Mag.* 121, pp. 174–186.
- Parthasarathy, B., A. Munot, and D. Kothawale (1995). *Monthly and seasonal rainfall series for All-India homogeneous regions and meteorological subdivisions: 1871-1994. Contributions from Indian Institute of Tropical Meteorology, Research Report RR-065, Aug. 1995.* Tech. rep. Pune 411 008 INDIA.
- Peixoto, J. P. and A. H. Oort (1992). *Physics of Climate.* American Institute of Physics, p. 520.
- Plumb, R. A. and A. Y. Hou (1992). “The response of a zonally symmetric atmosphere to subtropical thermal forcing: Threshold behavior”. In: *J. Atmos. Sci.* 49.19, pp. 1790–1799. doi: 10.1175/1520-0469(1992)049<1790:TROAZS>2.0.CO;2.
- Privé, N. C. and R. A. Plumb (2007). “Monsoon Dynamics with Interactive Forcing. Part I: Axisymmetric Studies”. In: *J. Atmos. Sci.* 64.5, pp. 1417–1430. doi: 10.1175/JAS3916.1.

- Raju, P. V. S., U. C. Mohanty, and R. Bhatla (2007). "Interannual variability of onset of the summer monsoon over India and its prediction". In: *Nat. Hazards* 42.2, pp. 287–300. DOI: 10.1007/s11069-006-9089-7.
- Ramage, C. (1971). *Monsoon Meteorology*. Vol. 15. San Diego, Calif.: Academic Press, 296 pp. DOI: 10.1016/S0074-6142(08)60596-3.
- Ramanathan, V., C. Chung, D. Kim, T. Bettge, L. Buja, J. T. Kiehl, W. M. Washington, Q. Fu, D. R. Sikka, and M. Wild (2005). "Atmospheric brown clouds: impacts on South Asian climate and hydrological cycle." In: *Proc. Natl. Acad. Sci. U. S. A.* 102, pp. 5326–5333. DOI: 10.1073/pnas.0500656102.
- Randel, W. J. and I. M. Held (1991). "Phase Speed Spectra of Transient Eddy Fluxes and Critical Layer Absorption". In: *J. Atmos. Sci.* 48.5, pp. 688–697.
- Rao, R. R., R. L. Molinari, and J. F. Festa (1989). "Evolution of the climatological near-surface thermal structure of the tropical Indian Ocean: 1. Description of mean monthly mixed layer depth, and sea surface temperature, surface current, and surface meteorological fields". In: *J. Geophys. Res.* 94.C8, p. 10801. DOI: 10.1029/JC094iC08p10801.
- Rao, Y. P. (1976). *South West Monsoon*. Pune, India: India Meteorological Department, p. 376.
- Rasmusson, E. M. and T. H. Carpenter (1982). "Variations in tropical sea surface temperature and surface wind fields associated with the Southern Oscillation/El Niño". In: *Mon. Weather Rev.* 110, pp. 354–384. DOI: 10.1175/1520-0493(1982)110<0354:VITSST>2.0.CO;2.
- Rienecker, M. M., M. J. Suarez, R. Gelaro, R. Todling, J. Bacmeister, E. Liu, M. G. Bosilovich, S. D. Schubert, L. Takacs, G.-K. Kim, S. Bloom, J. Chen, D. Collins, A. Conaty, A. da Silva, W. Gu, J. Joiner, R. D. Koster, R. Lucchesi, A. Molod, T. Owens, S. Pawson, P. Pegion, C. R. Redder, R. Reichle, F. R. Robertson, A. G. Ruddick, M. Sienkiewicz, and J. Woollen (2011). "MERRA: NASA's Modern-Era Retrospective Analysis for Research and Applications". In: *J. Clim.* 24.14, pp. 3624–3648. DOI: 10.1175/JCLI-D-11-00015.1.
- Saji, N. H., B. N. Goswami, P. N. Vinayachandran, and T. Yamagata (1999). "A dipole mode in the tropical Indian Ocean." In: *Nature* 401.6751, pp. 360–363. DOI: 10.1038/43854.
- Schneider, E. and R. Lindzen (1977). "Axially Symmetric Steady-State Models of the Basic State for Instability and Climate Studies. Part I. Linearized Calculations". In: *J. Atmos. Sci.* 34, pp. 263–279.
- Schneider, T., T. Bischoff, and G. H. Haug (2014). "Migrations and dynamics of the Intertropical Convergence Zone". In: *Nature* 513, pp. 45–53. DOI: 10.1038/nature13636.

- Schneider, T. (2006). “The General Circulation of the Atmosphere”. In: *Annu. Rev. Earth Planet. Sci.* 34.1, pp. 655–688. DOI: 10.1146/annurev.earth.34.031405.125144.
- Schneider, T. and S. Bordoni (2008). “Eddy-Mediated Regime Transitions in the Seasonal Cycle of a Hadley Circulation and Implications for Monsoon Dynamics”. In: *J. Atmos. Sci.* 65.3, pp. 915–934. DOI: 10.1175/2007JAS2415.1.
- Shaw, T. A. (2014). “On the Role of Planetary-Scale Waves in the Abrupt Seasonal Transition of the Northern Hemisphere General Circulation”. In: *J. Atmos. Sci.* 71.5, pp. 1724–1746. DOI: 10.1175/JAS-D-13-0137.1.
- Shuen, X., M. Kimoto, and A. Sumi (1998). “Role of Land Surface Processes Associated with Interannual Variability of Broad-scale Asian Summer Monsoon as Simulated by the CCSR/NIES AGCM”. In: *J. Meteorol. Soc. Japan* 76.2, pp. 217–236.
- Shukla, J. and D. A. Mooley (1987). “Empirical prediction of the summer monsoon rainfall over India”. In: *Mon. Weather Rev.* 115, pp. 695–703.
- Simpson, G. (1921). “The south-west monsoon”. In: *Q. J. R. Meteorol. Soc.* 199.17, pp. 150–173.
- Sun, Y., Y. Ding, and A. Dai (2010). “Changing links between South Asian summer monsoon circulation and tropospheric land-sea thermal contrasts under a warming scenario”. In: *Geophys. Res. Lett.* 37, p. L02704. DOI: 10.1029/2009GL041662.
- Takacs, L. L., M. Suarez, and R. Todling (2015). “Maintaining Atmospheric Mass and Water Balance Within Reanalysis”. In: *NASA/TM–2014-104606 Tech. Rep. Ser. Glob. Model. Data Assim.* 37. March.
- Taniguchi, K. and T. Koike (2006). “Comparison of definitions of Indian summer monsoon onset: Better representation of rapid transitions of atmospheric conditions”. In: *Geophys. Res. Lett.* 33.2, p. L02709. DOI: 10.1029/2005GL024526.
- Thompson, D. W. J. and J. M. Wallace (2000). “Annular Modes in the Extratropical Circulation. Part I: Month-to-Month Variability”. In: *J. Clim.* 13.5, pp. 1000–1016. DOI: 10.1175/1520-0442(2000)013<1000:AMITEC>2.0.CO;2.
- Tomas, R. A. and P. J. Webster (1997). “The role of inertial instability in determining the location and strength of near-equatorial convection”. In: *Q. J. R. Meteorol. Soc.* 123.542, pp. 1445–1482. DOI: 10.1002/qj.49712354202.
- Trenberth, K. E., J. Hurrell, and D. P. Stepaniak (2005). “The Asian monsoon: Global perspectives”. In: *Asian Monsoon*. Ed. by B. Wang. Chichester, UK: Praxis Publishing Ltd. Chap. 2, pp. 67–87.
- Trenberth, K. E. (1997a). “The Definition of El Niño”. In: *Bull. Am. Meteorol. Soc.* 78.12, pp. 2771–2777.

- Trenberth, K. E. (1997b). “Using Atmospheric Budgets as a Constraint on Surface Fluxes”. In: *J. Clim.* 10.11, pp. 2796–2809. DOI: 10.1175/1520-0442(1997)010<2796:UABAAC>2.0.CO;2.
- Turner, A. G. and H. Annamalai (2012). “Climate change and the South Asian summer monsoon”. In: *Nat. Clim. Chang.* 2.8, pp. 587–595. DOI: 10.1038/nclimate1495.
- Uppala, S. M., P. W. Kallberg, A. J. Simmons, U. Andrae, V. D. C. Bechtold, M. Fiorino, J. K. Gibson, J. Haseler, A. Hernandez, G. A. Kelly, X. Li, K. Onogi, S. Saarinen, N. Sokka, R. P. Allan, E. Andersson, K. Arpe, M. A. Balmaseda, A. C. M. Beljaars, L. V. D. Berg, J. Bidlot, N. Bormann, S. Caires, F. Chevallier, A. Dethof, M. Dragosavac, M. Fisher, M. Fuentes, S. Hagemann, E. Hólm, B. J. Hoskins, L. Isaksen, P. A. E. M. Janssen, R. Jenne, A. P. McNally, J.-F. Mahfouf, J.-J. Morcrette, N. A. Rayner, R. W. Saunders, P. Simon, A. Sterl, K. E. Trenberth, A. Untch, D. Vasiljevic, P. Viterbo, and J. Woollen (2005). “The ERA-40 re-analysis”. In: *Q. J. R. Meteorol. Soc.* 131.612, pp. 2961–3012. DOI: 10.1256/qj.04.176.
- Walker, C. C. and T. Schneider (2006). “Eddy Influences on Hadley Circulations: Simulations with an Idealized GCM”. In: *J. Atmos. Sci.* 63.12, pp. 3333–3350. DOI: 10.1175/JAS3821.1.
- Walker, J. M. and S. Bordoni (2016). “Onset and withdrawal of the large-scale South Asian monsoon: A dynamical definition using change point detection”. In: *Geophys. Res. Lett.* 43. DOI: 10.1002/2016GL071026.
- Walker, J. M., S. Bordoni, and T. Schneider (2015). “Interannual Variability in the Large-Scale Dynamics of the South Asian Summer Monsoon”. In: *J. Clim.* 28.9, pp. 3731–3750. DOI: 10.1175/JCLI-D-14-00612.1.
- Wang, B., Q. Ding, and P. V. Joseph (2009). “Objective Definition of the Indian Summer Monsoon Onset”. In: *J. Clim.* 22.12, pp. 3303–3316. DOI: 10.1175/2008JCLI2675.1.
- Wang, B. and Z. Fan (1999). “Choice of South Asian Summer Monsoon Indices”. In: *Bull. Am. Meteorol. Soc.* 80.4, pp. 629–638. DOI: 10.1175/1520-0477(1999)080<0629:COSASM>2.0.CO;2.
- Wang, B. and LinHo (2002). “Rainy Season of the Asian-Pacific Summer Monsoon”. In: *J. Clim.* 15.4, pp. 386–398. DOI: 10.1175/1520-0442(2002)015<0386:RSOTAP>2.0.CO;2.
- Wang, B., J. Liu, H.-J. Kim, P. J. Webster, S.-Y. Yim, and B. Xiang (2013). “Northern Hemisphere summer monsoon intensified by mega-El Niño/southern oscillation and Atlantic multidecadal oscillation.” In: *Proc. Natl. Acad. Sci. U. S. A.* 110.14, pp. 5347–52. DOI: 10.1073/pnas.1219405110.

- Wang, B., R. Wu, and K.-M. Lau (2001). “Interannual Variability of the Asian Summer Monsoon: Contrasts between the Indian and the Western North Pacific–East Asian Monsoons”. In: *J. Clim.* 14.20, pp. 4073–4090. DOI: 10.1175/1520-0442(2001)014<4073:IVOTAS>2.0.CO;2.
- Webster, P. J. (1972). “Response of the tropical atmosphere to local, steady forcing”. In: *Mon. Weather Rev.* 100.7, pp. 518–541.
- Webster, P. J., V. O. Magaña, T. N. Palmer, J. Shukla, R. A. Tomas, M. Yanai, and T. Yasunari (1998). “Monsoons: Processes, predictability, and the prospects for prediction”. In: *J. Geophys. Res.* 103.C7, pp. 14451–14510. DOI: 10.1029/97JC02719.
- Webster, P. J. and S. Yang (1992). “Monsoon and ENSO: Selectively Interactive Systems”. In: *Q. J. R. Meteorol. Soc.* 118.507, pp. 877–926. DOI: 10.1002/qj.49711850705.
- Webster, P. and J. Fasullo (2003). “MONSOON | Dynamical Theory”. In: *Encycl. Atmos. Sci.* Ed. by J. R. Holton. Oxford: Academic Press, pp. 1370–1386. DOI: <http://dx.doi.org/10.1016/B0-12-227090-8/00236-0>.
- Weickmann, K. M. and R. M. Chervin (1988). “The Observed and Simulated Atmospheric Seasonal Cycle. Part I: Global Wind Field Modes”. In: *J. Clim.* 1.3, pp. 265–289. DOI: 10.1175/1520-0442(1988)001<0265:TOASAS>2.0.CO;2.
- Wu, G. and Y. Zhang (1998). “Tibetan Plateau forcing and the timing of the monsoon onset over South Asia and the South China Sea”. In: *Mon. Weather Rev.* 126, pp. 913–927.
- Wu, R. and B. P. Kirtman (2003). “On the impacts of the Indian summer monsoon on ENSO in a coupled GCM”. In: *Q. J. R. Meteorol. Soc.* 129.595, pp. 3439–3468. DOI: 10.1256/qj.02.214.
- Xie, P. and P. A. Arkin (1997). “Global Precipitation : A 17-Year Monthly Analysis Based on Gauge Observations, Satellite Estimates, and Numerical Model Outputs”. In: *Bull. Amer. Meteor. Soc.* 78.11, pp. 2539–2558.
- Yang, W., R. Seager, and M. A. Cane (2013). “Zonal Momentum Balance in the Tropical Atmospheric Circulation during the Global Monsoon Mature Months”. In: *J. Atmos. Sci.* 70.2, pp. 583–599. DOI: 10.1175/JAS-D-12-0140.1.
- Yasunari, T. (1991). “The monsoon year - a new concept of the climatic year in the tropics”. In: *Bull. Am. Meteorol. Soc.* 72, pp. 1331–1338.
- Zuo, Z., S. Yang, R. Zhang, P. Jiang, L. Zhang, and F. Wang (2013). “Long-Term Variations of Broad-Scale Asian Summer Monsoon Circulation and Possible Causes”. In: *J. Clim.* 26.22, pp. 8947–8961. DOI: 10.1175/JCLI-D-12-00691.1.

*Appendix A*SIMULATION OF NITRATE, SULFATE, AND AMMONIUM
AEROSOLS OVER THE UNITED STATES

Walker, J. M., S. Philip, R. V. Martin, and J. H. Seinfeld (2012). “Simulation of nitrate, sulfate, and ammonium aerosols over the United States”. In: *Atmos. Chem. Phys.* 12.22, pp. 11213–11227. doi: 10.5194/acp-12-11213-2012.



Simulation of nitrate, sulfate, and ammonium aerosols over the United States

J. M. Walker¹, S. Philip³, R. V. Martin^{3,4}, and J. H. Seinfeld^{1,2}

¹Department of Environmental Science and Engineering, California Institute of Technology, Pasadena, California, USA

²Department of Chemical Engineering, California Institute of Technology, Pasadena, California, USA

³Department of Physics and Atmospheric Science, Dalhousie University, Halifax, Nova Scotia, Canada

⁴Harvard-Smithsonian Center for Astrophysics, Cambridge, Massachusetts, USA

Correspondence to: J. H. Seinfeld (seinfeld@caltech.edu)

Received: 19 July 2012 – Published in Atmos. Chem. Phys. Discuss.: 6 August 2012

Revised: 16 November 2012 – Accepted: 19 November 2012 – Published: 27 November 2012

Abstract. Atmospheric concentrations of inorganic gases and aerosols (nitrate, sulfate, and ammonium) are simulated for 2009 over the United States using the chemical transport model GEOS-Chem. Predicted aerosol concentrations are compared with surface-level measurement data from the Interagency Monitoring of Protected Visual Environments (IMPROVE), the Clean Air Status and Trends Network (CASTNET), and the California Air Resources Board (CARB). Sulfate predictions nationwide are in reasonably good agreement with observations, while nitrate and ammonium are over-predicted in the East and Midwest, but under-predicted in California, where observed concentrations are the highest in the country. Over-prediction of nitrate in the East and Midwest is consistent with results of recent studies, which suggest that nighttime nitric acid formation by heterogeneous hydrolysis of N_2O_5 is over-predicted based on current values of the N_2O_5 uptake coefficient, γ , onto aerosols. After reducing the value of γ by a factor of 10, predicted nitrate levels in the US Midwest and East still remain higher than those measured, and over-prediction of nitrate in this region remains unexplained. Comparison of model predictions with satellite measurements of ammonia from the Tropospheric Emissions Spectrometer (TES) indicates that ammonia emissions in GEOS-Chem are underestimated in California and that the nationwide seasonality applied to ammonia emissions in GEOS-Chem does not represent California very well, particularly underestimating winter emissions. An ammonia sensitivity study indicates that GEOS-Chem simulation of nitrate is ammonia-limited in southern California and much of the state, suggesting that an underestimate of

ammonia emissions is likely the main cause for the under-prediction of nitrate aerosol in many areas of California. An approximate doubling of ammonia emissions is needed to reproduce observed nitrate concentrations in southern California and in other ammonia sensitive areas of California. However, even a tenfold increase in ammonia emissions yields predicted nitrate concentrations that are still biased low in the central valley of California. The under-prediction of nitrate aerosol in the central valley of California may arise in part from an under-prediction of both ammonia and nitric acid in this region. Since nitrate aerosols are particularly sensitive to mixed layer depths, owing to the gas-particle equilibrium, the nitrate under-prediction could also arise in part from a potential regional overestimate of GEOS-5 mixed layer depths in the central valley due to unresolved topography in this region.

1 Introduction

Nitrate (NO_3^-), sulfate (SO_4^{2-}) and ammonium (NH_4^+) are major constituents of atmospheric aerosols. These species are formed primarily from chemical reactions in the atmosphere involving the gas-phase precursors, nitrogen oxides (NO_x), sulfur dioxide (SO_2) and ammonia (NH_3). In this work, we use the global chemical transport model GEOS-Chem to simulate nitrate, sulfate and ammonium aerosols over the United States and we compare model predictions with measurement data to assess model performance. This work is motivated, in part, by previous studies (Pye et al.,

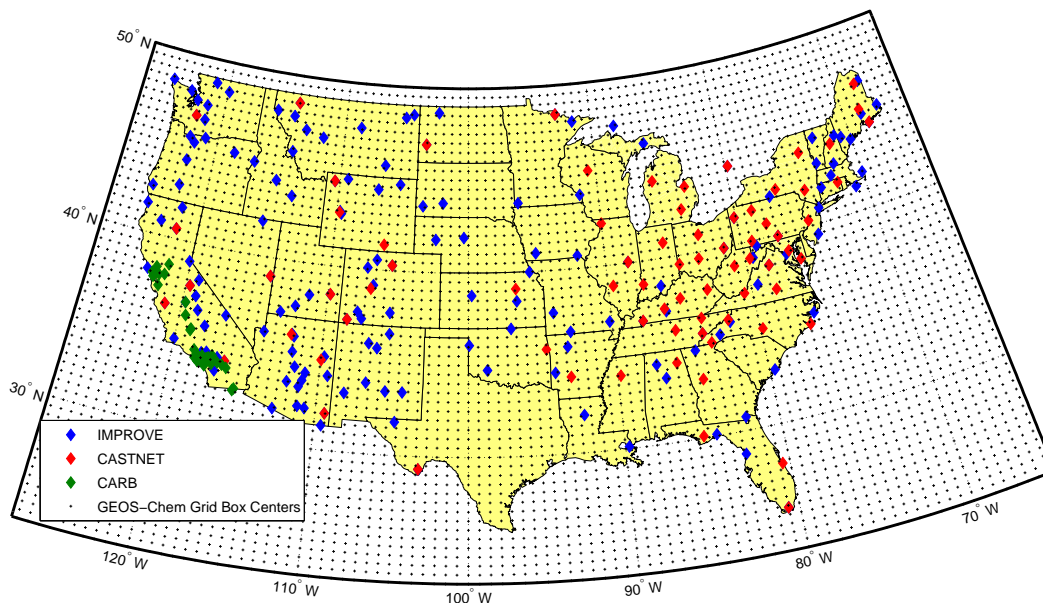


Fig. 1. Locations of IMPROVE, CASTNET, and CARB measurement sites, and GEOS-Chem grid box centers over the US.

2009; Bauer et al., 2007; Myhre et al., 2006) that indicated that observed high nitrate levels in California have not been simulated adequately by global chemical transport models. In a recent GEOS-Chem simulation over the US, Zhang et al. (2012) found that although predictions of the gas-phase precursor NO_x agreed well with satellite measurements, predicted HNO_3 and nitrate aerosol had strong positive biases throughout most of the country.

We note especially the study of Heald et al. (2012), completed at essentially the same time as the present work, which addresses a number of the same issues and reports results generally consistent with those presented here.

2 GEOS-Chem model

Atmospheric concentrations of aerosols and gas-phase species are simulated using the chemical transport model GEOS-Chem, version 9-01-02 (<http://acmg.seas.harvard.edu/geos/>). A nested version of the model (Chen et al., 2009; van Donkelaar et al., 2012; Zhang et al., 2012) is used, on a $1/2^\circ$ (latitude) by $2/3^\circ$ (longitude) horizontal grid over North America (Fig. 1), with 47 vertical levels, nested within a global parent grid at $2^\circ \times 2.5^\circ$ horizontal resolution. The calendar year 2009 is simulated, with a spin-up period of one year. The model is driven by Goddard Earth Observing System (GEOS-5) assimilated meteorological fields from NASA's Global Modeling and Assimilation Office (GMAO). Meteorological data include winds, temperature, humidity, cloud fraction, precipitation and other fields at a 6-h temporal resolution, as well as mixed layer depth and surface properties at a 3-h temporal resolution.

Data from the EPA National Emissions Inventory (NEI) 2005 on emissions of NO_x , SO_2 , NH_3 , CO and volatile organic compounds (VOCs) were scaled to the simulation year according to annual trends in the EPA Acid Rain Program (<http://ampd.epa.gov/ampd/>) and the NEI Air Pollutant Emissions Trends Data (<http://www.epa.gov/ttn/chief/trends/>). Additional NO_x and SO_2 emission sources include aircraft, biofuel, and biomass burning, as well as emissions of NO_x from lightning, soil and fertilizer, and sulfur emissions from ships, volcanoes and oceans (Park et al., 2004). Natural emission sources of ammonia include soil, vegetation and oceans, as described by Bouwman et al. (1997). Seasonal scaling factors, based on the EPA NEI 1999 emission inventory, were applied to emissions of all species except for NO_x , which was seasonally scaled based on the EPA Visibility Improvement-State and Tribal Association of the Southeast (VISTAS) emission inventory, and ammonia, which was seasonally scaled as in Park et al. (2004).

The model includes a detailed ozone- NO_x -VOC gas-phase chemical mechanism involving approximately 80 species and 300 chemical reactions (Bey et al., 2001). Sulfate formation pathways include gas-phase oxidation of SO_2 by OH and aqueous-phase oxidation of SO_2 by ozone and hydrogen peroxide. Gas-phase sulfur chemistry also includes oxidation of dimethyl sulfide (DMS) by OH to form SO_2 and methanesulfonic acid, and oxidation of DMS by NO_3 to form SO_2 (Park et al., 2004). The partitioning between gas-phase and aerosol-phase nitrate, sulfate and ammonium is computed using ISORROPIA II (Fountoukis and Nenes, 2007), a thermodynamic equilibrium model for the K^+ - Ca^{2+} - Mg^{2+} - NH_4^+ - Na^+ - SO_4^{2-} - NO_3^- - Cl^- - H_2O aerosol system, implemented within GEOS-Chem.

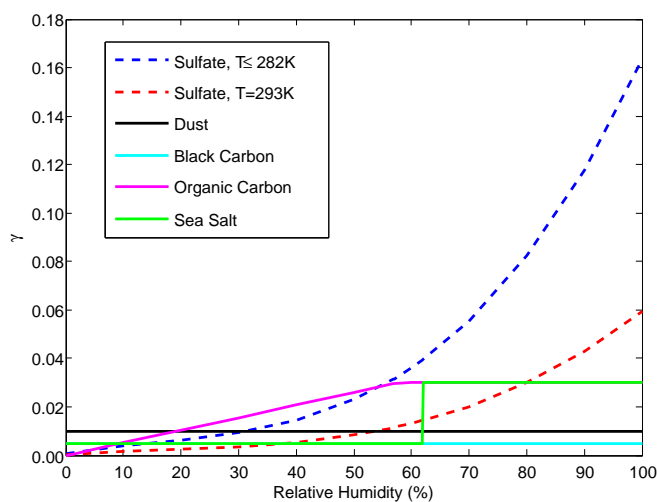
Table 1. Measurement datasets.

Dataset	Site locations	Sampling frequency	Species measured
IMPROVE	Remote/rural areas	24-h samples every 3rd day	Fine particulate (< 2.5 μm) sulfate and nitrate
CASTNET	Remote/rural areas	7-day samples	Total particulate (not size selective) sulfate, nitrate and ammonium, SO_2 (g), HNO_3 (g)
CARB	Mostly urban	24-h samples every 6 days	Fine particulate (< 2.5 μm) sulfate, nitrate, and ammonium; PM_{10} sulfate and nitrate

Removal of nitrate, sulfate, ammonium and related gas-phase species through wet deposition and dry deposition is simulated. The wet deposition scheme includes scavenging of aerosols and soluble gases in wet convective updrafts, in-cloud scavenging by cloud droplets or ice crystals, and below-cloud scavenging by precipitation (Liu et al., 2001). Dry deposition is simulated with a resistance in series scheme (Weeseley, 1989), with surface resistances for sulfate, nitrate and ammonium aerosols as described by Zhang et al. (2001).

Planetary boundary layer mixing is simulated using the TURBDAY full mixing scheme (Wu et al., 2007; Bey et al., 2001), in which vertical mixing is assumed to be instantaneous and uniform from the surface to the top of the mixed layer. The offline GEOS-5 meteorological fields used here display unrealistically low mixed layer depths at night, compared with observed mixed layer depths (Liu and Liang, 2010). This bias causes GEOS-5 driven GEOS-Chem simulations to predict an artificially large build up of aerosols at night and corresponding high biases in predicted daily and monthly average concentrations. To correct this issue, we have modified the model to define a minimum mechanical mixing depth, calculated based on the local friction velocity (Lin and McElroy, 2010; Koracin and Berkowicz, 1988; Heald et al., 2012); any GEOS-5 mixed layer depths below this value are set to the minimum mechanical mixing depth. This modification yields nighttime mixed layer depths that are more consistent with observations (Liu and Liang, 2010), and more realistic diurnal variations in predicted aerosol concentrations.

Zhang et al. (2012) suggest that nitrate concentrations may be over-predicted owing to an overestimate of nighttime nitric acid formation through heterogeneous N_2O_5 hydrolysis, $\text{N}_2\text{O}_5 + \text{H}_2\text{O} \rightarrow 2\text{HNO}_3$, as N_2O_5 concentrations build up due to the gas phase reaction of NO_2 with NO_3 . The rate of HNO_3 production by this reaction is expressed as $2k[\text{N}_2\text{O}_5]$, where $k = \gamma v_{\text{N}_2\text{O}_5} A_{\text{Aerosol}}/4$ and $v_{\text{N}_2\text{O}_5}$ is the mean molecular speed of N_2O_5 , A_{Aerosol} is the aerosol surface area per unit volume, and γ is the uptake coefficient, which describes the probability that an N_2O_5 molecule impacting an aerosol particle will undergo the irreversible heterogeneous hydrolysis reaction (Seinfeld and Pandis, 2006).

**Fig. 2.** Values of the N_2O_5 hydrolysis uptake coefficient γ in GEOS-Chem (Evans and Jacob, 2005).

Macintyre and Evans (2010) list the range of published values for γ as 10^{-4} to > 0.1 . They note that recent laboratory studies indicate lower values than previously considered, and suggest that the tropospheric value is likely in the range of 0.001 to 0.02. In a sensitivity analysis with GEOS-Chem, they find that within this range of values, the production of HNO_3 in the model is highly sensitive to the selected value of γ .

Figure 2 shows the values of γ used in the standard version of GEOS-Chem, for the various types of aerosols on which heterogeneous N_2O_5 hydrolysis is simulated (Evans and Jacob, 2005). The uptake coefficient on sulfate aerosol is determined in GEOS-Chem as a function of temperature and relative humidity. For temperatures of 282 K and below, γ at a given RH is assumed to be independent of temperature; for temperatures above 282 K, γ at a given RH decreases with increasing temperature. It is evident in Fig. 2 that the value of γ is above 0.02 for organic carbon and sea salt aerosol, and well above 0.02 for sulfate aerosol at higher humidities, exceeding 0.1 at lower temperatures and high RH. Based on the recommendations of Macintyre and Evans (2010), the values of γ in GEOS-Chem likely lead to an overestimate of

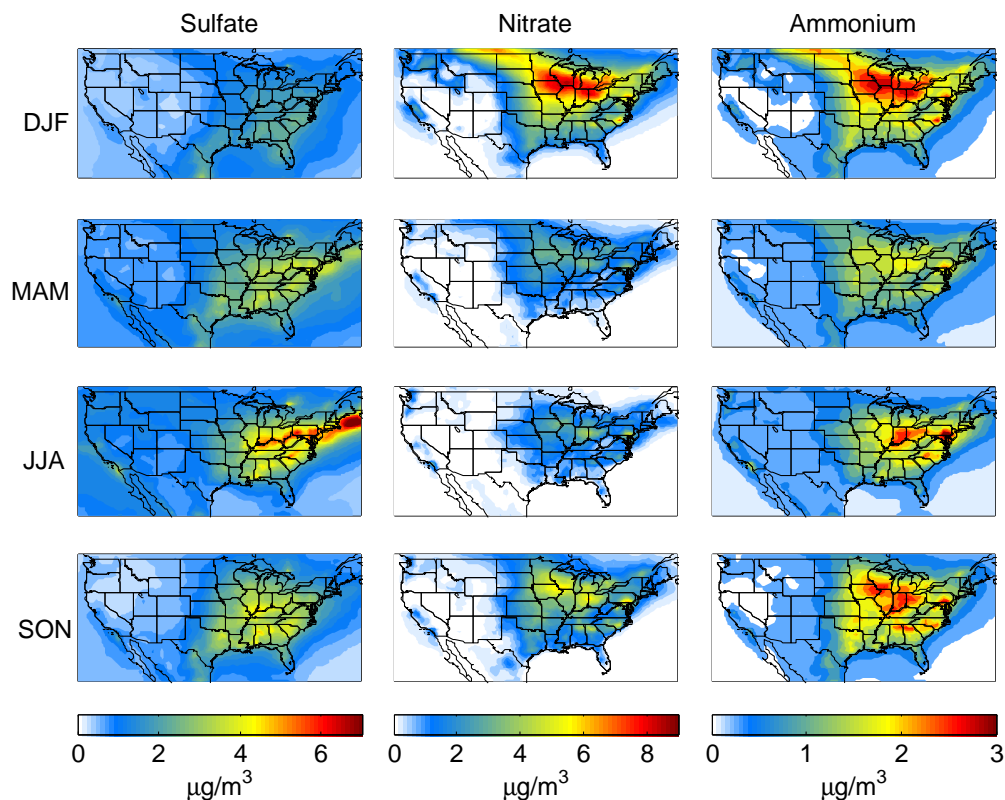


Fig. 3. Predicted concentrations of sulfate, nitrate, and ammonium aerosol for December-January-February (DJF), March-April-May (MAM), June-July-August (JJA) and September-October-November (SON), 2009.

nighttime HNO_3 formation, with a corresponding overestimate of nitrate aerosol production. Following the approach of Zhang et al. (2012), we have reduced γ by a factor of 10 in the present GEOS-Chem simulations, in order to simulate nighttime nitric acid formation using an uptake coefficient more consistent with Macintyre and Evans (2010).

3 Surface-level atmospheric data

GEOS-Chem simulations are compared to measured aerosol concentrations for 2009 from three data sources: the Interagency Monitoring of Protected Visual Environments (IMPROVE, <http://views.cira.colostate.edu/web/DataWizard/>), the Clean Air Status and Trends Network (CASTNET, <http://views.cira.colostate.edu/web/DataWizard/>) and the California Air Resources Board (CARB, <http://www.arb.ca.gov/aqmis2/aqmis2.php>). Table 1 summarizes the sampling frequency and measured species in each dataset. Locations of the measurement sites are shown in Fig. 1.

The CARB dataset includes sulfate and nitrate concentrations measured by both PM_{10} and $\text{PM}_{2.5}$ samplers. GEOS-Chem secondary aerosol predictions are not size resolved; however for the purposes of this study they can be assumed to be in the fine mode ($\text{PM}_{2.5}$), since the model does not in-

clude the formation of inorganic aerosols on coarse mode dust particles and although the model does include the formation of inorganic aerosols on coarse mode sea salt, these predicted concentrations comprise a negligible fraction of the total predicted aerosol concentrations over the continental US. Thus, the $\text{PM}_{2.5}$ nitrate and sulfate measurements were selected from the CARB dataset for comparison with model predictions.

The precision of IMPROVE secondary inorganic aerosol concentration measurements is estimated to be 4–6% (<http://vista.cira.colostate.edu/improve/Publications/OtherDocs/IMPROVEDataGuide/IMPROVEDataGuide.htm>). The precision of CASTNET concentration measurements is estimated to be approximately 3%, 8%, and 4% for sulfate, nitrate, and ammonium, respectively (Sickles II and Shadwick, 2002). Since the CARB $\text{PM}_{2.5}$ samplers are similar to the IMPROVE samplers, measurement precision for CARB observations is assumed to be similar to those in IMPROVE.

4 Results

Figure 3 shows the predicted seasonal average concentrations of nitrate, sulfate and ammonium aerosol at the surface level. Predicted annual concentrations are compared with measurements over the entire US in Fig. 4 and over California in

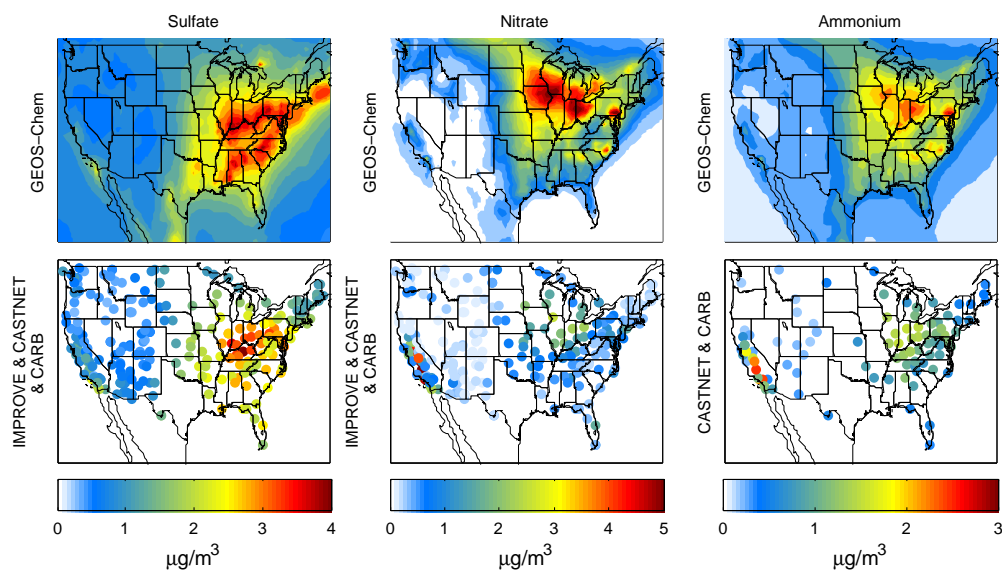


Fig. 4. Predicted 2009 annual mean aerosol concentrations compared with measured concentrations.

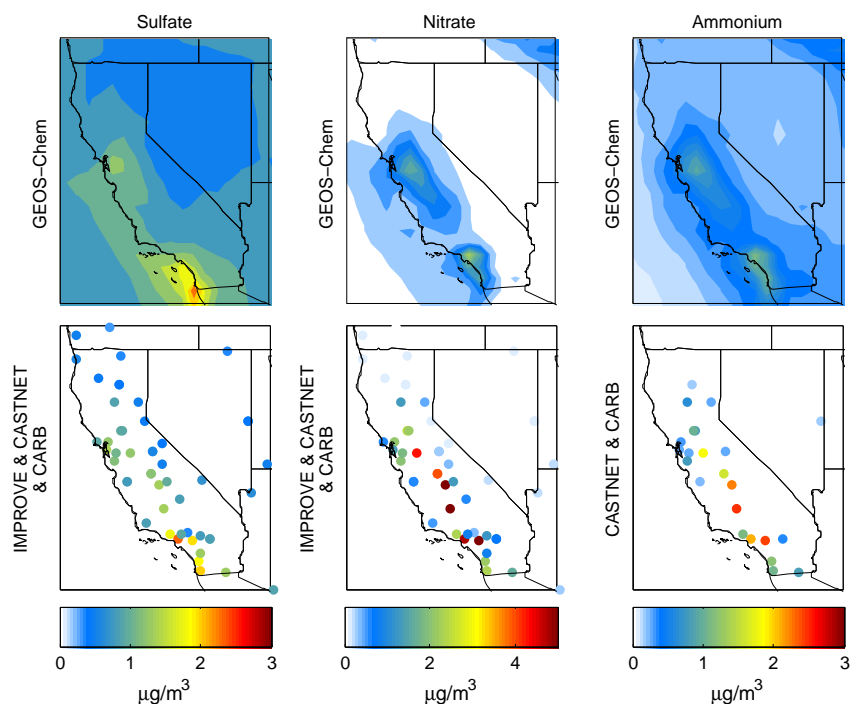


Fig. 5. Same as Fig. 4, but in detail for California.

Fig. 5. Scatter plots of predicted versus measured annual concentrations are shown in Fig. 6. The normalized mean biases (NMB) of predicted seasonal and annual concentrations are summarized in Table 2, where $NMB = (\sum(P_i - O_i) / \sum O_i) \times 100\%$, where P_i is the predicted and O_i the observed seasonal average concentration, and the summation is over all measurement sites.

Predicted annual sulfate concentrations are in reasonable agreement with IMPROVE, CASTNET and CARB measure-

ments (Fig. 6), with an NMB of +18% for the continental US excluding California and +3% for California. For California, the slope of the linear regression through the origin is actually less than 1, although the NMB is positive. Although this seems to be a contradiction, it reflects the fact that a straight line through the origin does not fit the scatter plot very well because there are just a few data points where the predicted concentration is substantially below the measured concentration, but there are a large number of data

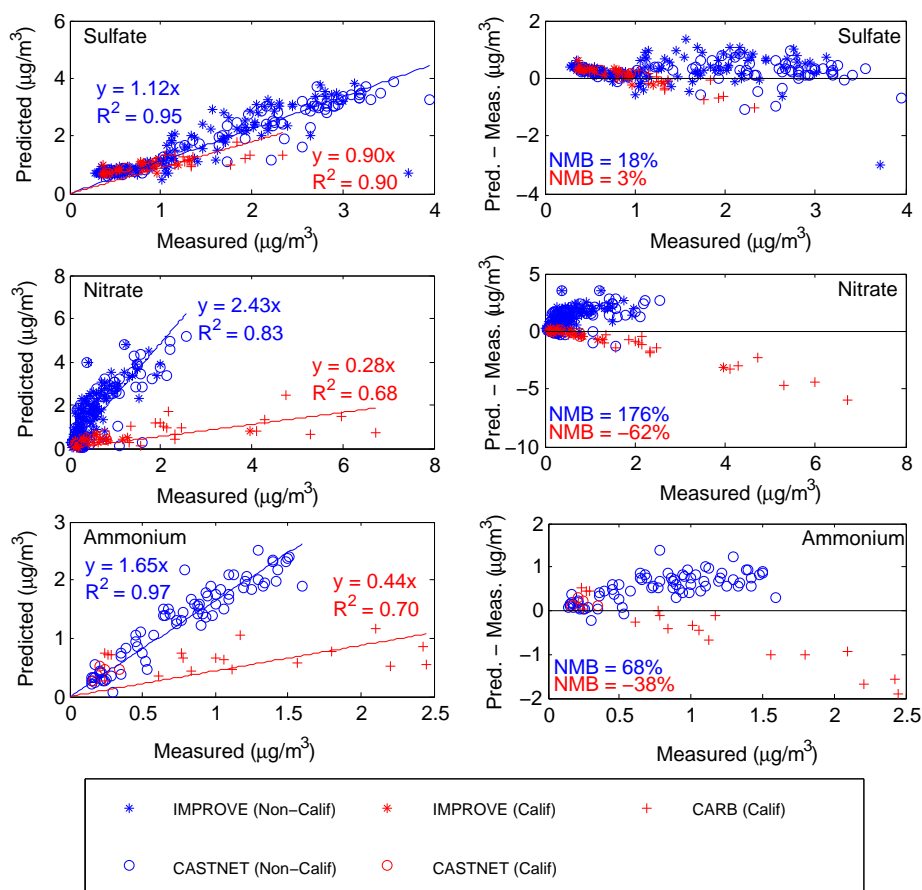


Fig. 6. Predicted versus measured annual mean concentrations (left panels) and difference between predicted and measured versus measured annual mean concentrations (right panels) for 2009. Each data point corresponds to an observed concentration at a measurement site along with the predicted concentration in the GEOS-Chem grid box containing the measurement site. Measured concentrations are IMPROVE ($\text{PM}_{2.5}$), CASTNET (TPM), and CARB ($\text{PM}_{2.5}$). Red regression lines and normalized mean biases (NMB) are for California sites only. Blue regression lines and NMB are for all sites excluding California. Coefficients of determination, R^2 , calculated for regression through the origin (Montgomery et al., 2006).

points for which the predicted concentrations are very close to or just slightly higher than those measured (top right panel of Fig. 6). There is substantial over-prediction, with NMB of +176% and +68%, respectively, in the predicted annual nitrate and ammonium annual concentrations over the US excluding California. The bias in nitrate predictions in the eastern and midwestern states has a significant seasonal variation, with the highest overprediction in the summer and autumn (Table 2). On the other hand, in California, there is a substantial under-prediction of annual nitrate and ammonium concentrations, with NMB of -62% and -38%, respectively, and the panels on the right side of Fig. 6 show that the magnitude of the negative bias increases as the measured concentration increases.

Figure 7 shows monthly mean predicted and measured inorganic aerosol concentrations at Bondville, IL, in the region of highest predicted nitrate concentrations in the Midwest, and at Fresno, CA and Riverside, CA. At all three sites, predicted sulfate concentrations agree reasonably well with

measured concentrations in magnitude and in the pattern of seasonal variation over the course of the year, with NMB values ranging from -36 to 9% (where the NMB at each site is calculated from the monthly mean predictions and observations at that site). Predicted nitrate and ammonium concentrations display similar patterns in comparison with observations at all three sites. At Bondville, nitrate and ammonium are over-predicted in all months except February and March, with NMB of +67% and +41% for nitrate and ammonium, respectively. At Riverside, nitrate and ammonium are under-predicted in all months, with NMB of -75% and -65%, respectively. At Fresno, nitrate is under-predicted in all months (NMB of -81%) and ammonium is under-predicted in all months except April, June and July (NMB of -64%). At Fresno, there is a very strong seasonal variation in observed nitrate which is not reflected in the model predictions; predicted January average nitrate concentration at Fresno is less than one tenth of the observed January average nitrate concentration.

Table 2. Normalized mean bias (%) of predicted 2009 seasonal concentrations relative to measurements (IMPROVE, CASTNET, CARB), for the base case GEOS-Chem simulation and the two ammonia sensitivity simulations ($2 \times \text{NH}_3$ and $10 \times \text{NH}_3$). Results for California are presented separately for the two regions shown in Fig. 11.

Aerosol species	Region	Simulation	DJF	MAM	JJA	SON	Annual
Sulfate	USA excluding California	Base Case	−3	+17	+23	+32	+18
		$2 \times \text{NH}_3$	−0.1	+18	+23	+34	+19
		$10 \times \text{NH}_3$	+4	+19	+229	+36	+21
	California (Region A)	Base Case	+67	−14	+11	−1	+6
		$2 \times \text{NH}_3$	+67	−14	+12	−1	+6
		$10 \times \text{NH}_3$	+69	−14	+12	−1	+6
	California (Region B)	Base Case	−27	−12	+27	−4	−2
		$2 \times \text{NH}_3$	−27	−12	+27	−4	−2
		$10 \times \text{NH}_3$	−26	−12	+26	−4	−2
Nitrate	USA excluding California	Base Case	+147	+85	+319	+296	+176
		$2 \times \text{NH}_3$	+248	+209	+654	+556	+334
		$10 \times \text{NH}_3$	+463	+539	+1415	+1095	+691
	California (Region A)	Base Case	−66	−65	−34	−50	−55
		$2 \times \text{NH}_3$	−35	−31	+26	−4	−13
		$10 \times \text{NH}_3$	+84	+91	+217	+144	+130
	California (Region B)	Base Case	−73	−47	−41	−71	−67
		$2 \times \text{NH}_3$	−62	−19	−7	−56	−51
		$10 \times \text{NH}_3$	−41	+54	+101	−16	−12
Ammonium	USA excluding California	Base Case	+63	+48	+59	+109	+68
		$2 \times \text{NH}_3$	+118	+93	+102	+184	+122
		$10 \times \text{NH}_3$	+232	+195	+179	+32	+229
	California (Region A)	Base Case	−59	−48	−12	−33	−38
		$2 \times \text{NH}_3$	−41	−29	+15	−7	−16
		$10 \times \text{NH}_3$	+23	+32	+94	+73	+54
	California (Region B)	Base Case	−68	+12	+51	−46	−38
		$2 \times \text{NH}_3$	−58	+36	+75	−33	−24
		$10 \times \text{NH}_3$	−40	+94	+140	−1	+8

Figure 8 shows the partitioning between monthly predicted aerosol and gas-phase nitrate and ammonia at the Fresno, Riverside, and Bondville sites. The annual average concentrations of total ammonia (gas phase ammonia plus aerosol ammonium, expressed as NH_3) and total nitrate (gas phase nitric acid plus aerosol nitrate, expressed as HNO_3) are similar at the Riverside and Bondville locations, with $7.9 \mu\text{g m}^{-3}$ total nitrate and $1.8 \mu\text{g m}^{-3}$ total ammonia at Riverside, compared to $8.9 \mu\text{g m}^{-3}$ total nitrate and $2.4 \mu\text{g m}^{-3}$ total ammonia at Bondville. Since Bondville is generally colder and more humid than Riverside, a larger fraction of total nitrate and ammonia exist in the aerosol phase at Bondville (Fig. 8). At Fresno, the annual average concentration of total ammonia is $2.3 \mu\text{g m}^{-3}$, similar to the other two sites, but the annual average total nitrate is only $4.0 \mu\text{g m}^{-3}$, approximately half the concentration at Riverside and Bondville.

4.1 Nitrate over-prediction in the Midwest/East

Over-prediction of nitrate and ammonium aerosol in the eastern and midwestern states in this study is consistent with re-

sults found by Zhang et al. (2012) and Heald et al. (2012). Nitrate aerosol is formed in thermodynamic equilibrium with gas-phase ammonia and nitric acid. The partitioning between the gas phase and aerosol phase nitrate is determined by the relative abundances of ammonia and nitric acid, as well as by the temperature and relative humidity, with equilibrium shifting towards the aerosol phase in colder and more humid conditions. If ammonia concentrations are low compared with the available nitric acid, then in thermodynamic equilibrium much of the HNO_3 will remain in the gas phase and nitrate aerosol formation is ammonia-limited. Conversely, if HNO_3 concentrations are low compared with the available ammonia, then nitrate aerosol formation is nitric acid-limited.

Zhang et al. (2012) suggest that GEOS-Chem may over-predict nitrate concentrations owing to an overestimate of nighttime nitric acid formation through heterogeneous N_2O_5 hydrolysis. However, the reduction of the N_2O_5 uptake coefficient, γ , by a factor of 10 in the current simulation did not reduce substantially the nitrate bias compared with another identical simulation (results not shown) using the standard GEOS-Chem values for γ : the NMB in predicted

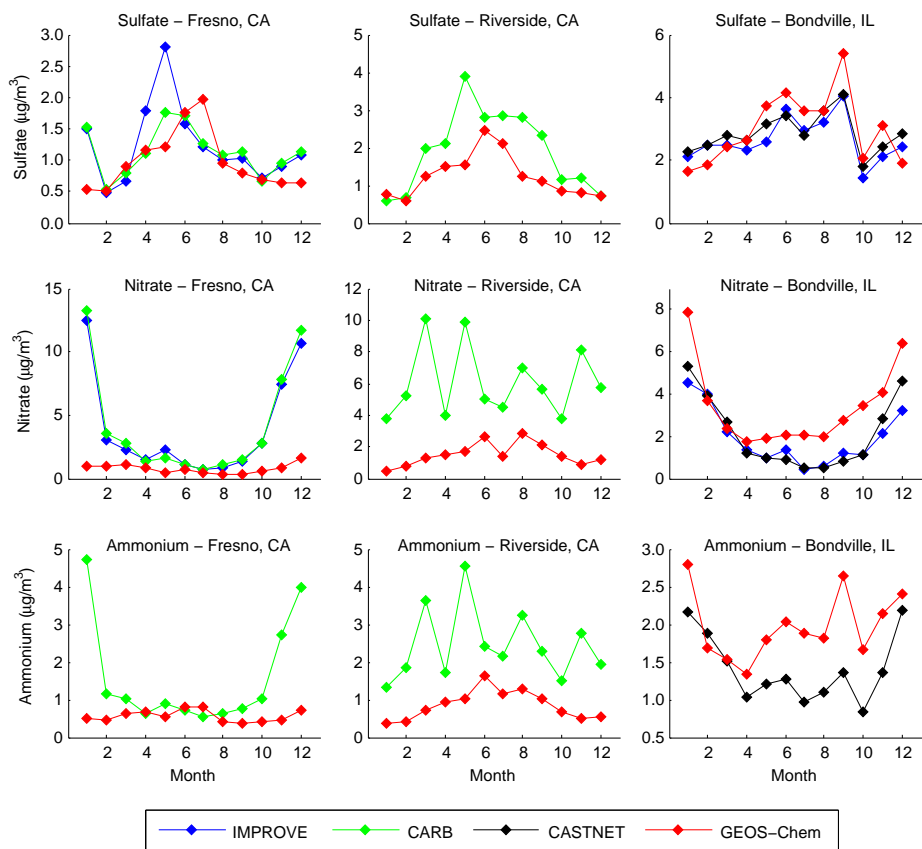


Fig. 7. 2009 monthly mean predicted and measured aerosol sulfate, nitrate, and ammonium concentrations at selected sites.

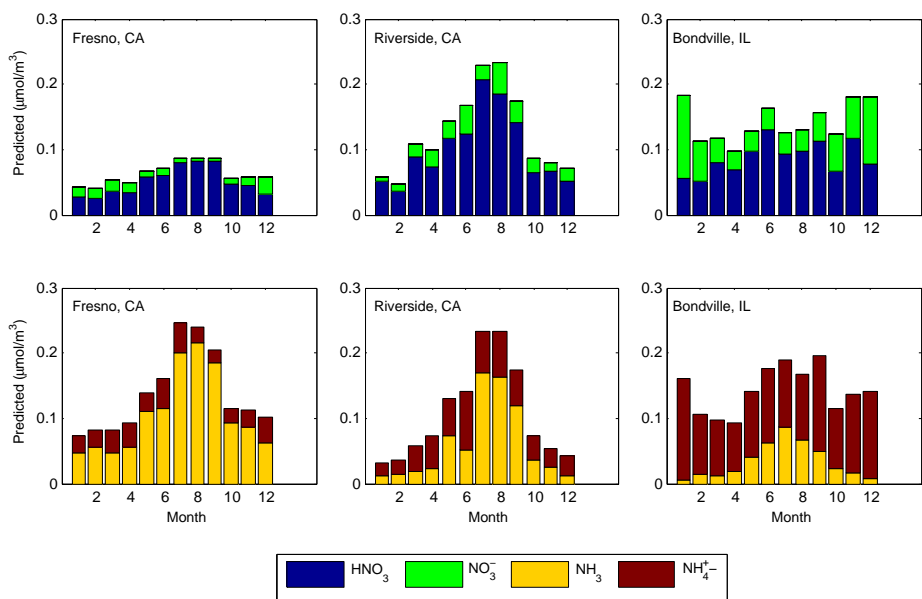


Fig. 8. Predicted 2009 monthly mean concentrations of gas-phase nitric acid, nitrate aerosol, gas-phase ammonia, and ammonium aerosol at selected sites. Note that gas-particle thermodynamic equilibrium is calculated to hold over each 20 min time step of the model. The monthly mean concentrations presented in this figure represent an average of the individual 20-min equilibria over all the hours of each month, and thus do not satisfy gas-particle equilibrium in the aggregate.

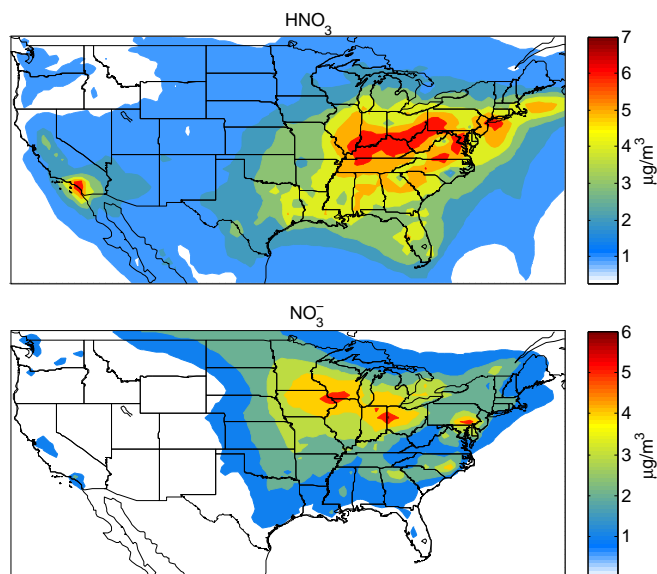


Fig. 9. Predicted 2009 annual mean concentrations of HNO_3 (upper panel) and nitrate aerosol (lower panel).

annual nitrate over the continental US (excluding California) is +176 % (Table 2) when γ is reduced by a factor of 10, compared with an NMB of +196 % when the standard γ values are used. These results suggest that an overestimate of heterogeneous N_2O_5 hydrolysis does not fully account for the nitrate bias.

Heald et al. (2012) found that GEOS-Chem simulation of nitrate aerosol over the midwestern and eastern states is nitric acid-limited and that the positive nitrate bias is likely linked with an overestimate of nitric acid concentrations: when they reduced nitric acid concentrations to 75 % of their simulated values in GEOS-Chem, this reduction corrected the bias in simulated nitrate and ammonium aerosol over the Midwest and East. In addition to the uncertainties in N_2O_5 hydrolysis, Heald et al. (2012) investigated other possible causes for an overestimate of nitric acid concentrations, including: uncertainties in daytime formation of HNO_3 arising from uncertainties in emissions of NO_x , concentrations of OH, or the rate of NO_2 oxidation by OH, and uncertainties in the dry deposition removal rates of nitric acid. They found that none of these uncertainties could fully account for the reduction in HNO_3 required to correct the nitrate bias. Overprediction of nitrate in the midwestern and eastern states remains to be explained.

4.2 Nitrate under-prediction in California

Figure 9 shows predicted annual HNO_3 and nitrate aerosol concentrations over the United States. Predicted concentrations of both HNO_3 and nitrate aerosol are high over the midwestern and eastern states. However, in southern California, predicted HNO_3 concentrations are among the highest in the country but this strong maximum is not reflected in the

predicted nitrate aerosol concentrations, suggesting that the nitrate simulation in this region may be ammonia-limited.

The large uncertainties in the ammonia emissions inventory and seasonal scaling factors used in GEOS-Chem could potentially result in a substantial underestimate of ammonia emissions and concentrations, along with a corresponding underestimate of nitrate aerosol in regions where simulated conditions are ammonia-limited. In their study of aircraft data from the CalNex 2010 experiment, Nowak et al. (2012) found that ammonia emissions from dairy facilities in Southern California have a significant effect on nitrate aerosol formation, shifting the NH_4NO_3 equilibrium towards the particle phase and resulting in higher nitrate aerosol concentrations downwind of the dairy facilities. They also compared the CalNex aircraft data to NEI 2005 and CARB-ARCTAS 08 (Huang et al., 2010) emissions inventories of ammonia in the South Coast Air Basin and found that both emissions inventories underestimate ammonia emissions relative to emissions estimates derived from the aircraft data. In the NEI 2005 inventory, which is used in GEOS-Chem, ammonia emissions from automobiles and dairy facilities in this region are 38 and 1 metric tonnes per day, respectively, compared to 56 and 11 tonnes per day, respectively, in the CARB-ARCTAS 08 inventory. Both these estimates are much lower than the emissions estimates derived by Nowak et al. (2012) from CalNex, of 38 to 86 tonnes per day from automobiles and 33 to 176 tonnes per day from dairy facilities.

We conducted a sensitivity analysis with GEOS-Chem, simulating the year 2009 with anthropogenic emissions of ammonia increased by a factor of two (“ $2 \times \text{NH}_3$ ” simulation) and by a factor of ten (“ $10 \times \text{NH}_3$ ” simulation). Figure 10 shows the ratios of the predicted annual nitrate concentrations in the ammonia sensitivity simulations to the base case predicted annual nitrate concentrations. In the upper panel, which displays the results for the $2 \times \text{NH}_3$ simulation, the ratio of predicted concentrations to base case predicted concentrations is close to two in the red areas, indicating that a doubling of ammonia emissions yields a doubling of predicted nitrate and thus the modeled nitrate is ammonia-limited in these areas. In the lower panel of Fig. 10, showing the results for the $10 \times \text{NH}_3$ simulation, the green, yellow and blue areas show the regions where predicted nitrate is sensitive to additional ammonia emissions beyond a factor of two increase, and the red areas show the regions where a tenfold increase in ammonia emissions yields a tenfold increase in predicted nitrate, indicating ammonia limitation over an order of magnitude increase in ammonia emissions.

Figure 11 summarizes the average ammonia sensitivity of predicted nitrate in California. The subset of California labeled “Region A” is an area of high ammonia sensitivity on average, in which predicted annual nitrate concentrations increase by 60 % or more above the base case when ammonia emissions are doubled in GEOS-Chem. The subset of California labeled “Region B” is an area of lower ammonia sensitivity on average, in which predicted annual nitrate

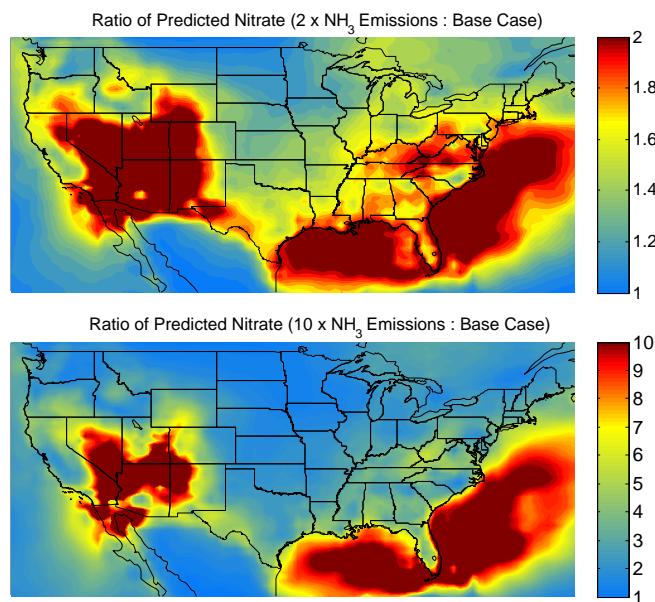


Fig. 10. Ratio of predicted 2009 annual nitrate concentrations in ammonia sensitivity simulations to base case predicted annual nitrate concentrations.

concentrations increase by less than 60 % when ammonia emissions are doubled. In each of these regions, the thermodynamic equilibrium between gas-phase and aerosol-phase nitrate is computed at each timestep and grid cell, so within Region A there will be some locations and timesteps where the ammonia sensitivity is low, and conversely for Region B. However, Fig. 11 shows that, on average, there are two distinct regions corresponding to the limiting factor (ammonia or nitric acid) in the simulation of nitrate in California.

Region B covers approximately the central valley of California, including Fresno, while Region A covers the rest of the state, including Riverside and all of southern California. The monthly predicted nitrate at Fresno and Riverside is shown in Fig. 12 for the ammonia sensitivity simulations, along with the observed nitrate. At Fresno, a double or even tenfold increase in ammonia emissions is not sufficient to simulate the high wintertime nitrate concentrations observed at this location; this result is consistent with the low levels of predicted total nitrate relative to the predicted total ammonia at this location (Fig. 8). At Riverside, a doubling of ammonia emissions roughly doubles the predicted nitrate concentrations, but the predicted concentrations are still below the measured concentrations throughout the year. A tenfold increase in ammonia emissions yields predicted concentrations that are within the overall range of measured concentrations throughout the year, although the month to month variations are not captured as well as the annual average.

Table 2 summarizes the normalized mean biases in seasonal and annual predicted aerosol concentrations in the ammonia sensitivity simulations. In the ammonia sensitive Region A of California, the magnitude of the negative nitrate



Fig. 11. California regions of high (Region A) and low (Region B) ammonia sensitivity in predicted nitrate. Region A (yellow areas in California) comprises the grid points for which predicted 2009 annual nitrate concentrations increase by 60 % or more above the base case when ammonia emissions are doubled in GEOS-Chem. Region B (blue areas in California) comprises the grid points for which predicted 2009 annual nitrate concentrations increase by less than 60 % when ammonia emissions are doubled in GEOS-Chem.

bias is substantially reduced with a doubling of ammonia emissions (annual average NMB of -13% in the $2 \times \text{NH}_3$ simulation, compared to -55% in the base case). When ammonia emissions are increased tenfold, there are large positive biases in the predicted nitrate in Region A in all seasons, with NMB of $+130\%$ in the annual average. These results indicate that in order to simulate observed nitrate aerosols in Region A, the annual total ammonia emissions in GEOS-Chem need to be increased by a factor of approximately two or slightly higher.

The seasonal biases in Table 2 indicate that an adjustment to the seasonality of ammonia emissions in GEOS-Chem (Park et al., 2004) could also improve the nitrate predictions in California Region A. Although a doubling of the annual total ammonia emissions reduces the annual average nitrate bias to -13% , the seasonal biases in this scenario are -35% in winter and $+26\%$ in summer. The seasonal scaling in GEOS-Chem (Park et al., 2004) is a single set of monthly scaling factors, which is applied uniformly to ammonia emissions over the whole country. These scaling factors attribute 73 % of annual ammonia emissions to the 7 months of April through September, with the remaining 27 % of annual emissions in the five month period of October through March. This seasonality is based primarily on ammonia emissions data from North Carolina (Aneja et al., 2000; Roelle and Aneja, 2002), an area that is likely representative of much of the US, but has colder winters and substantially less wintertime agricultural activity than California. The seasonal biases

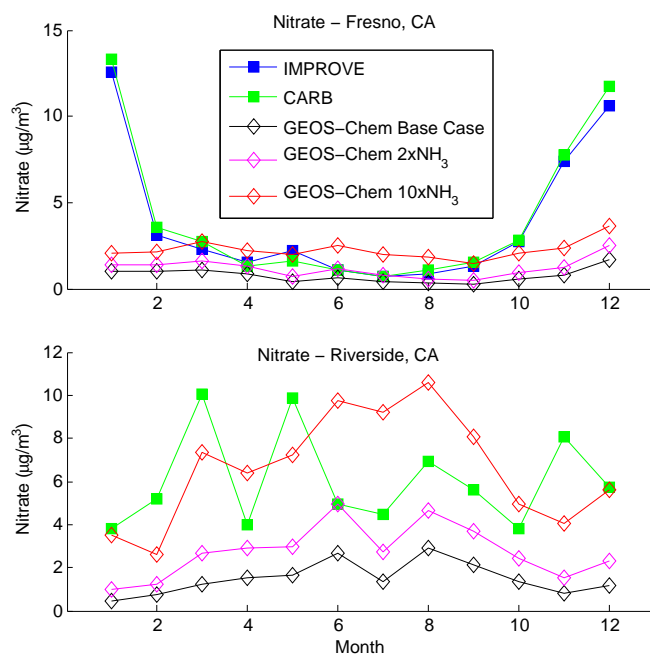


Fig. 12. 2009 monthly predicted aerosol nitrate at Fresno, CA and Riverside, CA in GEOS-Chem ammonia sensitivity simulations (base case, $2 \times \text{NH}_3$ emissions, and $10 \times \text{NH}_3$ emissions) compared with measured concentrations.

in nitrate shown in Table 2 and Fig. 12 suggest that in California, wintertime ammonia emissions comprise a larger fraction of the annual total, and summertime emissions comprise a smaller fraction of the annual total than the seasonality of Park et al. (2004). Since temperature and relative humidities are most favorable to nitrate formation in winter, this underestimate of the wintertime fraction of annual ammonia emissions in California is another likely cause for the under-prediction of nitrate in California Region A.

In contrast with Region A, when ammonia emissions are doubled, predicted annual nitrate concentrations in Region B still have a large negative bias (-51% in the $2 \times \text{NH}_3$ simulation, compared to -67% in the base case) (Table 2). Even a tenfold increase in ammonia emissions yields predicted nitrate concentrations that are still biased low by 12% in the annual average. These results indicate that in Region B, the under-prediction of nitrate aerosol may be a result of under-prediction of both ammonia and nitric acid in the central valley of California. Since nitrate aerosols are particularly sensitive to mixed layer depths, owing to the gas-particle equilibrium, the nitrate under-prediction could also arise in part from a potential regional overestimate of GEOS-5 mixed layer depths in the central valley due to unresolved topography in this region.

4.3 Satellite measurements of ammonia

To investigate the extent to which California ammonia emissions might be underestimated in GEOS-Chem, model pre-

dictions are compared to satellite measurements of ammonia in California in 2009 from the Tropospheric Emissions Spectrometer (TES) (Shephard et al., 2011; Beer et al., 2008). TES is a high-resolution (0.06 cm^{-1}) Fourier transform spectrometer onboard NASA's Aura satellite, in a sun-synchronous orbit with measurements at 01:30 and 13:30 LT. The spectrometer measures infrared radiation, and NH_3 concentrations are retrieved using optimal estimation methods (Bowman et al., 2006; Rodgers, 2000) with the Line-By-Line Radiative Transfer Model (LBLRTM) and the fast forward model (OSS-TES) (Clough et al., 2006; Moncet et al., 2008; Shephard et al., 2009). The ammonia data used in this study are from the TES Lite data product, Version 5 (<http://avdc.gsfc.nasa.gov/index.php?site=635564035&id=10&go=list&path=/NH3>).

To compare model predictions with satellite measurements, vertical profiles of predicted ammonia concentrations are sampled from GEOS-Chem hourly timeseries at each of the TES measurement locations and times. Each GEOS-Chem ammonia profile is interpolated from the model levels (47 vertical levels) onto the 15 vertical levels of the corresponding TES profile. The TES averaging kernel and a priori profile are applied to the interpolated profile using the equation $\hat{x} = x_a + A(x_i - x_a)$, where \hat{x} is a “retrieved” profile representing what TES would measure if the interpolated GEOS-Chem profile x_i were the true atmospheric state, x_a is the TES a priori profile, A is the TES averaging kernel representing the sensitivity of the retrieval to the true state, and the profiles \hat{x} , x_i and x_a are expressed as natural logarithm of the ammonia volume mixing ratios. An example TES retrieval, averaging kernel, and “retrieved” GEOS-Chem profile are shown in Fig. 13. Only TES retrievals with sufficiently high sensitivity (degrees of freedom for signal ≥ 0.5) are included in the comparison, with a total of 142 retrievals over the year. Inherent in our comparison is a mismatch in scales, since the TES footprint is approximately $5 \times 8 \text{ km}$ (Shephard et al., 2011), compared with the GEOS-Chem grid box size of approximately $56 \times 60 \text{ km}$ in California. However, since the predominant sources of ammonia in California are agricultural sources emitting over extended areas, we expect that sub-grid scale variations will be relatively small.

At a given vertical level, a TES retrieved profile may be strongly influenced by the choice of a priori, and vertical columns are dependent on the selected a priori profile. To reduce the influence of the a priori profiles in the comparison of GEOS-Chem predictions with TES, representative volume mixing ratio (RVMR) values (Shephard et al., 2011) are compared for the retrieved profiles from TES and GEOS-Chem. The RVMR is a boundary layer average volume mixing ratio (VMR) which is weighted by the TES sensitivity to provide an ammonia concentration that is representative of the vertical region over which TES is most sensitive. Examples of RVMRs from retrieved TES and GEOS-Chem profiles are shown in Fig. 13. The TES RVMR values used in this comparison have a mean error of 45% , where the RVMR error is

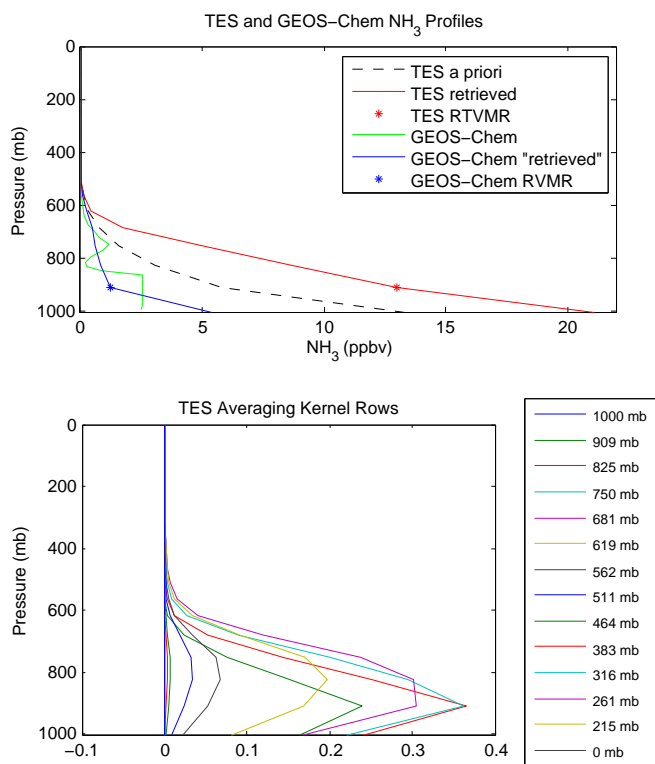


Fig. 13. Example ammonia profiles (TES, GEOS-Chem, and GEOS-Chem with the TES satellite operator applied) and TES averaging kernel, for the TES measurement at (120.39° W, 37.35° N), 18 May 2009, 01:30 p.m. PST and corresponding GEOS-Chem grid box and timestep

the sum of the measurement and smoothing errors described by Shephard et al. (2011). The RVMR values from TES and GEOS-Chem over California are shown for each month of 2009 in Fig. 14. The TES RVMR values exceed those from GEOS-Chem at most locations throughout the year. The normalized mean bias of GEOS-Chem predicted RVMRs relative to TES RVMRs, over the 142 retrievals in the year, is -79% , which could indicate that ammonia emissions in California are underestimated in GEOS-Chem. This negative bias is consistent with the findings of Shephard et al. (2011), who compared ammonia predictions from a global GEOS-Chem simulation to TES RVMRs, and with the findings of Heald et al. (2012), who compare ammonia predictions from a North American GEOS-Chem simulation to vertical columns from the Infrared Atmospheric Sounding Interferometer (IASI) satellite measurements; in both of these studies, ammonia was under-predicted compared with satellite measurements.

The spatial and temporal coverage of TES ammonia measurements is relatively sparse, so an analysis of monthly or seasonal averages is not feasible. However, the TES measurements qualitatively indicate that the seasonal variation of ammonia emissions in California is less than the country-wide

seasonality used in GEOS-Chem (Fig. 14), with a greater fraction of annual emissions occurring during the winter months than the currently assumed seasonality. Zhang et al. (2012) developed seasonal scaling factors for ammonia emissions based on measurements of total ammonia (ammonia plus ammonium aerosol) from the Midwest Ammonia Monitoring Project and the Southeastern Aerosol Research and Characterization; their analysis suggests a broadening of the summer peak, with enhanced springtime emissions. Comparison with IASI measurements also supports this increase in springtime emissions (Heald et al., 2012). The Zhang et al. (2012) seasonality, based on data from the midwest and southeast, improves the seasonal variations in predicted ammonia concentrations in these areas, and is likely representative of much of the country. In California, however, where ammonia emissions are high and winters are relatively warmer, our results suggest that seasonal variability of ammonia emissions differs substantially from those in the Midwest/East, and a seasonality customized to California conditions is needed in order to adequately simulate the observed nitrate concentrations in much of the state.

While we do not perform inverse modeling in the present study, inverse modeling represents a powerful method to assess the consistency between observed concentrations and emission inventories (Zhu et al., 2012; Turner et al., 2012).

5 Conclusions

Atmospheric chemical transport models (ACTMs) provide a powerful means to evaluate the extent to which predicted atmospheric gas and particle concentrations based on an assumed emission inventory agree with those actually observed. Prediction of aerosol levels over the US is a subject of intense interest, owing to efforts to achieve compliance with air quality standards and to assess the extent to which air quality is affected by long-range transport beyond the US border. Previous ACTM simulations of aerosol levels have exhibited mixed success in terms of agreement between predicted and observed concentrations. When predictions and observations do not agree, assessing the cause of the discrepancy may not be entirely straightforward, as both the emission inventory and representation of atmospheric processes may be implicated. The present study addresses the prediction of aerosol nitrate, sulfate, and ammonium levels over the US for 2009. Lack of agreement between observed and predicted levels can be traced to both emission inventory inaccuracies as well as model representation of nitric acid formation. The GEOS-Chem model employed here is the most widely used ACTM worldwide. The present study, and others like it, is valuable in pinpointing sources of model-measurement discrepancy and thereby lead to improvements in treatment of atmospheric processes and emission estimates.

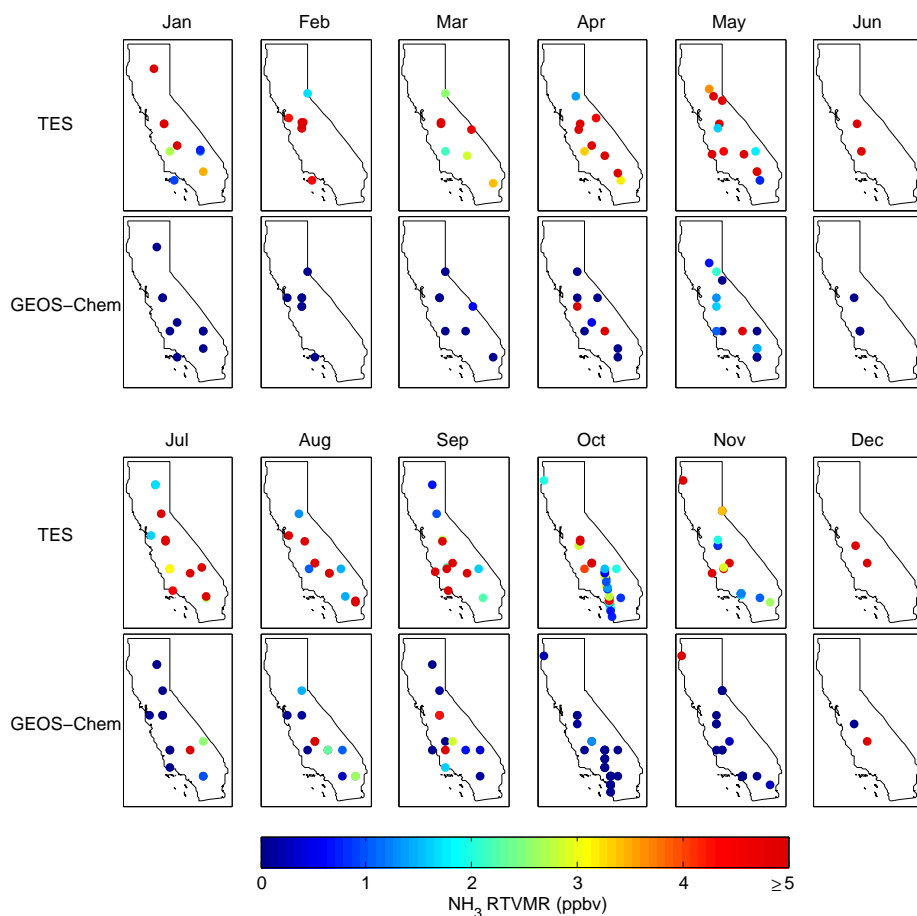


Fig. 14. Satellite-measured (TES) and predicted ammonia RVMR concentrations for 2009. Data points shown are individual measurements in each month; some data points overlap when there is more than one measurement at a location within a month.

Acknowledgements. The authors acknowledge the Clean Air Status and Trends Network (CASTNET), the Interagency Monitoring of Protected Visual Environments (IMPROVE), the California Air Resources Board (CARB), and NASA Jet Propulsion Laboratory for providing measurement data. Discussions with Joseph Ensberg, Karen Cady-Pereira, Debra Wunch, Paul Wennberg, Colette Heald and Havala Pye are greatly appreciated.

Edited by: M. Kopacz

References

- Aneja, V. P., Chauhan, J. P., and Walker, J. T.: Characterization of atmospheric ammonia emissions from swine waste storage and treatment lagoons, *J. Geophys. Res.*, 105, 11535–11545, doi:10.1029/2000JD900066, 2000.
- Bauer, S. E., Koch, D., Unger, N., Metzger, S. M., Shindell, D. T., and Streets, D. G.: Nitrate aerosols today and in 2030: a global simulation including aerosols and tropospheric ozone, *Atmos. Chem. Phys.*, 7, 5043–5059, doi:10.5194/acp-7-5043-2007, 2007.
- Bey, I., Jacob, D. J., Yantosca, R. M., Logan, J. A., Field, B. D., Fiore, A. M., Li, Q. B., Liu, H. G. Y., Mickley, L. J., and Schultz, M. G.: Global modeling of tropospheric chemistry with assimilated meteorology: model description and evaluation, *J. Geophys. Res.-Atmos.*, 106, 23073–23095, doi:10.1029/2001JD000807, 2001.
- Beer, R., Shephard, M. W., Kulawik, S. S., Clough, S. A., Eldering, A., Bowman, K. W., Sander, S. P., Fisher, B. M., Payne, V. H., Luo, M., Osterman, G. B., and Worden, J. R.: First satellite observations of lower tropospheric ammonia & methanol, *Geophys. Res. Lett.*, 35, L09801, doi:10.1029/2008GL033642, 2008.
- Bouwman, A. F., Lee, D. S., Asman, W. A. H., Dentener, F. J., VanderHoek, K. W., and Olivier, J. G. J.: A global high-resolution emission inventory for ammonia, *Global Biogeochem. Cy.*, 11, 561–587, doi:10.1029/97GB02266, 1997.
- Bowman, K. W., Rodgers, C. D., Sund-Kulawik, S., Worden, J., Sarkissian, E., Osterman, G., Steck, T., Luo, M., Eldering, A., Shephard, M. W., Worden, H., Clough, S. A., Brown, P. D., Rinsland, C. P., Lampel, M., Gunson, M., and Beer, R.: Tropospheric emission spectrometer: Retrieval method and error analysis, *IEEE T. Geosci. Remote*, 44, 1297–1307, doi:10.1109/TGRS.2006.871234, 2006.
- Chen, D., Wang, Y., McElroy, M. B., He, K., Yantosca, R. M., and Le Sager, P.: Regional CO pollution and export in China simulated by the high-resolution nested-grid GEOS-Chem model, *Atmos. Chem. Phys.*, 9, 3825–3839, doi:10.5194/acp-9-3825-2009, 2009.

- 2009.
- Clough, S. A., Shephard, M. W., Worden, J., Brown, P. D., Worden, H. M., Luo, M., Rodgers, C. D., Rinsland, C. P., Goldman, A., Brown, L., Kulawik, S. S., Eldering, A., Lampel, M. C., Osterman, G., Beer, R., Bowman, K., Cady-Pereira, K. E., and Mlawer, E. J.: Forward Model and Jacobians for Tropospheric Emission Spectrometer Retrievals, *IEEE T. Geosci. Remote*, 44, 1308–1323, 2006.
- Evans, M. J. and Jacob, D. J.: Impact of new laboratory studies of N_2O_5 hydrolysis on global model budgets of tropospheric nitrogen oxides, ozone, and OH, *Geophys. Res. Lett.*, 32, L09813, doi:10.1029/2005GL022469, 2005.
- Fountoukis, C. and Nenes, A.: ISORROPIA II: a computationally efficient thermodynamic equilibrium model for K^+ - Ca^{2+} - Mg^{2+} - NH_4^+ - Na^+ - SO_4^{2-} - NO_3^- - Cl^- - H_2O aerosols, *Atmos. Chem. Phys.*, 7, 4639–4659, doi:10.5194/acp-7-4639-2007, 2007.
- Heald, C. L., Collett Jr., J. L., Lee, T., Benedict, K. B., Schwandner, F. M., Li, Y., Clarisse, L., Hurtmans, D. R., Van Damme, M., Clerbaux, C., Coheur, P.-F., Philip, S., Martin, R. V., and Pye, H. O. T.: Atmospheric ammonia and particulate inorganic nitrogen over the United States, *Atmos. Chem. Phys.*, 12, 10295–10312, doi:10.5194/acp-12-10295-2012, 2012.
- Huang, M., Carmichael, G. R., Adhikary, B., Spak, S. N., Kulkarni, S., Cheng, Y. F., Wei, C., Tang, Y., Parrish, D. D., Oltmans, S. J., D'Allura, A., Kaduwela, A., Cai, C., Weinheimer, A. J., Wong, M., Pierce, R. B., Al-Saadi, J. A., Streets, D. G., and Zhang, Q.: Impacts of transported background ozone on California air quality during the ARCTAS-CARB period – a multi-scale modeling study, *Atmos. Chem. Phys.*, 10, 6947–6968, doi:10.5194/acp-10-6947-2010, 2010.
- Koracin, D. and Berkowicz, R.: Nocturnal Boundary Layer Height: Observations by Acoustic Sounders and Prediction in Terms of Surface Layer Parameters, *Bound.-Lay. Meteorol.*, 43, 65–83, doi:10.1007/BF00153969, 1988.
- Lin, J. T. and McElroy, M. B.: Impacts of boundary layer mixing on pollutant vertical profiles in the lower troposphere: Implications to satellite remote sensing, *Atmos. Environ.*, 44, 1726–1739, doi:10.1016/j.atmosenv.2010.02.009, 2010.
- Liu, H., Jacob, D. J., Bey, I., and Yantosca, R. M.: Constraints from ^{210}Pb and ^7Be on wet deposition and transport in a global three-dimensional chemical tracer model driven by assimilated meteorological fields, *J. Geophys. Res.-Atmos.*, 106, 12109–12128, doi:10.1029/2000JD900839, 2001.
- Liu, Shuyan and Xin-Zhong, Liang: Observed Diurnal Cycle Climatology of Planetary Boundary Layer Height, *J. Climate*, 23, 5790–5809, doi:10.1175/2010JCLI3552.1, 2010.
- Macintyre, H. L. and Evans, M. J.: Sensitivity of a global model to the uptake of N_2O_5 by tropospheric aerosol, *Atmos. Chem. Phys.*, 10, 7409–7414, doi:10.5194/acp-10-7409-2010, 2010.
- Montgomery, D. C., Peck, E. A., and Vining, G. G.: Introduction to Linear Regression Analysis, 4th Edn., John Wiley & Sons Inc., Hoboken, New Jersey, 2006.
- Myhre, G., Grini, A., and Metzger, S.: Modelling of nitrate and ammonium-containing aerosols in presence of sea salt, *Atmos. Chem. Phys.*, 6, 4809–4821, doi:10.5194/acp-6-4809-2006, 2006.
- Moncet, J.-L., Uymin, G., Lipton, A. E., and Snell, H. E.: Infrared radiance modeling by optimal spectral sampling, *J. Atmos. Sci.*, 65, 3917–3934, 2008.
- Nowak, J. B., Neuman, J., Bahreini, R., Middlebrook, A. M., Holloway, J., McKeen, S., Parrish, D., Ryerson, T., and Trainer, M.: Ammonia sources in the California South Coast Air Basin and their impact on ammonium nitrate formation, *Geophys. Res. Lett.*, 39, L07804, doi:10.1029/2012GL051197, 2012.
- Park, R. J., Jacob, D. J., Field, B. D., Yantosca, R. M., and Chin, M.: Natural and transboundary pollution influences on sulfate-nitrate-ammonium aerosols in the United States: implications for policy, *J. Geophys. Res.*, 109, D15204, doi:10.1029/2003JD004473, 2004.
- Pye, H. O. T., Liao, H., Wu, S., Mickley, L. J., Jacob, D. J., Henze, D. K., and Seinfeld, J.: Effect of changes in climate and emissions on future sulfate-nitrate-ammonium aerosol levels in the United States, *J. Geophys. Res.*, 114, D01205, doi:10.1029/2008JD010701, 2009.
- Rodgers, C. D.: Inverse methods for atmospheric Sounding: Theory and Practice, World Sci., Hackensack, NJ, 2000.
- Ruelle, P. A. and Aneja, V. P.: Characterization of ammonia emissions from soils in the upper coastal plain, North Carolina, *Atmos. Environ.*, 36, 1087–2097, doi:10.1016/S1352-2310(01)00355-7, 2002.
- Seinfeld, J. H. and Pandis, S.: Atmospheric Chemistry and Physics – From Air Pollution to Climate Change, 2nd Edn., John Wiley & Sons Inc., Hoboken, New Jersey, 2006.
- Shephard, M. W., Clough, S. A., Payne, V. H., Smith, W. L., Kireev, S., and Cady-Pereira, K. E.: Performance of the line-by-line radiative transfer model (LBLRTM) for temperature and species retrievals: IASI case studies from JAIVEx, *Atmos. Chem. Phys.*, 9, 7397–7417, doi:10.5194/acp-9-7397-2009, 2009.
- Shephard, M. W., Cady-Pereira, K. E., Luo, M., Henze, D. K., Pinder, R. W., Walker, J. T., Rinsland, C. P., Bash, J. O., Zhu, L., Payne, V. H., and Clarisse, L.: TES ammonia retrieval strategy and global observations of the spatial and seasonal variability of ammonia, *Atmos. Chem. Phys.*, 11, 10743–10763, doi:10.5194/acp-11-10743-2011, 2011.
- Sickles II, J. E. and Shadwick, D. S.: Precision of atmospheric dry deposition data from the Clean Air Status and Trends Network, *Atmos. Environ.*, 36, 5671–5686, doi:10.1016/S1352-2310(02)00723-9, 2002.
- Turner, A. J., Henze, D. K., Martin, R. V., and Hakami, A.: The spatial extent of source influences on modeled column concentrations of short-lived species, *Geophys. Res. Lett.*, 39, L12806, doi:10.1029/2012GL051832, 2012.
- van Donkelaar, A., Martin, R. V., Pasch, A. N., Szykman, J. J., Zhang, L., Wang, Y. X., and Chen, D.: Improving the accuracy of daily satellite-derived ground-level fine aerosol concentration estimates for North America, *Environ. Sci. Technol.*, 46, 11971–11978, doi:10.1021/es3025319, 2012.
- Wesley, M. L.: Parameterization of surface resistances to gaseous dry deposition in regional-scale numerical models, *Atmos. Environ.*, 23, 1293–1304, doi:10.1016/0004-6981(89)90153-4, 1989.
- Wu, S., Mickley, L. J., Jacob, D. J., Logan, J. A., and Yantosca, R. M.: Why are there large differences between models in global budgets of tropospheric ozone?, *J. Geophys. Res.*, 112, D05302, doi:10.1029/2006JD007801, 2007.
- Zhang, L., Jacob, D. J., Knipping, E. M., Kumar, N., Munger, J. W., Carouge, C. C., van Donkelaar, A., Wang, Y. X., and Chen, D.: Nitrogen deposition to the United States: distribution,

- sources, and processes, *Atmos. Chem. Phys.*, 12, 4539–4554, doi:10.5194/acp-12-4539-2012, 2012.
- Zhang, L. M., Gong, S. I., Padro, J., and Barrie, L.: A size-segregated particle dry deposition scheme for an atmospheric aerosol module, *Atmos. Environ.*, 35, 549–560, doi:10.1016/S1352-2310(00)00326-5, 2001.
- Zhu, L., Henze, D. K., Cady-Pereira, K. E., Shephard, M. W., Luo, M., Pinder, R. W., Bash, J. O., and Jeong, G.: Constraining U.S. ammonia emissions using TES remote sensing observations and the GEOS-Chem adjoint model, *J. Geophys. Res.*, submitted, 2012.